Heinrich Heine
Universität Düsseldorf

Structure and Dynamics of Colloids in Quasicrystalline Optical Fields

Inaugural-Dissertation

zur Erlangung des Doktorgrades der Mathematisch-Naturwissenschaftlichen Fakultät der Heinrich-Heine-Universität Düsseldorf

vorgelegt von

Caroline-Christine Marciniak

aus Düsseldorf

Düsseldorf, 07. April 2022

Aus dem Institut für experimentelle Physik der kondensierten Materie
am Lehrstuhl für Physik der weichen Materie

Gutachter: Prof. Dr. Stefan U. Egelhaaf

Zweitgutachter: Prof. Dr. Jan K.G. Dhont

aus dem Institut für der Heinrich-Heine-Universität Düsseldorf

Gedruckt mit der Genehmigung der Mathematisch-Naturwissenschaftlichen Fakultät der Heinrich-Heine-Universität Düsseldorf

Berichterstatter:

1. Prof. Dr. Stefan U. Egelhaaf

2. Prof. Dr. Jan K. G. Dhont

Tag der mündlichen Prüfung: 08.08.2022

Declaration of Originality

This dissertation is the result of my own work and includes nothing which is the outcome of work done in collaboration except as specified in the text. It was prepared considering the "Grundsätze zur Sicherung guter wissenschaftlicher Praxis an der Heinrich-Heine-Universität Düsseldorf". It is not substantially the same as any that I have submitted, or, is being concurrently submitted for a degree or diploma or other qualification at the Heinrich-Heine-Universität or any other University or similar institution except as specified in the text. I further state that no substantial part of my dissertation has already been submitted, or, is being concurrently submitted for any such degree, diploma or other qualification at the Heinrich-Heine-Universität or any other University of similar institution except as specified in the text.

Düsseldorf, 19.09.2022
(Place, Date)

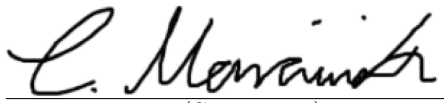

(Signature)

Abstract

Spherical micron-sized polystyrene particles (diameter $d = 2.1\,\mu m$) dispersed in a water/ heavy-water mixture are being studied in light fields with a quasicrystalline 10-fold rotational symmetry under bright-field microscopy. Unlike periodic crystals, quasicrystals possess no translational, but a long-range orientational order. Quasicrystals are popular objects to study and e. g. their stability mechanisms and formation can be examined diversely in soft matter systems.

In this work, the formation of colloidal quasicrystals is studied in six different light fields constructed from overlaying double rings positioned on a decagonal (10-fold) "Tuebingen" tiling. The ratio of the ring radii needs to be close to the so-called golden mean ($\phi \approx 1.618$) due to stability reasons.
The patterns acting as templates are uploaded on a so-called Digital Micromirror Device (DMD), which is illuminated by an expanded Gaussian laser beam ($\lambda = 532\,nm$). Due to the periodic arrangement of the DMD mirrors, diffraction effects arise predominantly with a coherent illumination source like a laser, which have to be accounted for during the construction and alignment of the setup. The whole mirror array projects a greyscale image into a sample plane, where each micro-mirror represents one image pixel. The particles can arrange according to the light field in an effective 2D system and can be "trapped" in a harmonic potential at positions for quasicrystalline symmetry.
Samples with different particle concentrations are being studied under six different 10-fold template patterns with varying field potential amplitude by adjusting the laser intensity.
The resulting quasicrystalline structures are analysed in Fourier Space as diffraction patterns, which show Bragg peaks on defined positions indicative of a decagonal long-range orientational order.

By analysing the dynamics of the particles in the decagonal light field it has been found, that the particles are performing jumps on the template, from one minimum of the light field potential to another as well as inside the minimum. These jumps are located with a phop-algorithm, which registers the time and position of a jump. The hop time τ_h between these "hops" is calculated to estimate the time, the particles require for one jump. It shows, that there are two time regimes at short and long times, which are representative of the movement in a trap and the jumping from one trap position to another respectively and can be separated via exponential fitting to the probability distributions of the jump times. Additionally, the time a particle spent trapped in the template potential has been determined by quantifying the compactness of a trajectory with the so-called packing coefficient. These residence times showed an overlap with the longer times between two particle jumps, indicating that the particles are jumping from one trap to another.
It has been found that a higher laser intensity increases the time a particle stays trapped in a tiling position due to increased strength of the potential. A higher particle concentration lowers the time between two jumps, since inter-particle interactions gain dominance over the light-field potential, raising the probability of shorter jump times. Among the tested

templates, the one with a tiling distance of two times the particle diameter showed longer dwell times, than the template with larger distances. The short jumps, i. e. particle fluctuations inside of a trap were neither influenced by a variation in the laser intensity nor by changing the particle concentration.

Finally, experiments were conducted with a holographic-optical-tweezers setup. Here, a liquid-crystal spatial light modulator (LC-SLM) is used instead of the Digital Micromirror Device as the method for creating light fields. Hexagonal (6-fold) crystals are constructed from feedback programming of a light field that adapts to the current particle positions. Light potentials with two length scales e. g. Gaussian double rings that support quasicrystalline symmetry did form metastable clusters with local 4-fold and 12-fold symmetries. Additionally, hexagonal crystal twins were found.

Zusammenfassung

Kugelförmige Polystyrol-Mikroteilchen (Durchmesser $d = 2.1\,\mu m$) in einer Mischung aus Wasser (H_2O) und schwerem Wasser (D_2O) wurden in Lichtfeldern mit quasikristalliner 10-facher Rotationssymmetrie unter dem Lichtmikroskop untersucht.
Anders als periodische Kristalle, haben so genannte Quasikristalle keine Translationsordnung, sondern eine orientierungsabhängige Ordnung mit langer Reichweite. Das bedeutet, dass sich die Ordnung erst bei Betrachtung längerer Abschnitte des Kristalls äußert.
Quasikristalle sind ein populäres Forschungsobjekt, um z. B. ihre Stabilitäts- und Entstehungsmechanismen auf vielfältige Art zu studieren besonders im Bereich der weichen Materie.

In dieser Arbeit werden kolloidale Quasikristalle in sechs verschiedenen Lichtfeldern studiert, welche sich durch Überlappung von Doppelringen an Positionen eines dekagonalen (mit 10-facher Rotationssymmetrie) "Tübingen" Kachelmusters konstruieren lassen. Dabei muss das Verhältnis der Radien zueinander aus Stabilitätsgründen nah am so genannten goldenen Schnitt ($\phi \approx 1.618$) liegen.
Die Template-Muster werden zu einem so genannten Digital Micromirror Device (DMD) gesendet, welches wiederum von einem aufgeweiteten Laserstrahl mit Gauss'schem Intensitätsprofil beleuchtet wird. Wegen der periodischen Anordnung der Mikrospiegel des DMD, kommt es zu Beugungseffekten, die bei der Anordnung und dem Aufbau einkalkuliert werden müssen. Die Effekte treten vor allem bei Verwendung einer kohärenten Beleuchtung z.B. mit einem Laser auf. Der Spiegelarray des DMD projiziert ein Bild in Graustufen in die Probenebene, wobei jeder Mikrospiegel einem Bildpixel entspricht. Die Teilchen ordnen sich in einer 2D-Ebene in der Probe nach dem Muster des Lichtfelds an, wobei sie in einem harmonischen Potential mithilfe optischer Fallen an Positionen gefangen werden, die zusammen einen quasikristallines Muster ergeben.
Proben mit verschiedener Teilchenkonzentration werden in sechs unterschiedlichen Templates mit 10-facher Rotationssymmetrie untersucht, wobei auch der Einfluss der Stärke des Lichtfeld-Potentials durch Variation der Laserintensität studiert wird. Die daraus resultierenden quasikristallinen Strukturen werden im Fourierraum als Beugungsmuster untersucht. Diese weisen so genannte Bragg-Peaks auf wohldefinierten Positionen auf, die auf eine 10-fache langreichweitige Orientierungsordnung hindeuten.

Aus der Analyse der Dynamik der Teilchen in den Lichtfeldern geht hervor, dass die Teilchen auf dem Template Sprünge sowohl von einem Minimum des Potentials zum nächsten, als auch innerhalb eines Minimums absolvieren. Diese Sprünge werden mit einem so genannten "Phop-Algorithmus" erkannt, welcher die Position und den Zeitpunkt eines Sprunges detektiert. Die Zeit τ_h, die ein Teilchen zwischen zwei Sprüngen benötigt, kann daraus hergeleitet werden. Dabei zeigte sich, dass die Zeiten eine Kategorisierung in kurze Sprünge innerhalb einer optischen Falle als auch Sprünge von einer Falle zur nächsten erlauben, indem für kurze und lange Zeiten jeweils ein exponentieller Fit an die Wahrscheinlichkeitsverteilung der Zeiten durchgeführt wird.

Zusätzlich wird über den so genannten “packing coefficient” aus dem Kompaktheitsgrad der Trajektorie die Zeit bestimmt, die ein Teilchen in einer optischen Falle des Lichtfelds verbringt. Diese Zeiten weisen einen Überlappungsbereich mit den längeren Zeiten aus der Phop-Analyse auf, was darauf hindeutet, dass diese Sprünge von Falle zur Falle geschehen. Es zeigt sich, dass eine höhere Teilchenkonzentration die Zeit zwischen zwei Sprüngen verringert, da die Interaktionen zwischen den Teilchen an Bedeutung gegenüber dem Lichtfeld gewinnen und somit die Wahrscheinlichkeit für Sprünge bei kürzeren Zeiten erhöhen. Währenddessen erzeugen höhere Laserintensitäten eine Verstärkung des Potentials und erhöhen somit die Zeit, die die Teilchen in einer Falle verbringen. Unter den getesteten Templates ergab sich, dass das Template mit Positionen in einem Abstand von zwei Teilchendurchmessern längere Zeiten zwischen den Sprüngen aufweist als ein Template mit längeren Abständen zwischen den Positionen. Kurze Sprünge, das heißt, Fluktuationen innerhalb einer optischen Falle an den Templatepositionen, wurden weder durch die Teilchenkonzentration, noch durch die Laserintensität beeinflusst.

Schließlich wurden noch Experimente mit so genannten holografischen optischen Pinzetten durchgeführt, welche statt einem DMD einen so genannten “Liquid-crystal Spatial Light Modulator” (LC-SLM) zur erzeugung der Lichtfelder verwenden. Hierbei wurden hexagonale Kristalle (mit 6-facher Rotationssymmetrie) durch Rückkopplung des Lichtfeld an die Teilchenpositionen erzeugt. Lichtfelder mit zwei Längenskalen, z. B. Doppelringe mit Radienverhältnissen, die Quasikristalle ermöglichen, führten zu der Bildnung von Teilchen-Clustern mit lokaler 4- oder 12-facher Rotationssymmetrie und so genannten hexagonalen Kristallzwillingen.

Acknowledgement

First of all, I would like to thank Prof. Stefan Egelhaaf for his extensive help and fruitful discussions, which helped me to progress in my work. Discussions together with Prof. Jan Dhont, my supervisor at "Forschungszentrum Jülich", always helped me not to lose sight of the overall aim of my project and kept me progressing. I thank you both for your tremendous help and your flexibility to always find some time for regular meetings with me.

To Dr. Thorsten Auth at the "Forschungszentrum Jülich", I want to give my thanks for arranging the financial support for my project. Without it, the last years of my work would not be possible at all. The same goes for Prof. Egelhaaf, who also managed to keep me financially supported.
On top of that, I thank Dr. Auth for his organisation of the IHRS Biosoft student seminar and IHRS soft skill courses, which offered tremendous help scientifically and with regard to presentation and soft skills.

During the installation of my setup, I encountered some obstacles and delays, due to missing components or defective equipment. During this time many people helped me to circumvent those problems and continue swiftly with my work. Among these is Dr. Debasish Saha, who helped me especially at the beginning of my thesis to get into the workflow and showed me how to operate the Spatial Light Modulator (SLM) setup and optical tweezers in the first place. He also guided me through programming in Labview and Matlab for setup control and data analysis. He proposed the idea, that I could continue measuring with the Digital Micromirror Device (DMD) and building the setup for it.
Especially for building the setup, Dr. Angel Zuccolotto Bernez was the one who helped me enormously with tools and tricks. He taught me the basics of laser alignment and the alignment of optical components. When I came across problems with the alignment of the DMD, he took his time and experience to understand the operation principle of the DMD himself and together we managed to align the device properly. Finally, together in discussions with Prof Egelhaaf and Dr. Saha, we were able to work around encountered problems and make the DMD-setup operable.
In other cases where I encountered hindrances, Manuel Escobedo-Sánchez, as well as Dr. Andreas Pamvouxoglou, were always there to offer help or their expertise.
To Dr. Florian Platten I would like to give my thanks, especially for his annual laser safety instructions. Without it, I would not be able to do my work in a safe environment and finish it without getting harmed.
Additionally, I would like to thank Mrs Dietlind Vobis for her technical help in terms of the operation of computers and related components may it be hard- or software. And my thank goes as well to Mrs Katrin Reh for her help in organisation and administration.

To sum up, I would like to thank everyone who helped me during the last years and whom I did not mention explicitly, but whose help was not lesser impactful on my work. And I would like to mention, that although many discussions and meetings were not in person due

to COVID restrictions, they were no less effective and instrumental.
Finally, my thank goes to my family, who faithfully supported and motivated me with reassuring words to continue and finish this work.

"In the smallest things nature shows its greatest wonders".
-Carl Linnaeus

Contents

List of Figures

List of Tables

Acronyms

DMD	Digital Micromirror Device	viii
SLM	Spatial Light Modulator	viii
HOT	Holographic Optical Tweezers	3
CCD	Charged-Coupled Device	3
PMMA	Polymethyl Methacrylate	9
RCP	Random Closed Packing	12
CNT	Classical Nucleation Theory	13
PDF	Probability Density Function	26
MSD	Mean Squared Displacement	27
FOV	Field of view	43
DDM	Differential Dynamic Microscopy	43
DLS	Dynamic Light Scattering	43
NA	Numerical aperture	46
AOD	Acoustic-Optical Deflector	55
FFT	Fast Fourier Transformation	56
GMM	galvanometer-mounted mirrors	58
DFT	Discrete Fourier Transform	66
BDL	Barkan-Diamant-Lifshitz Model	117
DLVO	Potential for charged-stabilised colloidal suspensions named after Boris Derjaguin, Lev Landau, Evert Verwey and Theodoor Overbeek	
TNLC	Twisted-nematic liquid crystal; used in SLM-arrays.	

1 Introduction

Soft matter and colloidal particles can be encountered regularly in our everyday life. Whether in food, cosmetic products or in medicine and healthcare, soft matter is contained in many consumer goods of today. In science, they serve as model systems e. g. for atomic systems. This is due to the fact that soft matter objects are in the size range of 1 nm to 10 µm [1] making them several orders larger than atoms. This makes it easier to study them since they are large enough to be visible with light microscopy, but also small enough to be manipulated with light like in optical tweezers.

Like in atoms colloidal particles undergo phase separations. Moreover, colloidal phases can be observed in real-time and manipulated more easily by tuning not only environmental parameters but also the particles' concentration.

In contrast to solid crystals, quasicrystals show a long-range order without a strict periodicity. They may even seem amorphous at first glance but show a long-range rotational symmetry unlike that of any regular crystals. Various arrangements are being studied in mathematics and new tilings are being created after aperiodic tiling rules. The aesthetics of quasicrystalline tilings are often used in art, e. g. as mosaics but can also be found in nature. An example of one-dimensional quasiperiodicity is the Fibonacci sequence, which is the underlying rule for the formation of plant florets e. g. in sunflowers [2].
Linked to the Fibonacci series is the golden ratio ($(1+\sqrt{5})/2 \approx 1.618$), which appears in repeating units defining the rotational symmetry of quasicrystals. Whereas for periodic crystals only 2-, 3-, 4-, and 6-fold non-trivial rotational symmetries are allowed, quasicrystals have far higher values even up to 24. Symmetries of 10 and 12 are most common, also called decagonal and dodecagonal symmetries after the respective Greek numbers.
In photonic applications, the long-range order of quasicrystals is exploited. Hence soft quasicrystals are candidate systems for studying optical properties of photonic crystals since the structures formed by colloids are on the scale of visible wavelengths and can be directly observed and analysed [3].

Self-assembly and crystallisation of particles are controlled by the interaction potential. The shape of particles, e. g. patchy-particles [3], constraints [1], or external forces, e. g. magnetic[4], electric [4], optical light fields [5] influence the particle interaction. In this work particles in optical light fields will be studied, i. e. particle manipulation via optical tweezers. Here, it is possible to control the position of a single micron-sized particle with a

laser beam, which is focused on a diffraction-limited spot. To create a stable optical trap for a spherical particle, certain requirements have to be met. First, the particles have to be preferably spherical and their size in the range of about 10 nm to 50 µm. Second, the refractive index of the particles has to be larger than that of their surrounding medium. For the laser, it is important, that it is tightly focused and has a Gaussian intensity profile. Only then, the scattering force pushing the particle in the direction of the beam will be smaller than the gradient force, that drives the particle into the focus. Once it reaches it, the particle will stay there, since the gradient force restores the particle's position to the focus, if it moves slightly away from it. The more it moves out of focus, the bigger the restoring force acting on it will be. The forces acting on a spherical particle will contribute differently to the total force and its direction. The gradient force will be greater than the scattering force. A stable trapping construction is then called optical tweezers because it is possible to hold and move a micron-sized object analogous to the use of common tweezers in the macroscopic length scale. The moving of traps can be achieved e. g. with galvanometer-mounted mirrors, which enable the steering of a particle held by the laser beam.

To steer several particles simultaneously multiple traps can be created with devices like an SLM or a DMD. In this work, two multiple tweezers setups with these devices will be presented.
For the main experiments a setup with a DMD is used, where the desired pattern is directly created on the device itself and imaged in the sample plane. This will be contrasted with Holographic Optical Tweezers (HOT), where multiple traps are created with a liquid crystal spatial light modulator (LC-SLM) forming a hologram, which is a pattern formed from phase information of the desired image pattern.
The DMD creates multiple tweezers more directly in real space without using holograms. This largely decreases the response time of the setup compared to the SLM and is limited only by the DMD's refresh rate and computational power.
A DMD consists of an array of many micron-sized mirrors, which can adopt two states and can be controlled independently. When a light beam illuminates the active area of the DMD, it will be reflected in the directions according to the two mirror states.
However, this will not simply result in two separate beams. Due to the periodic arrangement of the micron-sized regularly-spaced mirrors on the chip and the coherence of the laser light source, the reflected pattern will also show diffraction effects. This is a reason why the alignment of the DMD is an important part of building this setup.
Furthermore, homogeneous illumination of the DMD and minimisation of the loss of beam intensity have to be established. The Gaussian beam exiting the laser is expanded into a slightly larger size than the active area of the DMD and homogenised with a spatial filter. With dichroic mirrors, the DMD pattern is directed into the backport of a microscope and imaged with a telescopic arrangement of a convex lens and a high-numerical-aperture objective into the sample plane. The sample cell is constructed in a way, that the particles are moving effectively in a two-dimensional system. Images of this plane are recorded with a Charged-Coupled Device (CCD) camera and stored for further processing and analysis.

In the DMD experiments, it will be studied, how the particles behave in light fields with

quasicrystalline symmetry projected by the DMD. The light field is supposed to act as a substrate for the particles to arrange themselves into a pattern with the same 10-fold symmetry as predefined by the light template, hence creating quasicrystalline colloidal structures. Templates with different scaling are used to study the pattern formation under different particle concentrations and laser intensities of the light fields. The symmetry of the particle arrangement in real space can be deduced from the so-called diffraction pattern, which is studied in reciprocal space. These patterns will be analysed to determine to which degree the template pattern is recreated.

Moreover, it will be analysed how the particles diffuse in the template, e. g. by performing jumps, which can be categorised into short and long jumps.
The particles will encounter confinements of different sizes on the template. The sizes of these confinements can be estimated from the particle dynamics and the duration a particle spends in a confined area can be determined. With the knowledge of this residence time, the strength of the respective template can be deduced, i. e. the strength of the light field to trap particles in positions, which recreate the quasicrystalline symmetry of the template.

In the SLM experiments, the aim was to create quasicrystals and structures with 6-fold symmetries via feedback programming. Here, the particle coordinates are sent to the SLM to create a pattern, which adapts according to the particle positions. The light field changes the inter-particle interaction and hence can induce the formation of different local structures. Like this, a self-assembly process into clusters with 6- and 4-fold symmetries and varying lattice constants can be induced, by changing the length scales of the pattern and hence the interaction potential.

The thesis will consist of four sections. It will begin in chapter 2 with the basics of physical phenomena followed by an overview of the samples and experimental setups in chapter 3. The methods of analysing the structure of the particle arrangement in the different templates will be presented as well as an algorithm to register particle jumps for the analysis of particle dynamics.
Chapter 4 deals with the experiments of structure formation and measurements of particle dynamics, which will be analysed and discussed afterwards.
To conclude the findings will be summarised in chapter 5 and an outlook will be given.

2 Physics Fundamentals

This chapter deals with the physics groundwork for this thesis. It introduces each of the main topics, which are important for the understanding of the following chapters. Starting with an overview of colloidal particles in general, i. e. presenting their behaviour and its description with the help of mathematical definitions. Subsequently, the topic of colloidal crystals in general and especially quasicrystals will be treated in more detail, since they are the main systems studied in this work. Further, optical particle manipulation through optical tweezers will be presented, as this is the main technique used in the experiments. Their working principle and similarly the function of the spatial light modulator devices used in the setups will be explained.

2.1 Soft Matter and Colloids

Systems of colloidal particles are one of the most studied samples in soft matter physics. We encounter them quite often in products we use in our everyday life, e. g. food, cosmetic products or materials from the industry like paint. Since they appear in many different fields, it is rather difficult to provide a general definition for a colloid. The name was given by Thomas Graham in 1860 [1], who studied gelatinous polymer colloids. He named it after the ancient Greek word κόλλα (*kólla*) meaning "glue-like", since they can aggregate easily and show sticking behaviour. Today when we talk about colloids in soft matter physics, we usually mean particles in the size range from 1 nm to 10 µm [1]. This lies in the mesoscopic regime (fig. 2.1), where phenomena characteristic of soft matter physics can be observed, while quantum physical effects and chemical details can be neglected. Therefore, the surrounding medium, e. g. the water molecules can be treated as a continuum [3]. On the other hand, surface chemistry becomes more important in defining the particle interactions since the surface area-to-volume ratio is large on this length scale.

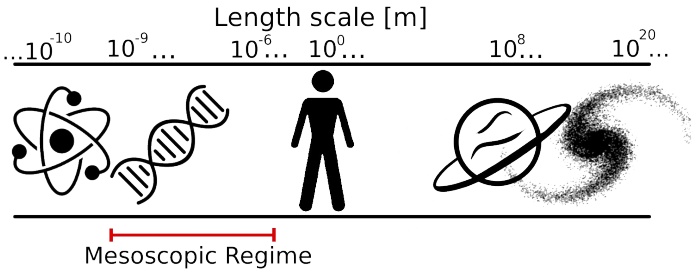

Figure 2.1: Location of the mesoscopic regime in the length scale spectrum (not to scale) [6],[7].

The particles in this work are plastic beads (2.1 µm in diameter) made out of polystyrene polymers and stabilised by sulfate charges [8]. Spherical particles are most common, but many different forms can be fabricated today with recent improvements in novel techniques [9], e. g. anisotropic or patchy particles ([10] ,[11]) resulting in different behaviour of the systems. Like atoms, colloids can form thermally equilibrated phases. But thermal energy plays a more important role in colloidal systems, enabling the manipulation of particle configuration as in optical tweezer experiments. E. g. colloidal crystals can easily be deformed due to lower energy density, hence the name "soft" matter [9].

Colloids can also be active, mimicking bacterial movement, and therefore exhibiting behaviour and phase transitions that cannot be observed in atomic systems [9]. This makes them good candidates for biology-inspired studies.
Since their size range can lie above the resolution limit of light-microscopy ($\approx 400\,nm$ at the most), they are perfect model systems for studying phase transitions. Crystallisation and self-assembly events can be observed directly in real space and hence the kinetic and non-equilibrium micro-scale processes studied [9].

In the next section, the inter-particle interactions will be presented since they gain importance for concentrated suspensions and the modelling of particles as hard spheres will be introduced. Before treating quasicrystals in detail, an overview of colloidal crystals and their formation will be given.

2.1.1 Inter-Particle Interactions

In a stabilised colloidal suspension, inter-particle interaction potential consists of a repulsive and an attractive part, which have to be balanced. Otherwise, the particles start to form aggregates leaving the sample unusable for experiments unless this behaviour is desired. The overall potential V_{tot} can then be written as

$$V_{tot} = V_R + V_A \ . \tag{2.1}$$

The most simple potential contributing to the repulsive part is a hard-sphere interaction in a monodispersed system defined as

$$V_{HS} = \begin{cases} \infty & r < 2R \ , \\ 0 & \text{else} \ , \end{cases} \tag{2.2}$$

where r is the particle distance and $2R$ is the particle diameter. The interaction between two particles can then be compared to the behaviour of two billiard balls. If the particles are apart, that means the distance r is greater than 2 radii R of the particles, the potential is zero. The same is true for the other direction if $r < 2R$ since the particles are impenetrable. Hence only for $r = 2R$, the potential is nonzero it is then infinitely large.

The attractive part V_A consists of Van der Waals interactions, which act on very short distances $< 100\,\text{nm}$. Johannes Diderik Van der Waal was a Dutch physicist, who discovered the interactions named after him in 1869. These forces originate from electron density fluctuations of the atoms and molecules in particles, causing a charge shift when two of them are less than 100 nm apart. This results in a dipole-dipole interaction, which weakens fast with greater distance due to r^{-6} dependence. The form of the Van der Waals potential is dependent on the geometry of the interacting objects. E. g. for two particles with radius R, which are a distance r apart, it can be calculated with the following formula

$$V_A = V_{vdW} = -\frac{A_H R}{12(r - 2R)} \ . \tag{2.3}$$

For this case, the curve looks like the red one depicted in fig. 2.2b. A_H is the Hamaker constant and it describes the strength of the interaction which is further dependent on the material of the interacting objects [12].

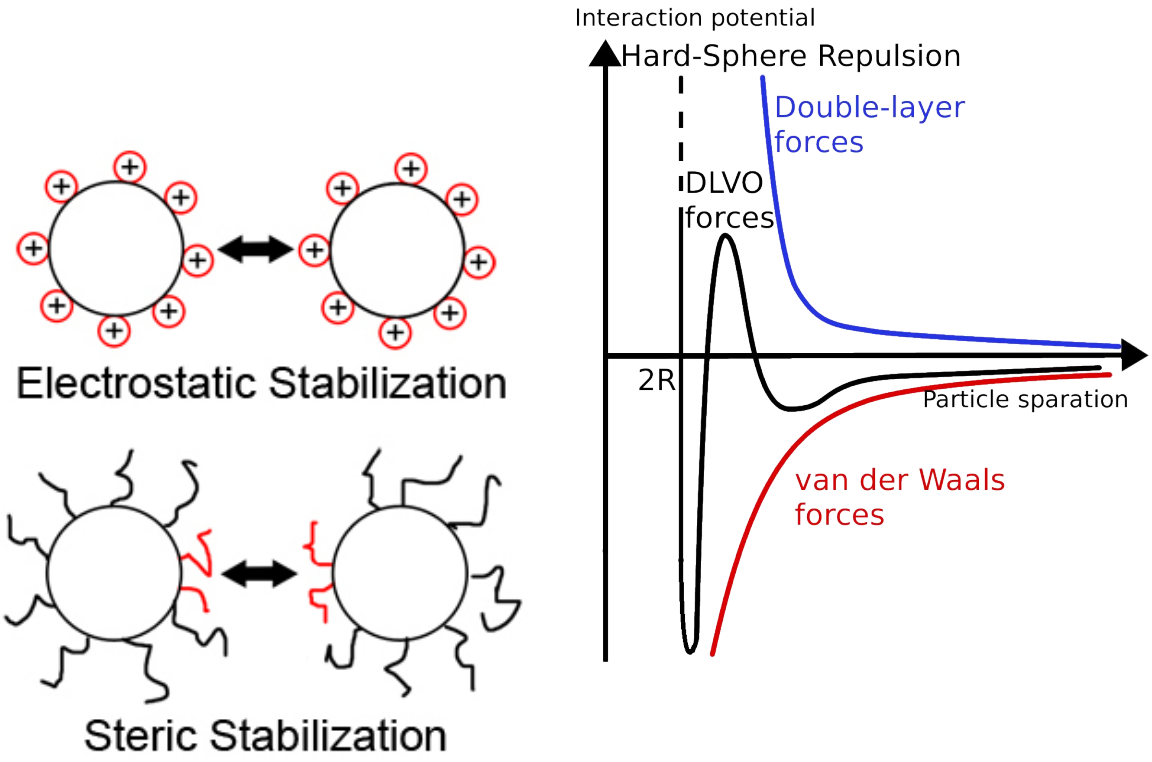

(a) Illustrated depletion interactions.

(b) Illustrative plot of the effective interaction potential.

Figure 2.2: Stabilization mechanisms and particle interactions.

If these were the only forces acting on the particles, the system would become unstable causing the particles to aggregate. However, this can be overcome by adding repulsive forces in two ways: Either the surface chemistry of the particles is changed or the electrostatics of the particle and its surrounding medium. The first method is also called steric stabilisation, where polymer brushes are attached to the particles causing them to repel each other. This is the case for Polymethyl Methacrylate (PMMA) particles, which are yet the best systems to be described by the hard-sphere model [13]. These brushes generate repulsive forces due to entropic reasons and prevent the formation of particle clusters. Around each particle exists an excluded volume, which overlaps when two particles get close to each other, causing them to separate (see fig. 2.2a).

Another method to prevent aggregation is through electrostatic stabilization, where the particle surfaces are being charged so they repel each other. To tune this interaction,

counterions can be added to the surrounding medium in controllable amounts, thus creating a double layer around each particle (see fig. 2.2a). If the particles get into their interaction range, a repulsive force is driving them away from each other. The corresponding potential can be expressed through the following equation

$$V_{EL} = \frac{64\pi R k_B T c_0 \Gamma_0^2}{\kappa^2} \exp\{-\kappa(r-2R)\} \ , \tag{2.4}$$

where

$$\Gamma_0^2 = \frac{\exp\{\zeta e\Phi_0/2k_BT\}-1}{\exp\{\zeta e\Phi_0/2k_BT\}+1} = tanh\Big(\frac{\zeta e\Phi_0}{4k_BT}\Big) \ . \tag{2.5}$$

For small surface potentials Φ_0 of the particles eq. (2.5) can further be simplyfied into $\Gamma_0^2 \approx \frac{\zeta e\Phi_0}{4k_BT}$. κ^{-1} is the Debye length, which tells when Φ_0 drops to e^{-1} of its total value [1]. For a colloidal suspension, it is defined as

$$\kappa^{-1} = \sqrt{\frac{\varepsilon_r \varepsilon_0 k_B T}{2\times 10^3 N_A e^2 I}} \ , \tag{2.6}$$

of which the values that were not mentioned previously are the ionic strength I of the electrolyte in molar units, the permittivity of free space ε_0, the dielectric constant ε_0, N_A is the Avogadro number and the elementary charge e. To calculate the full repulsive potential V_R one has to know the electrolyte concentration c_0 in mol/m^3 and for Γ_0 the valency ζ of the counterion species. All of these values mentioned above can be found in the corresponding literature.

The full interaction potential is obtained by adding up all repulsive and attractive forces

$$V_{tot} = V_{DLVO} = V_{HS} + \frac{64\pi R k_B T c_0 \Gamma_0^2}{\kappa^2} \exp\{-\kappa(r-2R)\} - \frac{A_H R}{12(r-2R)} \ . \tag{2.7}$$

This is the so-called DLVO potential named after Boris Derjaguin, Lev Landau, who developed this theory for charged-stabilised colloidal suspensions in 1941, and Evert Verwey and Theodoor Overbeek seven years later in 1948 [14].

In fig. 2.2b a typical shape of the potential is depicted along with the curves for the repulsive and attractive part. At distances below $2R$, the particles can not overlap and thus the interaction potential goes to infinity around $r \approx 2R$. For slightly larger distances $r > 2R$ the attractive van der Waals force becomes the strongest, counteracting even the repulsion from the double layers. Its strength quickly drops at greater distances, where the electrostatic repulsion then dominates the interaction. Since this part can be tuned via the counterion concentration, the shape of the potential can vary strongly. The parameters can be chosen in a way, that their form approximates that of the hard-sphere potential and the inter-particle interactions can be simplified by the hard-sphere potential [13, 15].
In this work, the particles are stabilised by monovalent sulfate groups on 5 % to 10 % of the

surface of the particles. The remaining part is covered with hydrophilic stacked benzene rings [16].

2.1.2 Hard Sphere Phase Behaviour and Crystallisation Mechanisms

Colloidal particles modelled as hard spheres (HS), can undergo phase transitions only by changing their volume fraction $\phi = N\,V_p/V_{tot}$, which is defined as the volume of all particles $N\,V_p$ in relation to the total volume of the system V_{tot}. HS samples differing from each other only by volume fraction express different phases, ranging from liquid over liquid-solid coexistence to ordered solids [17]. E. g. at first a less dense ordered crystal can be formed at a volume fraction of $\phi_c \geq 0.545$ while an increase of particles leads to an amorphous structure from $\phi_g = 0.58$. At even higher fractions first a Random Closed Packing (RCP) is formed at $\phi_{RCP} = 0.64$ [18]. By a process of crystallisation by vibration, e. g. as in granular crystallisation, the structure will become more ordered fig. 2.3 and reaches $\phi_{CP} = \pi/(3\sqrt{2}) \approx 0.74$ the highest possible packing of spheres with a so called hexagonal close packing (hcp-lattice) [19]. This has been proven by Carl Friedrich Gauss in 1831. Amorphous solids or glasses are materials with a typical relaxation timescale of the order of or larger than the typical duration of an experiment or a numerical simulation [20]. The existence of a link between crystallisation and glass transition is a topic of current research.

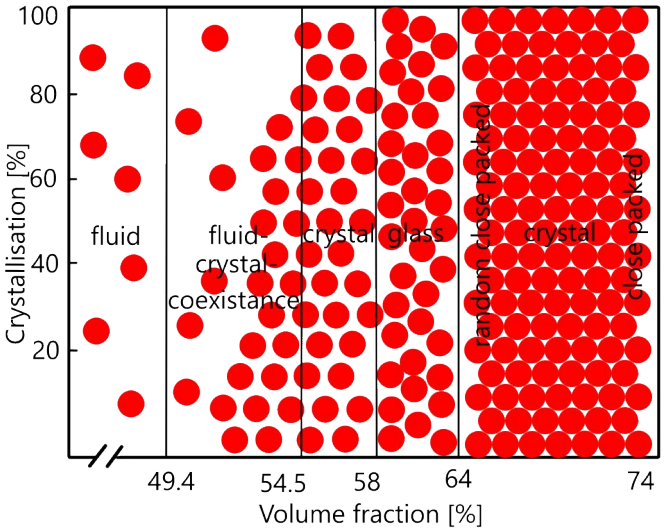

Figure 2.3: Hard-sphere-state-transition diagram for 3D-systems dependent on volume fraction.

In general, phase transitions can be explained by a system's drive to choose a configuration with the lowest free energy. For this, the fundamental thermodynamic equations are considered. These equations describe how the four thermodynamic quantities of a system, the internal energy U, the enthalpy H, the Gibbs free energy G and the Helmholtz free energy F, depend on variables that can be controlled and measured experimentally. E. g.

the equation for the Helmholtz free energy F is defined as [21]

$$F(T, V, N) = E - TS \ , \tag{2.8}$$

with the natural variables, energy E, temperature T and entropy S of the system. Furthermore, F is dependent on the temperature T, the volume V of the system and the number of particles N respectively.
The Gibbs free energy on the other hand is defined as

$$G(p, T, N) = U + pV - TS = H - TS \ , \tag{2.9}$$

with the internal energy U of the system, pressure p, temperature T, volume V and entropy S and is dependent on the pressure, the temperature and the particle number N of the system. It has a similar form as the Helmholtz free energy eq. (2.8), with the enthalpy $H = U + pV$ in place of the energy E. The enthalpy of a system is briefly defined as the heat absorbed or produced during any process at constant pressure [22].

It has been found that local ordering, which can be either entropy or energy-driven, leads to different resulting structures [23].
For hard spheres without external potential, ordering in liquids is purely entropy-driven and it can be split into configurational and vibrational entropy [24]. Crystallisation starts, when vibrational (correlational) entropy rises in favour of configurational entropy [24]. If an external potential is added, e. g. via optical tweezers, then the ordering is also driven by the external energy, which leads to the appearance of new favoured structures. In an optical tweezers setup, the external potential can both be attractive and repulsive depending on the particle's refractive index relative to the medium. This will be discussed in more detail in section 2.2. In general, crystallisation via nucleation can be split into classical and non-classical theories. In Classical Nucleation Theory (CNT) an ordered aggregate is formed via spontaneous particle fluctuations. If a critical size is reached, the aggregate keeps growing into a crystal with a structure, which is already predefined by the nucleus.
From the Gibbs free energy, the critical radius r_c of the nucleus can be derived

$$r_c = \frac{2\gamma}{|\Delta g_v|} \ , \tag{2.10}$$

where γ is the surface tension and $|\Delta g_v|$ is the absolute value of the Gibbs free energy per volume [25]. If the nucleus radius r surpasses the critical radius r_c, then the aggregate will rather not shrink but tends to grow into a larger ordered structure. Because for $r > r_c$ the volume contribution to the Gibbs energy dominates over the surface contribution.

In non-classical theories, in contrast to the CNT, an aggregate formed from spontaneous particle-fluctuations is not ordered at first. It turns into an ordered nucleus from the interior, while the boundary gets ordered through gaseous particles from the medium. There are many more nucleation models, but their discussion would exceed the scope of this work.

For more see [26].
This has been observed with magnetic colloidal particles by controlling their mobility through the magnetic field and by driving them into the centre with a concave dish [27]. For slow cooling rates, that is when the particle motion is lowered slowly, the particles form a dense hexagonal crystal in the centre.

When two particles touch they tend to stay together, which is then called a bond [27]. The more of these contacts are made, the higher the stability. A maximum is reached with six neighbours. Therefore, a hexagonal structure is most often found for a solid phase and a crystal is mostly associated with a hexagonal structure. The stability for quasicrystals is achieved differently since hexagons are appearing in dodecagonal (12-fold) symmetries but not for e. g. 10-fold, which are studied in this work. This will be discussed further in section 2.3.1. The next section will cover the background physics and optical phenomena encountered in optical tweezers techniques.

2.2 Optical Forces acting on a Dielectric Particle

It is known, that light carries energy and therefore momentum, which can be transferred to an object. E. g. radiation pressure is caused by a momentum transfer of the electromagnetic field to the objects which are interacting with it.
The incident pressure P_{inc} is given by the incident irradiance I_{inc} divided by the speed of light in vacuum c,

$$P_{inc} = \frac{\langle \mathbf{S} \rangle}{c} = \frac{I_{inc}}{c} \ . \tag{2.11}$$

P_{inc} is calculated from the Poynting vector $\mathbf{S} = \mathbf{E} \times \mathbf{H}$ with the magnetic $\mathbf{H}$ and electric field vector $\mathbf{E}$. $\mathbf{S}$ is a measure of energy transfer per area and time, i. e. representing the energy flux.

Effects of radiation pressure are appearing on different length scales: Macroscopically, solar radiation pressure can affect the shape of a comet's tail by interacting with its dust particles. On the mesoscopic length scale, it forces micron-sized dielectric particles to move in the direction of a laser beam, as done by Ashkin in 1970 [28]. To manipulate objects in three dimensions, the so-called gradient force needs to be considered additionally to the forces exerted by the radiation pressure. In this case, a high intensity of the light source and/or small size of the manipulated object is favourable. This has an application in optical tweezers, which also have been elaborated by Ashkin et al. [29]. On even smaller length scales the transfer of momentum from light is used to manipulate atoms like in laser cooling, e. g. to the quantum ground state, [30], which could be useful for quantum computing.

In the case of optical tweezers, a beam with a high-intensity Gaussian TEM_{00} profile and low power fluctuations [31] is required. Therefore, a laser source is ideal. Moreover, to manipulate colloidal particles, it also needs to be tightly focused. This creates a restoring force, which is able to move particles of a diameter in the range of 10 nm to 50 µm. A Gaussian mode focuses on the smallest diameter beam waist, which will produce the most efficient, harmonic trap. For the focus an objective with a high numerical aperture is needed in an inverted microscope, so the laser can enter the optical path before the objective.

To explain the trapping process, the ray optics regime will be considered. If the particle can be regarded to be much larger than the wavelength of the beam, i. e. $d/\lambda >> 1$, diffraction effects can be neglected. Here, the acting forces will be described through the refection and refraction of rays at the surface of the spherical particle. Calculations for ray optics have already been done by Ashkin for a TEM_{00} as well as a doughnut-shaped TEM_{01}^{*} beam profile [28].

The particle is driven to and held in the focus of a beam mainly by two forces, which arise from the change in the total momentum of the beam: Firstly, the scattering force $\mathbf{F_{scat}}$ originating from the radiation pressure of light, which pushes the particle in the direction

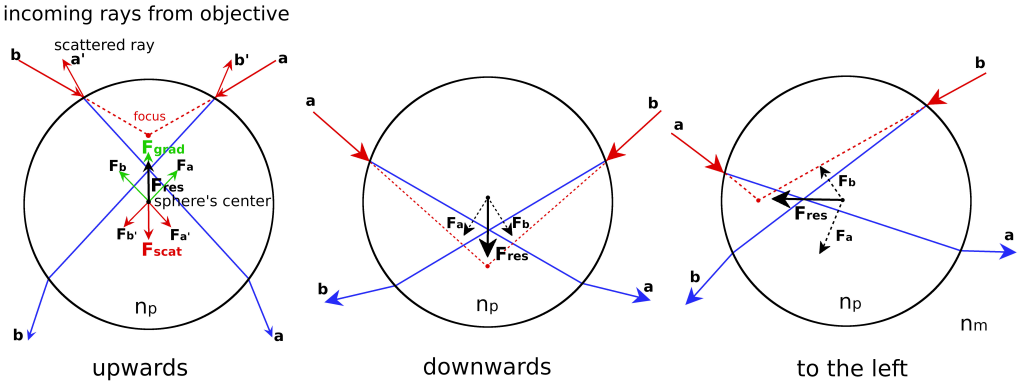

Figure 2.4: A schematic ray diagram for three cases of a laser beam hitting a spherical particle for optical trapping. The resulting force is always driving the sphere into the focus. Redrawn after [32].

of the incidence light propagation or away from its source. Secondly, the gradient force $\mathbf{F_{grad}}$ arising from a radial intensity gradient in the Gaussian beam [31], pushes the particle towards the focus of the laser beam. The gradient force has to be greater than the scattering force for a particle to get trapped.

In ray optics, the particle can be regarded as a converging or diverging lens depending on the difference in the refracting index of the particle n_p and its surrounding medium n_m (fig. 2.4).
In detail, for $n_p > n_m$ several cases can be imagined as illustrated in fig. 2.4. In the case of axial trapping, the particle moves upwards or downwards towards the focus. This is due to the gradient force pointing to the focus from momentum transfer of the refracted rays, being larger than the scattering force pointing in the opposite direction stemming from the scattered rays. Therefore, the resulting force $\mathbf{F_{res}} = \mathbf{F_{grad}} + \mathbf{F_{scat}}$ is pointing to the trap's focus.
If $n_m > n_p$ then the opposite case is true, where the scattering force dominates over the gradient force. The particle will be repelled by the laser beam in the direction of propagation aways from the focus of the trap. This is the reason why the particle's refractive index has to be larger than that of the surrounding medium for the successful trapping of a particle.

In the case of lateral trapping the gradient force will point to the steepest increase of intensity. Hence, by using a beam with a Gaussian profile, the gradient force will point to the focus. If it dominates over the scattering force in case of $n_p > n_m$, the resulting force always drives the particle to the focus of the trap.
All in all, the particle will be driven towards the focus by a combination of lateral and axial trapping by using a highly focussed, high-intensity Gaussian beam and a refractive index which is larger than that of its surrounding medium.

The so-called Rayleigh regime is applied, if the particle size d is much smaller than the

wavelength λ of the light source, i. e. $d << \lambda$. For polystyrene particles in water like those used in this thesis, this regime would be valid for particle radii with $R \lesssim 0.7\,\lambda \sim 0.372\,\mu m$ [33]. Then the particle is treated as a point dipole and the scattering force pointing in the direction of the light propagation is described as

$$\mathbf{F_{scat}} = \frac{I_0 \sigma_s n_m}{c} \ . \tag{2.12}$$

It is dependent on the incident intensity I_0, the refractive index of the medium n_m and the scattering cross-section of the sphere [31].

$$\sigma_s = \frac{8}{3}\pi (kr)^4 r^2 \left(\frac{n^2-1}{n^2+2}\right)^2 \tag{2.13}$$

with particle radius r and wave vector k. The gradient force pointing in the direction of the steepest increase of intensity is defined as

$$\mathbf{F_{grad}} = \frac{2\pi\alpha_s}{c n_m^2} \nabla I_0 \ , \tag{2.14}$$

with the polarisability of a sphere [31]

$$\alpha_s = n_m^2 a^3 \left(\frac{m^2-1}{m^2+2}\right)^2 \ . \tag{2.15}$$

For the total time-averaged force acting on a sphere in the Rayleigh regime, these two contributions can be merged into one expression [34]

$$\langle F^i \rangle = \frac{1}{2} \mathfrak{Re}[\alpha E_{0j} \partial^j (E_0^j)^*] \ , \tag{2.16}$$

with the complex magnitude of the electric field E_0 and a generalised polarisability

$$\alpha = \alpha_s (1 - \frac{2}{3} i k^3 \alpha_s)^{-1} \ , \tag{2.17}$$

where α_s is the polarisability of a sphere (eq. (2.15)). Eq. 2.16 can be valid also for larger particles with the coupled dipole method [31].

The generalised Lorentz-Mie theory (GLMT) is the most complete theory to describe the forces on a dielectric particle in an optical trap, where $R \approx \lambda$ is valid like for many soft matter objects. Although it is complex it is still helpful to determine the capabilities of an optical tweezers setup and can be simplified e. g. with the second-order Rayleigh theory,

which is the Rayleigh theory extended by a second order scattering term to be valid for larger particles [31]. In this work, the smallest particle diameter is about $d = 2.1\,\mu m$ and the wavelength of the laser is $532\,nm < d$. That means, that $d/\lambda = 2.1\,\mu m/0.532\,\mu m >> 1$ holds, and it is reasonable to describe the trapping process in the ray optics regime.

2.3 Quasicrystals

In general, crystals are defined as periodic arrangements of unit cells into structures with translational and orientational order [35]. In the case of orientational order, only rotational symmetries are allowed, that do not break the translational symmetry, e. g. 2-, 3-, 4- or 6-fold symmetries. However, in 1984 Shechtman et al. found structures in aluminium manganese alloys with higher rotational symmetries, which are incompatible with translational symmetry [36]. Such structures with quasiperiodic configurations are named quasicrystals since traditional crystallographic rules are not applicable here. Instead of having a translational order, they possess a long-range orientational order. For one this means, that the periodicity is only revealing itself when the order is analysed for long distances between the atoms or particles [36]. Secondly, the order is orientational, meaning that the arrangement follows tiling rules, which are specific for each rotational symmetry. Because of these properties the usual methods in crystallography can not be applied.

Quasicrystals show unique physical and chemical properties, which can be interesting for possible applications. Some materials have a capacity to store hydrogen efficiently, e. g. which could be useful as hydrogen-storage materials for the future energy economy [37]. Furthermore, quasicrystals can be used in infrared detectors, selective absorbers for solar photothermal converters and active elements for thermoelectric devices [38]. High rotational symmetries like in 12-fold quasicrystals are favourable for novel photonic bandgap devices, where the propagation of electromagnetic waves or the spontaneous emission of light is forbidden [21].

For soft matter systems in 2004 by Zeng et al., where supermolecular dendrimers have been found to form quasicrystalline structures [39]. Since then they have also been found in various other soft matter systems with micelles [21] or colloids [21], the most frequent symmetry being 12-fold (dodecagonal). Because of their large length-scale soft matter quasicrystals are good model systems to study these materials more easily e. g. with visible light.
In this work, 10-fold symmetry will be analysed by studying the alignment and dynamics of colloidal particles in a decagonal (10-fold) light field.

2.3.1 Stability Mechanisms in Quasicrystals

A tiling is the space-filling arrangement of tiles with no overlaps or gaps. Quasicrystalline tiles are not to be confused with a unit cell of crystals, since the first possess no periodic translational order in comparison to the latter [35]. Every quasicrystalline symmetry has its own set of tiles making up the structure. Although some tiles occur for several symmetries, the occurrence and combination of tiles are unique for each symmetry. In dodecagonal tilings, squares and equilateral triangles can be found in a specific ratio of fractions [40]. A decagonal tiling can be broken down into two kinds of isosceles triangles, short and long ones, which can be assembled into larger building structures. E. g. the so-called "Tübingen" or "Tuebingen" tiling [41], which will be the template structure for this thesis, is made up of pentagons, hexagons and nonagons (fig. 2.5). The two length scales, which can be found in these tilings, play an important role in their stabilisation, i. e. the side lengths of the squares and triangles and the side lengths of the pentagons and triangles respectively.

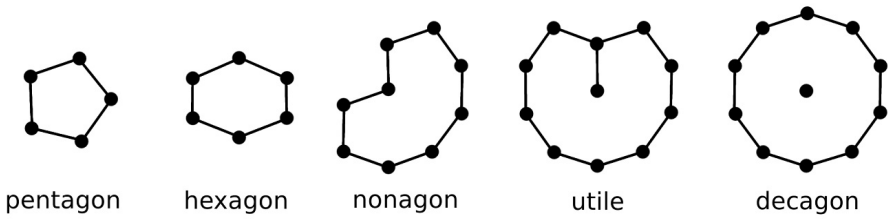

Figure 2.5: Basic tiles as building blocks of a decagonal quasicrystal.

Therefore, the formation of quasicrystals is facilitated by an interaction potential with two length scales due to the competition of nearest neighbour distances. Examples are purely attractive potentials with two minima or a repulsive shoulder and soft-shell model [42]. Depending on their attractive or repulsive nature and on the ratio between the two length scales, many different complex structures can emerge. Some examples are the square-well [43, 44], Lennard-Jones-Gauss [45, 46] and square-shoulder interaction potentials [47]. The formation of colloidal 12-fold quasicrystals is found to be facilitated by an isotropic interaction potential with at least two incommensurate length scales [48]. This is due to the fact, that the most abundant tiles in dodecagonal quasicrystals are the square and the triangle. Upon assembly of these tiles, two dominating length scales can be found, e. g. the side length of the rectangles and triangles and the ratio of them [49].

Similarly, for stabilising 10-fold quasicrystals, the two main lengths stem from the smallest building blocks as the regular pentagons, namely its side length and diagonal (fig. 2.5). However, the pentagon can also be broken down into 3 triangles, where the centre one is a so-called golden triangle formed from the two length scales (see fig. 2.6a).

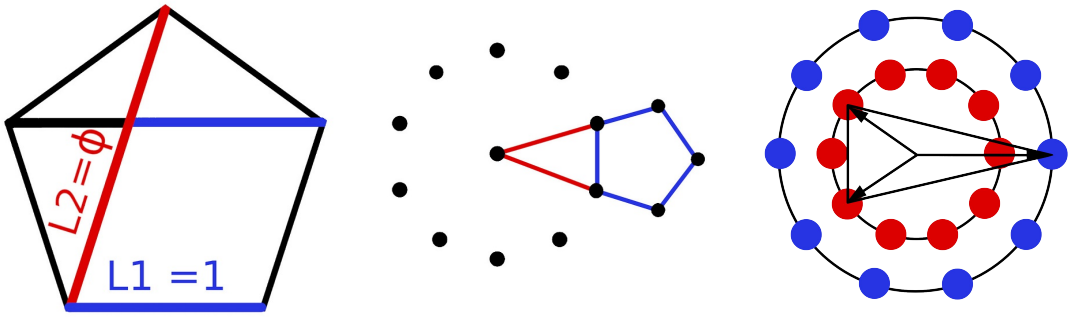

(a) Regular pentagon with side length 1.

(b) Pentagon and golden triangle in a decagonal tiling.

(c) Lifshitz-Petrich stabilisation mechanism.

Figure 2.6: Tiles in decagonal quasicrystals: (a) The length ratio in a regular pentagon $\frac{L2}{L1} = \phi \approx 1.618$ is the golden ratio. (b) Short (blue) and long (red) lengths in decagonal tilings. (c) Illustration of vector cancellation on a decagonal diffraction pattern for reaching a free energy minimum after the Lifshitz-Petrich model (eq. (2.20)), redrawn after [50].

Although 12-fold rotational symmetry is more common in soft matter quasicrystals [51], in this work colloidal particles will be studied in light field potentials with 10-fold symmetry. More about the creation and properties of these quasicrystal templates will be presented in section 3.5.

The formation of quasicrystals is highly complex and still not fully understood [52]. Two different growth regimes have been observed so far. Either defect-free quasicrystals stabilised by energy or metastable locally disordered random tilings stabilised by entropy [21]. For each case, the dominant mechanism of stability is a different one [53].
Entropically stabilised tilings can be described by the so called random tiling models. These have been used to overcome problems when constructuing quasicrystalline tilings. E. g. for one, there need to be some imperfecions in the final structure and secondly it's impossible to apply strict local growing rules for perfect quasicrystals [54].
Therefore, models have been created with stochastic approaches to solve the stabilisation mechanism with contributions from configurational entropy. A set of tiles can join in a random manner and edge-matching rules do not have to be applied [53].

This process is also called entropy-driven reconfiguration [55], which is reversible and it allows for the appearance of degenerate states. Hence a state exists with maximum entropy and long-range order [56]. It can be shown, that the deviations from perfect quasicrystal tilings by rearrangement and imperfections do not destroy the diffraction pattern [57]. As will be further discussed in the next section, quasicrystals can show some disorder in the form of diffusion, where the local structure can rearrange to redistribute stresses in the structure. The random tiling model is an accurate model for most quasicrystals since it describes the diffuse scattering resulting from these diffusive modes. It manifests itself in the background of the structure factor of random tilings additionally to the Bragg peaks

[53]. Perfect quasicrystals stabilised by energy are on the other hand a very rare occurrence in quasicrystals found in nature.

For a more mathematical viewpoint on stability in quasicrystals, an equation based on the Swift-Hohenberg equation has been elaborated by Lifshitz and Petrich [58]. To obtain the length scales which stabilise the desired structures, one has to minimise the free energy, which will be expressed by a free-energy functional $\mathcal{F}_{LP}(u(\mathbf{r}))$. $u(\mathbf{r})$ is the order parameter described as a scalar field which for soft matter systems is the density profile.
The partial differential Swift-Hohenberg equation (SH-equation), found by Swift and Hohenberg in 1977 [59], is a model for crystallisation of a fluid in equilibrium and can describe the process of pattern formation [60]. Since quasiperiodic patterns are possible for this model, it can therefore be useful to predict and control the formation of stable quasicrystalline symmetries from disordered structures, where $u(\mathbf{r}) = 0$ holds.

It reads

$$\partial_t u = \varepsilon u - (\nabla^2 + 1)^2 \cdot u - u^3 \ , \tag{2.18}$$

where $u = u(\mathbf{r})$ is a two-dimensional scalar field that describes the relative deviation $(c(\mathbf{r}) - \bar{c})/\bar{c}$, e. g. of a coarse-grained density $c(\mathbf{r})$, from its mean value [50]. The quadratic divergence term stems from the description of pattern formation via density gradients comparable to the description of phase separations.

Lifshitz and Petrich extended the SH-equation by a Landau free-energy expansion to study parametrically-excited liquid surface waves [58]

$$\partial_t u = \varepsilon u - (\nabla^2 + 1)^2(\nabla^2 + q^2)^2 \cdot u + \alpha u^2 - u^3 \ , \tag{2.19}$$

where the parameter α characterises third-order interactions and the pairwise interactions are controlled by a temperature-like parameter ε. The ratio of the two main lengths is denoted by q, which is a control parameter for this system and will be defined later in this section.

It has been found that these liquid surface waves can form quasiperiodic standing-wave patterns (Faraday waves) for a superposition of two temporal frequencies that require two spatial length scales for stable structures [50].
With $\partial_t u = -\frac{\delta \mathcal{F}_{LP}}{\delta u}$ (Model A by Hohenberg and Halperin [61]) the generalised effective free energy reads

$$\mathcal{F}_{LP} = \frac{\gamma}{2} \int \left[(\nabla^2 + 1)^2(\nabla^2 + q^2)u(\mathbf{r})^2\right]^2 \mathrm{d}\mathbf{r} + \int \left[-\frac{\varepsilon}{2}u(\mathbf{r})^2 - \frac{\alpha}{3}u(\mathbf{r})^3 + \frac{1}{4}u(\mathbf{r})^4\right] \mathrm{d}\mathbf{r} \ , \tag{2.20}$$

where the parameter γ is the so-called energy penalty factor [62].
For $\mathcal{F}_{LP}$ to reach a minimum, the first integral in eq. (2.20) with quadratic divergence terms, defines the selection of two length scales with the ratio q.

The free energy is approximated as an expansion of the concentration gradient. Since we're looking for extrema of the free-energy functional in this optimisation problem, the values around the minima are negligible. Therefore, the quadratic divergence term is the lowest non-vanishing order.

It can be shown, that the free energy is minimal if there exist triplets of density modes with wave vectors restricted by the ratio q, which cancel each other out. That is quasicrystals are favourable when the wave vectors are restricted to lie on two concentric rings at 1 and q. Visually this means, when the sum of two unit wave vectors ($k = 1$) separated by $2\pi/n$ pointing to one ring in the diffraction pattern and a third wave vector $k = q$ pointing to a second ring is zero, a free energy minimum is reached for $\mathcal{F}_{LP}$ [60] (see fig. 2.6c). The ratio q between these rings can be calculated for N-fold symmetry with

$$q = 2\,\cos\left(\frac{\pi}{n}\right)\,, \tag{2.21}$$

where N is equal to n for even or $2n$ for odd integers n, as has been elaborated by Barkan and inspired by Lifshitz and Petrich [60]. Therefore, a quasiperiodic pattern can be obtained as a minimum of $\mathcal{F}_{LP}$, which is stabilised by two dominant lengths with a ratio q in the pair potential. For decagonal symmetry with $n = 5$, $q \approx 1.618 = \phi$, where ϕ is the golden ratio (eq. (3.7)) and will be discussed in more detail in section 3.5.

An extension of the Lifshitz-Petrich model is the BDL model, named after Barkan, Diamant and Lifshitz [63], which was specifically developed for soft matter systems. Pair potentials with two length scales can be tailored to control complex self-assembly processes into the desired structures such as quasicrystals with symmetries even greater than 12.

2.3.2 Excitation Modes in Quasicrystals

In solid-state physics, the concept of phonons is used to describe excitations and vibrations of atoms in a solid. E. g. more generally speaking phonons describe how heat is moving through the solid through oscillations of atoms or particles around their equilibrium position [64]. Collective thermal motions are then called phononic modes. In quasicrystals additionally to phonons so-called phason excitation is possible, for which no counterpart in periodic solids exists.
These complex rearrangements of particles can be observed in metastable quasicrystals as phasonic flips, which cause local defects [52]. Like Brownian motion, phasonic displacements can be caused by thermal fluctuations. Phasons can induce diffusion in a quasicrystal and rearrange its structure only restricted by its internal geometry, while the quasicrystal's symmetry is globally always preserved [65]. They are unique in quasicrystals due to their additional degrees of freedom from non-periodicity. Correlated excitations of phasons do

not cost any energy within the limit of long wavelengths [52]. Phasonic modes facilitate the formation of dislocation-free quasicrystals since during crystal growth the stress due to incommensurate distances is lowered [66]. Whereas in periodic crystals phononic strain fields alone can not redistribute the stress resulting in dislocations. E. g. repair processes by phason relaxation, rather than a local growth rule, plays an essential role in the construction of ideal quasicrystalline order in real materials [67].

In the case of entropically stabilised quasicrystals like described by the random tiling model (section 2.3.1), phason modes contribute to configurational entropy and hence to the stability of the quasicrystal [68]. The induced diffusion by phason modes results in diffusive scattering, which can be seen in the diffraction patterns of quasicrystals as diffuse noise around the Bragg peaks [68]. The structures in this work do not show these collective dynamics since the quasicrystalline symmetry is induced by the light field. However, the particles show Brownian motion and diffusive behaviour, which can be separated into different regimes. In the following the concept of Brownian motion and diffusion will be introduced, together with mathematical methods to describe the particle dynamics.

2.4 Dynamics of Brownian Particles

Brownian Motion was observed for the first time in 1827 by the Scottish botanist Robert Brown. When studying pollen immersed in water under a microscope, he observed a motion, that couldn't be traced back to currents in the fluid e. g. like drift motion. After studying old dried pollen samples, he was convinced, that it was not a motion exclusive to living matter. Later his discovery has been described mathematically by several people including Einstein in 1905, who deduced it independently without knowledge of Brown's observations.

Brownian motion arises from thermal fluctuations, which cause the transfer of momentum from molecules in the solution to the colloids [69]. Although it is a microscopic description of short times, the effects of Brownian motion can be seen on all length scales. E. g. even in astrophysics it is used to describe stellar dynamics [70]. On both length scales a cumulative effect leads to a small measurable change in velocity of the colloid/star because of a high number of collisions/encounters during a certain time interval (on the order of 10 years for stars and microseconds for micron-sized particles).

Since Brownian motion has no defined direction, it can be described by a random walk model. Here, the particle's behaviour is described as that of a random walker, who repeatedly covers a distance in a random direction, starting a new step independent from the previous one. This process goes on and a random walk is created, which as a series of discrete independent steps S_n describes the trajectory of a Brownian particle very well. For one dimension this stochastic process reads

$$S_n = \sum_{k=1}^{n} X_k \ , \tag{2.22}$$

where the steps X_k are independent and $S_0 = 0$. It can be shown, that the probability density to find the walker in an interval $[x, x + dx]$ is a Gaussian [71]

$$P(x,t) = \frac{1}{\sqrt{4\pi D t}} \exp\left\{ -\frac{x^2}{4Dt} \right\} \tag{2.23}$$

with the diffusion coefficient D. This is only true if at time $t = 0$ the initial PDF is described by the Dirac-Delta $P(x, t = 0) = \delta(x - x_0)$, where x_0 is the particle's initial position.
On the other hand, there are occasions where the model of discrete steps is not used, e. g. in the description of the movement in a harmonic potential as will be shown in section 2.4.4.

2.4.1 The Van Hove Distribution Function

To describe the dynamics and structure of a system, a central quantity is the so-called van Hove distribution function, named after the Belgian physicist and mathematician Léon van Hove [72]. It is defined as the probability of finding a particle at a position $\mathbf{r}$ at time $t_0+\Delta t$, given that there was a particle at $\mathbf{r_i}$ at time t_0 [73]

$$\mathcal{G}(\Delta\mathbf{r},\Delta t)=\frac{1}{N_P}\left\langle\sum_{i=1}^{N_P}\sum_{j=1}^{N_P}\delta[\Delta\mathbf{r}-(\mathbf{r}_j(t_0+\Delta t)-\mathbf{r}_i(t_0))]\right\rangle . \tag{2.24}$$

$\delta()$ is the Dirac delta function, which is used in the microscopic definition of the local density of a particle

$$\rho_n(\mathbf{r},t)=\sum_{i=1}^{N_P}\delta[\mathbf{r}-\mathbf{r}_i(t)] . \tag{2.25}$$

This definition of density is not to be confused with the macroscopic particle concentration $n(\mathbf{r},t)\neq\rho_n(\mathbf{r},t)$

With this, eq. (2.24) can be rewritten as

$$\begin{aligned}\mathcal{G}(\Delta\mathbf{r},\Delta t)&=\frac{1}{N_P}\left\langle\sum_{i=1}^{N_P}\delta[\Delta\mathbf{r}-(\mathbf{r}_i(t_0+\Delta t)-\mathbf{r}_i(t_0))]\right\rangle\\&+\frac{1}{N_P}\left\langle\sum_{i=1}^{N_P}\sum_{\substack{j=1\\j\neq i}}^{N_P}\delta[\Delta\mathbf{r}-(\mathbf{r}_j(t_0+\Delta t)-\mathbf{r}_i(t_0))]\right\rangle\\&\equiv\mathcal{G}_s(\Delta\mathbf{r},\Delta t)+\mathcal{G}_d(\Delta\mathbf{r},\Delta t) ,\end{aligned} \tag{2.26}$$

consisting of a self part $\mathcal{G}_s(\Delta\mathbf{r},\Delta t)$ and a distinct part $\mathcal{G}_d(\Delta\mathbf{r},\Delta t)$ [74]. If a particle i is in $\mathrm{d}\Delta\mathbf{r}$ around $\mathbf{r_i}$ at the initial time t_0, then $\mathcal{G}(\Delta\mathbf{r}\Delta t)\mathrm{d}\Delta\mathbf{r}$ can be interpreted as the probability to find another particle j in $\mathrm{d}\Delta\mathbf{r}$ at later time $t_0+\Delta t$ [1].
For the description of the self part $\mathcal{G}_s(\Delta\mathbf{r},\Delta t)$ like the name states, only one particle i is considered. It gives the probability of finding it displaced by $\Delta\mathbf{r}$ at $t_0+\Delta t$ after it has been at $\mathbf{r_i}$ at t_0. The explanation for the distinct part is similar, only that the particle j, which is found at $\mathbf{r_i}$, is a different one than the particle i displaced by $\Delta\mathbf{r}$.

Both parts can be used to describe different aspects of a sample. E. g. for $\Delta t=0$ the distinct part becomes $g(\Delta\mathbf{r})\cdot\rho(\mathbf{r})$ with the so-called pair distribution function $g(\Delta\mathbf{r})$. For homogeneous systems $\rho(\mathbf{r})=\rho$, it becomes the radial correlation function $g(r)$, which describes the particle distribution from the distance of a reference particle at the origin and

hence is used for analysing the structure of a sample.
The self part $\mathcal{G}_s(\Delta\mathbf{r}, \Delta t)$ is used for estimating the Probability Density Function (PDF)

$$\frac{\partial \mathcal{G}_s(\Delta\mathbf{r}, \Delta t)}{\partial \Delta t} = D_l \nabla^2 \mathcal{G}_s(\Delta\mathbf{r}, \Delta t) \ , \tag{2.27}$$

where D_l is the self-diffusion coefficient for long times. Thus for pure Brownian motion in a homogeneous medium $\mathcal{G}_s(\Delta\mathbf{r}, \Delta t)$ can be approximated as a Gaussian [75]

$$\mathcal{G}_{s,B}(\Delta\mathbf{r}, \Delta t) = (4\pi D_l t)^{-d/2} \exp\left\{-\frac{\Delta\mathbf{r}^2}{4D_l \Delta t}\right\} = P_B(\Delta\mathbf{r}, \Delta t) \ , \tag{2.28}$$

where d is the dimensionality.

All in all, $\mathcal{G}(\Delta\mathbf{r}, \Delta t)$ is an important tool for the analysis of particle dynamics and structure.

2.4.2 Diffusion and Mean Squared Displacement

Diffusion is a collective process, hence not a single particle but a collective of particles is considered. Mathematically it is described in three laws, which are called after Adolf Fick, who derived these equations in 1855. Calculations and definitions will be done in one dimension for clarity here, but are valid equally in higher dimensions.
The first law of Adolf Fick describes the change of the particle concentration $n(x, t)$ in time and space with the diffusion flux J, the diffusion coefficient D and the gradient of particle concentration [69],

$$J = -D\frac{\partial n(x, t)}{\partial x} \ . \tag{2.29}$$

The particle concentration $n(x, t)$ used here, is defined as the number of particles per volume and meant as a macroscopic quantity. From the continuity equation for mass the change in particle density equals the change in flux,

$$\frac{\partial n}{\partial t} = -\frac{\partial J}{\partial x} \ . \tag{2.30}$$

Together with Fick's first law eq. (2.29), this leads to his second law also known as the diffusion equation

$$\frac{\partial n}{\partial t} = D\frac{\partial^2 n}{\partial x^2} \ . \tag{2.31}$$

It describes the time and space dependence of a particle distribution $n(x,t)$ and can be solved by a Gaussian function of the form

$$n(x,t) = \frac{1}{\sqrt{4\pi D t}} \exp\left\{-\frac{x^2}{4Dt}\right\} , \tag{2.32}$$

with

$$D(t) = \frac{k_B T}{6\pi\eta R_h} . \tag{2.33}$$

The fluctuations from the diffusion of particles in thermal equilibrium are related to the energy dissipation in non-equilibrium, which is stored in the viscosity η of the friction coefficient $\xi(t) = 6\pi\eta R_h$ [69]. R_h is the hydrodynamic radius as a measure for the particle size. More on this in section 3.1.1.
Systems, which obey Fick's laws presented above, show normal diffusion behaviour. However, usually, this is not the case, if the sample is exposed to external forces, e. g. gravity.

The Mean Squared Displacement (MSD) is a measure for the width of the distribution of particle positions during a given time Δt [69] and therefore used to quantify the particle's mobility. To mathematically describe and calculate the MSD, the PDF will be presented first along with the concept of moments for describing probability distributions in general.

The PDF for diffusive particles in one dimension can be written as

$$P(\Delta x, \Delta t) = \frac{1}{\sqrt{4\pi D \Delta t}} \exp\left\{-\frac{\Delta x^2}{4D\Delta t}\right\} . \tag{2.34}$$

For characterisation, one needs to consider the moments, which quantify the shape of the function. This is important in particle dynamics to discriminate between Brownian motion under various conditions. E. g. the motion can be isotropic or anisotropic like the transport in biological tissue and diffusion in liquid crystals, while still being Brownian [76]. Therefore, it is useful to calculate the moments of a measured distribution function.
Mathematically the n-th moment of a probability density function $\widehat{P}(x)$ is defined by the following integral

$$\mu_n = \int_{-\infty}^{\infty} (x)^n \widehat{P}(x) \mathrm{d}x . \tag{2.35}$$

Moments are generally used in probability theory and statistics. To visualise this concept, it is more convenient to look at how they are used in mechanics. Here, the main function represents the mass density analogous to $\widehat{P}(x)$. Then the zeroth moment will give the total mass, the first moment normalised by the total mass is the centre of mass and the second moment will give the rotational inertia. This shows, that the mathematical concept of moments has a concrete application that can ease its understanding.

If we now go back to a more general point of view, the first raw moment gives the mean of a distribution

$$\mu_1 = \int_{-\infty}^{\infty} (\Delta x)\widehat{P}(\Delta x, \Delta t)\mathrm{d}\Delta x =: \langle \Delta x \rangle \ . \tag{2.36}$$

For pure Brownian motion, it vanishes, since there is no preferred direction in a random walk. The second moment, on the other hand, does not disappear. Calculated around zero, it gives one of the central quantities, the Mean Squared Displacement (MSD)

$$\mu_2 = \langle \Delta x^2 \rangle(\Delta t) = 2D\Delta t \ , \tag{2.37}$$

and can be calculated experimentally from the diffusion coefficient D defined in eq. (2.31). In the case of Brownian motion the MSD is equal to the variance $\sigma^2_{\Delta x}(\Delta t)$ of the PDF, which is the second central moment, since $\langle \Delta x \rangle = 0$ and

$$\sigma^2_{\Delta x}(\Delta t) = \langle \Delta x^2 \rangle - \langle \Delta x \rangle^2 \ . \tag{2.38}$$

Generally, it is a measure for the spreading of values around their average with its root being the well-known standard deviation σ. Analogously the MSD is calculated from the width of the distribution of particle positions in time Δt. The variance can be interpreted with Chebyshev's inequality

$$Pr\{\Delta x \in [\langle \Delta x \rangle - j\sigma_{\Delta x}, \langle \Delta x \rangle + j\sigma_{\Delta x}]\} > 1 - \frac{1}{j^2} \ . \tag{2.39}$$

This means, that at least $100\,(1 - 1/j_2)\%$ of the data will be within $\pm j\sigma$ of the mean and is true for any distribution [77]. In the case of a Gaussian function $j = 1$, 2, and 3 represent 68 %, 95 %, and 99.7 %

In summary, the MSD $\langle \Delta \mathbf{r}^2 \rangle(\Delta t)$ with eq. (2.37) and eq. (2.38) can be written in d dimensions with the position vector $\mathbf{r}$

$$\sigma^2_{\Delta r}(\Delta t) = \langle \Delta \mathbf{r}^2 \rangle(\Delta t) = \langle [\mathbf{r}(t + \Delta t) - \mathbf{r}(t)]^2 \rangle = 2dD\Delta t \ , \tag{2.40}$$

where $\langle \cdot \rangle$ denotes a time-average over t and/or an ensemble-average over several trajectories.

2.4.3 Higher Moments of Probability Distributions and Anomalous Diffusion

The MSD is the first non-vanishing moment of a PDF and therefore central for quantifying particle dynamics. The next important measure is the so-called skewness γ_1 of a distribution,

calculated from the third moment normalised by the cubic square root of the variance $\sigma^2_{\Delta x}(\Delta t)$

$$\gamma_1(\Delta t) = \frac{1}{\sigma^3_{\Delta x}} \int_{-\infty}^{\infty} (\Delta x - \langle \Delta x \rangle)^3 P(\Delta x, \Delta t) \mathrm{d}\Delta x \ . \tag{2.41}$$

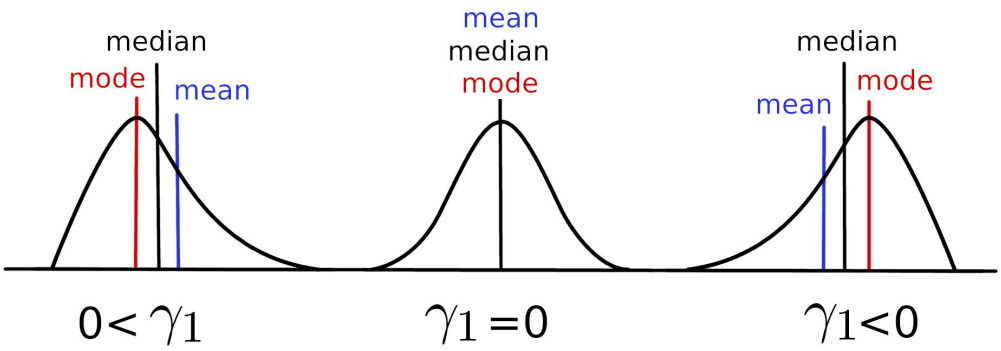

Figure 2.7: Illustration of distributions with different values of skewness.

It measures the asymmetry of a distribution of values around its mean $\langle \Delta x \rangle$ and can either be positive or negative depending on the location of the centre of mass of the distributions, e. g. it is said to be left-skewed or left-tailed for negative skewness (fig. 2.7).

For an ideal normal distribution, the skewness is zero, since it is symmetric around its mean. This is also the case for Brownian motion even with drift and therefore, it is not enough to properly characterise particle dynamics in measurements.

E. g. the mean is defined by the first moment eq. (2.36), but we are used to calculating it by summation of the values and then dividing by their total number:

$$\langle \Delta x \rangle(\Delta t) = \frac{1}{N} \sum_{i=1}^{N} \Delta x_i(\Delta t) \ . \tag{2.42}$$

This is a well-known procedure to calculate the average. Estimates like these are done for many experimentally measured properties. So the variance defined in eq. (2.38) can be estimated from

$$\sigma^2_{\Delta x}(\Delta t) = \frac{1}{N} \sum_{i=1}^{N} (\Delta x_i(\Delta t) - \langle \Delta x(\Delta t) \rangle)^2 \ . \tag{2.43}$$

The formula above is however biased since $\Delta x(\Delta t)$ is already an estimate calculated from eq. (2.42). For the unbiased variance, one has to divide by $(N-1)$ instead

$$\tilde{\sigma}^2_{\Delta x}(\Delta t) = \frac{1}{N-1} \sum_{i=1}^{N} (\Delta x_i(\Delta t) - \langle \Delta x(\Delta t) \rangle)^2 \ . \tag{2.44}$$

The estimator for the skewness defined in eq. (2.41) is

$$\gamma_1(\Delta t) = \frac{1}{N} \frac{\sum_{i=1}^{N} (\Delta x_i(\Delta t) - \langle \Delta x(\Delta t) \rangle)^3}{\sqrt{\sigma_{\Delta x}^2}^3} \ . \tag{2.45}$$

As stated above, one needs to calculate higher moments to describe a distribution more thoroughly. The next higher moment would then be the fourth moment, which when standardised, is called the kurtosis and quantifies the skewness or "tailedness" of the distribution

$$\beta_2(\Delta t) = \frac{1}{\sigma_{\Delta x}^4} \int_{-\infty}^{\infty} (\Delta x - \langle \Delta x \rangle)^4 P(\Delta x, \Delta t) \mathrm{d}\Delta x \ . \tag{2.46}$$

For a better comparison with Gaussian distributions, one can define the so-called excess kurtosis

$$\gamma_2(\Delta t) = \beta_2(\Delta t) - 3 \ , \tag{2.47}$$

which is a measure of deviation from a Gaussian form for which $\beta_2(\Delta t) = 3$. The corresponding estimator is calculated from

$$\gamma_2(\Delta t) = \frac{1}{N} \frac{\sum_{i=1}^{N} (\Delta x_i(\Delta t) - \langle \Delta x(\Delta t) \rangle)^4}{\sqrt{\sigma_{\Delta x}^2}^4} - 3 \ . \tag{2.48}$$

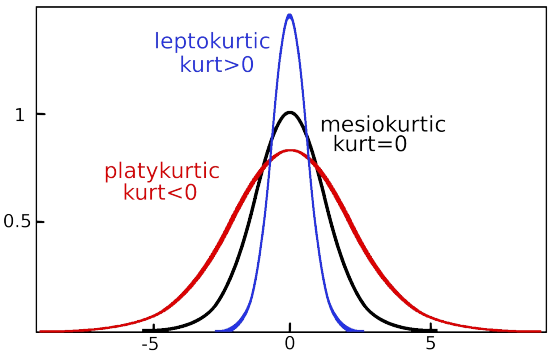

Figure 2.8: Kurtosis definitions for normal distributions.

Depending on its value relative to zero the respective function is categorised into three types. It is called platykurtic, if $\gamma_2(\Delta t) < 0$, which means, that the function is less flat-topped than a Gaussian distribution (fig. 2.8), leptokurtic, if $\gamma_2(\Delta t) > 0$, or mesokurtic, if the function follows a normal distribution, thus $\gamma_2(\Delta t) = 0$.
This characterisation can however be misleading since $\gamma_2(\Delta t)$ can not be used as a sole

measure for the overall shape of a distribution [1].
Moreover, $\beta_2(\Delta t)$ and $\gamma_2(\Delta t)$ are very sensitive to "outliers", since deviations have a dependence on the power of 4.
Another aspect to be careful with is the asymmetry of $\gamma_2(\Delta t)$ values around zero. While there is a lower bound defined by

$$\beta_2(\Delta t) = \gamma_1^2(\Delta t) + 1 \ , \tag{2.49}$$

there is no upper bound [1].

Related to the excess kurtosis is the non-Gaussian parameter, which is also a measure of how much a function deviates from a normal distribution, but it is calculated from fourth moments around zero and reads for d dimensions

$$\alpha_2(\Delta t) = \frac{d}{d+2}\frac{\langle \Delta \mathbf{r}^4 \rangle(\Delta t)}{\langle \Delta \mathbf{r}^2 \rangle^2(\Delta t)} - 1 \ . \tag{2.50}$$

Its definition derives from $\alpha_2(\Delta t) = 0$ for isotropic Brownian motion, where

$$\langle \Delta \mathbf{r}^4 \rangle(\Delta t) = \frac{d+2}{d}\langle \Delta \mathbf{r}^2 \rangle^2(\Delta t) \ . \tag{2.51}$$

For one dimension it can be estimated via

$$\alpha_2(\Delta t) = \frac{N\sum_{i=1}^{N}\Delta x_i^4}{3\Big(\sum_{i=1}^{N}\Delta x_i^2\Big)^2} - 1 \ . \tag{2.52}$$

It has similar behaviour to $\gamma_2(\Delta t)$ when it comes to the asymmetry of the distribution of its values around zero. The non-Gaussian parameter of the self part of the van Hove function serves as a measure for heterogeneity in the system at different times.

$\gamma_2(\Delta t)$ can be normalised for comparison with literature values

$$\alpha_2(\Delta t) = \frac{\gamma_2(\Delta t)}{3} \ . \tag{2.53}$$

This is then called the normalised excess kurtosis and is equal to $\alpha_2(\Delta t)$ for pure Brownian motion without drift.

In the pressence of an external force

$$F_D = \xi v_D \ , \tag{2.54}$$

where ξ is the friction coefficient, the behaviour of the system deviates from the diffusion equation eq. (2.31) and has to be corrected by a factor F_D. This accounts for the external

force, which causes a preferred direction for particle motion, also called drift motion or drift with v_D as the drift velocity of the particles.
Then the PDF reads

$$P(\Delta x, \Delta t) = \frac{1}{\sqrt{4\pi D \Delta t}} \exp\left\{ -\frac{(\Delta x - v_D \Delta t)^2}{4 D \Delta t} \right\} , \tag{2.55}$$

and the MSD is described by

$$\langle \Delta r^2(t) \rangle = 2dD\Delta t + v_D^2 t^2 \ . \tag{2.56}$$

When particles interact with each other, in contrast to the case of single-particle considerations above, the MSD becomes

$$\langle \Delta r^2(t) \rangle = 2dD_\alpha \Delta t^{\alpha_D} \ , \tag{2.57}$$

with D_α as a generalised diffusion coefficient.

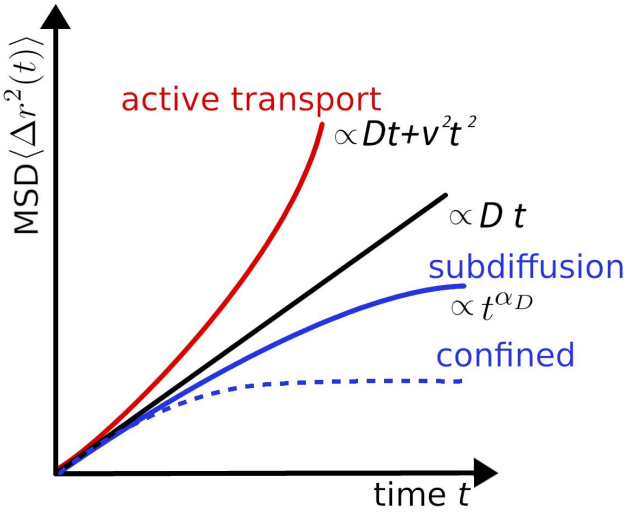

Figure 2.9: Schematic plot of MSD for different types of diffusion.

α_D is the so-called anomalous diffusion exponent and defines, whether the system is subdiffusive ($\alpha_D < 1$) or superdiffusive ($\alpha_D > 1$). For $\alpha_D = 1$ the case for pure Brownian motion is regained (see section 2.4.2).
For subdiffusion, the MSD curve flattens for larger times (see fig. 2.9). Examples of systems showing this behaviour, e. g. are crowded environments like cells.
In the superdiffusive case the particles are moving not solely from thermal fluctuations like for the Brownian case (red curve in fig. 2.9). This type of motion can be observed for active matter like bacteria or artificially created active particles.

2.4.4 Brownian Motion in a Harmonic Trap

In addition, there is the case of confined or partially confined (corralled) motion as seen e. g. in colloidal glasses or for tracer particles located in a confined area of a cell [78]. The area of the confinement L^2 can be estimated from the value which is asymptotically approached by the MSD [79]

$$\langle \Delta r^2(t) \rangle = \frac{L^2}{3}\Big(1 - \exp\Big(-\frac{t}{\tau}\Big)\Big) + 4\,D_M t \ , \tag{2.58}$$

where D_M is the long-term diffusion coefficient and $\tau = L^2/(12D_\mu)$ is the equilibrium time in the confinement with the microscopic diffusion coefficient D_μ.
A particle in an optical trap will also show a deviation from the diffusive regime. This will be discussed in the next section.

To describe the motion of a particle in a harmonic trap like in optical tweezers, we have to look at the motion differently than in the random walk model section 2.4. There, the movement was divided into discrete steps Δx for one dimension with vanishing mean $\langle \Delta x \rangle = 0$. On the other hand, the movement of a Brownian particle with mass m in a Newtonian viscous fluid with viscosity η can be described continuously by the classical Langevin equation [80]

$$m\frac{\mathrm{d}^2x(t)}{\mathrm{d}t^2} = -\xi(t)\frac{\mathrm{d}x(t)}{\mathrm{d}t} + F_R(t) + F_{ext}(t) \ , \tag{2.59}$$

with the drag coefficient from Stoke's law $\xi(t) = 6\pi R\eta(t)$ for the friction force $F_{fr}(t)$ and any external forces $F_{ext}(t)$. $F_R(t)$ denotes the random forces acting on the particle from collisions with molecules from the surrounding medium.

Eq. 2.59 can be rewritten by dividing by the mass m of the particle

$$\frac{\mathrm{d}v(t)}{\mathrm{d}t} + \frac{1}{\tau}v(t) = \frac{F_R(t)}{m} \ , \tag{2.60}$$

where $v(t) = \dfrac{\mathrm{d}x(t)}{\mathrm{d}t}$ is the particle velocity and $\tau = \frac{m}{6\pi R\eta(t)}$ is the dissipation time. The right side of the equation consists of a fluctuating part and can be treated like white noise, where the average over time vanishes $\langle F_R(t) \rangle = 0$. In the case, where the particle is trapped in a harmonic potential, $F_{ext}(t) = -k\,x(t)$ in eq. (2.60) is a linear restoring force

$$\frac{\mathrm{d}v(t)}{\mathrm{d}t} + \frac{1}{\tau}v(t) + \frac{k}{m}x(t) = \frac{F_R(t)}{m} \ , \tag{2.61}$$

where the undamped natural angular frequency can be written as $\omega_0 = \sqrt{\frac{k}{m}}$ with k as the spring constant or stiffness factor of the trap. It is a measure of how well a particle can be

kept in the centre of the trap and is therefore used for the calibration of optical tweezers. It can also be used to calculate the force F_{ext} acting on a trapped object.

The stiffness can be determined with the use of the equipartition theorem of energy

$$\frac{1}{2}k\langle x^2\rangle = \frac{1}{2}k_B T \ , \tag{2.62}$$

by equating the harmonic potential energy of the trap $\frac{1}{2}k\langle x^2\rangle$ and the thermal energy, where k_B is the Boltzmann constant and x the displacement from the particles equilibrium position in the trap [31]. The MSD $\langle x^2\rangle$ can then be calculated from the particle trajectories by analysing the Brownian motion of a particle, e. g. via video particle tracking. However, since $\langle x^2\rangle$ as the variance is a biased estimator, one has to be careful, when using this method. Drift or noisy position data will only increase the variance since it is always positive as a squared value. This in turn will decrease the stiffness estimate [31].

In this work, this method was used to determine the trap stiffness, see section 3.2.2. Other ways for determining k involve the drag force method or the analysis of either the optical potential or the power spectrum, which are mentioned but will be not discussed in more detail here, since they weren't applied in this work. Observing single particles is mostly useful for calibration. For more interesting phenomena and the formation of structures like crystals and quasicrystalline tilings, the interaction between many particles and multiple traps needs to be studied. The interaction between Brownian particles and light fields with 10-fold symmetry is the main concern of this work. In the next section 2.5 the basic physics for structure analysis and crystallography of quasicrystals will be introduced and continued in more detail in section 3.6.

2.5 Fourier Optics

For describing and explaining the optical trapping of a particle the ray optics regime is sufficient. However, diffraction effects can only be explained, if light is regarded as being made up of plane or spherical waves. These can be modelled mathematically in Fourier space, which will be presented in this section.

In general, any function in the time or space domain can also be expressed in the frequency domain by a Fourier transformation, named after the French mathematician and physicist Jean-Baptiste Joseph Fourier, who studied the Fourier series and developed the Fourier analysis. The transformation is defined by integrating a function $f(\nu_x, \nu_y)$,

$$\mathcal{F}(x,y) = \int_{-\infty}^{\infty}\int_{-\infty}^{\infty} f(\nu_x,\nu_y)\exp\left[-i2\pi(\nu_x x + \nu_y y)\right]\mathrm{d}\nu_x\mathrm{d}\nu_y \ . \tag{2.63}$$

With Euler's identity $e^{\pm ix} = sin(x) \pm i\cos(x)$ it can be seen, that any arbitrary function in the spatial domain can be approximated as the summation of several harmonic functions or wave functions by comparing the argument of the integral above (eq. (2.63)) to a time-dependent electromagnetic plane wave $\mathbf{E}(\mathbf{r},t)$ propagating through free space

$$\mathbf{E}(\mathbf{r},t) = \mathfrak{Re}[\mathbf{A_0}\exp\{i(\pm\mathbf{k}\cdot\mathbf{r} - \omega t)\}] \ , \tag{2.64}$$

where $\mathbf{A_0}$ is a complex amplitude. This is an equation for monochromatic waves, which is a solution to the Helmholtz equation

$$\nabla^2\mathbf{E}(\mathbf{r}) + k^2\mathbf{E}(\mathbf{r}) = 0\,, \quad k = \omega/c \ . \tag{2.65}$$

Comparing eq. (2.64) and eq. (2.63), $\mathbf{A_0}$ is analogous to $f(\nu_x, \nu_y)$ and ω to the spatial frequencies ν_x, ν_y.

2.5.1 Diffraction Phenomena

For creating a light field pattern, which is to be imaged in the sample plane, a DMD can be used. A DMD is an array of millions of micron-sized mirrors, which reflect the light according to their tilt angle, which can assume two states. It can be described as a reflective grating, hence the basics of diffraction phenomena will be introduced in this section.

When a planar wave interacts with an object, e. g. a narrow slit, it does not pass straight through it like it would be expected from ray optics. Instead, light only appears at certain

spots called diffraction orders, which are forming a diffraction pattern, that can be observed on a screen. It can be calculated from the so-called Huygens-Fresnel principle. It states, that every point on a wavefront is a source of spherical wavelets. A plane wave passing through a slit will then generate new wavelets, which are additionally interfering with each other causing the diffraction pattern to emerge.

Two distinctions have to be made when calculating the pattern or intensity distribution, dependent on the distance between the observation of the diffraction effects and the object, that is causing them.
First, consider the far-field regime, where

$$\frac{a^2}{L\lambda} << 1 \ . \tag{2.66}$$

This means the diffraction is studied at a large distance L to the object and the aperture has a small width a compared to its length and the wavelength λ of the light source. This is the so-called Fraunhofer regime, where these approximations can be applied in the calculation of the intensity distribution.
The near field case is the Fresnel regime, where the approximations above are no longer valid and the equations can only be solved numerically. All further calculations in this work can be done in the Fraunhofer regime since only the far-field diffraction is relevant and eq. (2.66) is satisfied. In general, it applies to imaging with lenses, diffraction at apertures or gratings and devices, which are based on the same principle as the DMD.

2.5.2 Single Slit Experiment

At first, the simplest case of diffraction at a single slit is explained, before considering the diffraction effects that appear, when using the DMD with a coherent light source.
The locations of the diffraction orders (maxima) and the minima where no light is allowed can be derived from interference considerations. If the phases of two waves are shifted by $\pi/2$, they interfere destructively, causing a dark spot on the screen. This is the case, when

$$2a \sin(\theta) = n\lambda \ , \tag{2.67}$$

where a is the width of the slit, θ is the diffraction angle and n is an integer, which denotes the order of the minimum. The whole intensity distribution on the screen (fig. 2.11) follows a sinc-function

$$I(\theta) = I_0 \ \mathrm{sinc}^2(\pi a \sin(\theta)/\lambda) \ , \tag{2.68}$$

where $\mathrm{sinc}(x) = \sin(x)/x$. This is the solution of the Fraunhofer diffraction equation for a slit of infinite length.

2.5.3 Diffraction Gratings

A diffraction grating can be seen as being made up of multiple identical slits. That's why eq. (2.67) also applies here, where a is now the line spacing equivalent to the distance between the slits (fig. 2.10).

The envelope of the intensity on the screen can be described again with the sinc^2 function eq. (2.68), which is the intensity distribution of a single slit. This means, that the intensity is not evenly distributed among the diffraction orders, but is defined by the height of the sinc^2 profile at the order location instead.

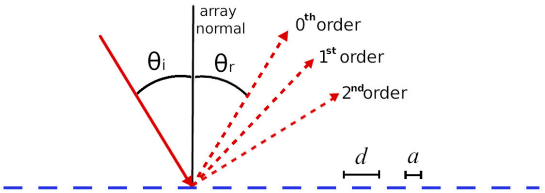

Figure 2.10: Illustration of a diffraction grating after [81]

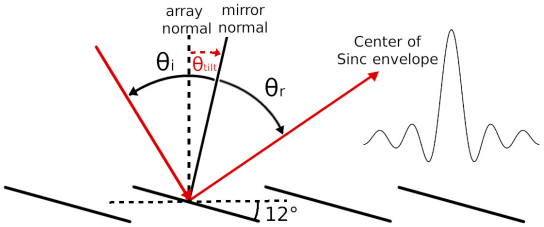

Figure 2.11: Illustration of a tilted diffraction grating after [81]

Moreover, the centre of the sinc^2 function is fixed to the zeroth order, which means, that it always receives the most intensity across all orders. However, this is not the case for a so-called blazed grating. Here, the groove faces have a tilt angle to the normal decoupling of the zeroth order from the sinc^2 envelope (fig. 2.11).

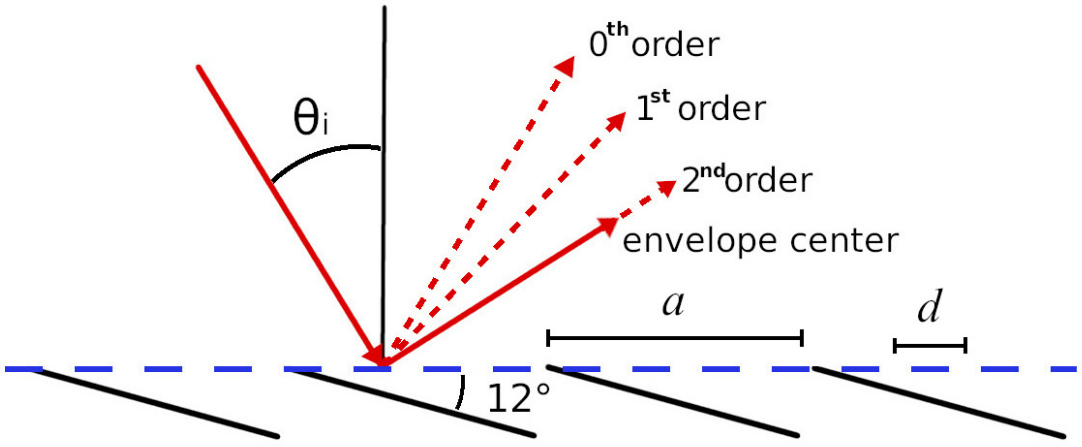

Figure 2.12: DMD illustration as a tilted reflective diffraction grating after [81].

For this case, the combination of the previous two cases of the multi-slit grating (fig. 2.10) and the tilted-blazed grating (fig. 2.11) is considered. A 2D reflective-blazed diffraction grating can be used to model the DMD. I. e. for two dimensions with widths a_x and a_y for each dimension the intensity envelope will be described by

$$I(x,y) = \mathrm{sinc}^2\left(\pi\frac{a_x}{\lambda}(x-x_i)\right)\,\mathrm{sinc}^2\left(\pi\frac{a_y}{\lambda}(y-y_i)\right)\,, \tag{2.69}$$

and the orders will be located at $(m\lambda/d_x, n\lambda/d_y)$ where m and n are integers and d_x and d_y the dimensions of the mirrors [81].

In the reflective diffraction grating, the grooves are replaced by the tilted micro-mirrors (fig. 2.12). The location of the sinc^2 peak is then dependent on the incident angle θ_i. For the alignment of the device, it is important to know the blaze angle θ_B. The blaze condition needs to be satisfied to ensure, that most of the intensity is directed into the order used for the light field in the sample plane. For this, consider the grating equation in one dimension

$$a\,[\sin(\theta_i) + sin(\theta_r)] = n\lambda\,. \tag{2.70}$$

The diffraction angle θ_r is dependent on the wavelength λ of the light source, the line spacing a as well as the incident angle θ_i. Both angles are relative to the array normal. If these angles coincide $\theta_i = \theta_r$, eq. (2.70) from above becomes

$$2a\,\sin(\theta_B) = n\lambda \tag{2.71}$$

This is the so-called Littrow configuration, from which the blaze angle θ_B can be calculated for one diffraction order.
The location of these orders is dependent on the grating pitch, the wavelength of the light source λ and its incident angle θ_i relative to the flat mirror state and can be calculated with the following equation

$$\sin(\theta) = \frac{m\lambda}{d} - \sin(\theta_i)\,, \tag{2.72}$$

where λ is the wavelength, d is the grating pitch and m is an integer [81]. The amount of intensity in each order and their positions relative to the main diffraction order depend on these parameters, which are all fixed by the DMD manufacturer and the light source except for the incident angle (eq. (2.72)). Hence for finding the blaze condition the angle of the beam incident on the DMD has to be varied. Then the non-zero orders move relative to the sinc^2-envelope centre and the incident angle is adjusted so that one of the orders coincides with the sinc^2-envelope centre.
More about the DMD properties and alignment of the setup will be presented in section 3.2.

2.5.4 Structure Analysis in Fourier Space

In scattering experiments like those conducted in crystallography, a sample is analysed in Fourier space, since its structure can be inferred from the scattered or diffracted intensity. In atomic crystals, x-rays are often used to probe the sample, while in soft matter systems electromagnetic waves in the visible spectrum can be used, due to the higher length scales of the structures. Colloidal crystals can even be studied under a bright-field microscope like in this work. The static structure factor is defined in Fourier space as

$$S(\mathbf{q}) = \frac{1}{N}\left\langle \sum_{j=1}^{N}\sum_{k=1}^{N} \exp\left[-i\mathbf{q}(\mathbf{r}_j - \mathbf{r}_k)\right] \right\rangle_t , \tag{2.73}$$

where $\mathbf{r}_j(t)$ and $\mathbf{r}_k(t)$ are the particle positions at time t and $\mathbf{q}$ is the scattering vector. It is defined as the difference between the incident and scattered wave vectors $\mathbf{q} = \mathbf{k_f} - \mathbf{k_i}$, where $\mathbf{k} = \frac{2\pi}{\lambda}$, so $\mathbf{q}$ has the dimension of a reciprocal length, e. g. m^{-1}. For the systems in equilibrium considered here, the ensemble average $\langle\cdot\rangle_t$ in eq. (2.73) is time-independent.

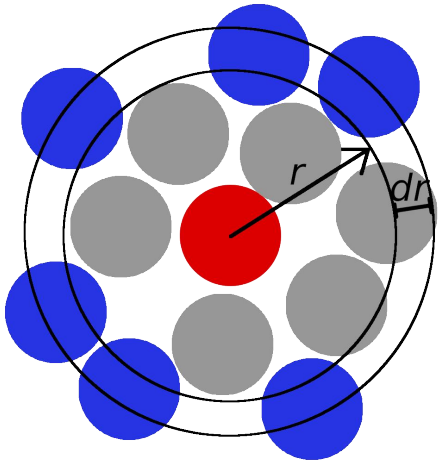

Figure 2.13: Illustrated Radial Distribution Function: The particles (blue) whose centres fall in a ring-area with width dr around a reference particle (red) are counted.Then the probability to find a particle in a ring dr for every distance r from the reference particle is depicted in the radial distribution function.

The static structure factor can also be written in terms of the radial distribution function $g(\mathbf{r})$

$$S(\mathbf{q}) = 1 + \rho \int_V \exp(-i\mathbf{q}\cdot\mathbf{r})[g(r) - 1]\,\mathrm{d}\mathbf{r} , \tag{2.74}$$

which describes the particle distribution from the distance of a reference particle at the origin (see fig. 2.13) while ρ is the average particle density. As the Fourier transform of $g(\mathbf{r})$, the structure factor gives the particle distribution in Fourier space. Hence $g(\mathbf{r})$ and $S(\mathbf{q})$ are carrying the same structural information.

For perfect crystals, the structure factor is defined as

$$S(\mathbf{q}) = \frac{1}{N}\left|\sum_{j=1}^{N} \exp(i\mathbf{q}\cdot\mathbf{r}_j)\right|^2 \propto \frac{I(\mathbf{q})}{N\,P(\mathbf{q})} \ , \tag{2.75}$$

where N is the number of particles, $\mathbf{r}_j$ is the position vector of the jth particle and $P(\mathbf{q})$ the form factor of the particles. The strength of the scattered intensity is proportional to the particle density at the corresponding position in real space [82]. Furthermore, constructive interference along a particular direction leads to a diffraction spot. For a given symmetry of the crystal's lattice the diffraction pattern will show these diffraction or Bragg peaks on defined spots reflecting the symmetry of the lattice. Therefore, the order of rotational symmetry is expressed in the number of diffraction peaks for one wave vector, so simply the number of points for one radius has to be counted. E. g. for a 2D hexagonal lattice a Fourier spectrum will show six evenly spaced peaks for wave vectors with a given length of 10 for a quasicrystal with 10-fold symmetry (fig. 2.14).

In crystallography, an analytic expression of the structure factors is the scattering amplitude, which is defined as the structure factor F_{hkl},

$$F_{hkl} = \sum_{j=1}^{N} f_j \exp\left[2\pi i(hx_j + ky_j + lz_j)\right] \ , \tag{2.76}$$

with the so-called Miller indices (hkl), defining a point in reciprocal lattice coordinates, and the atomic scattering or form factor f_j, which is a measure of scattering power of every atom (or particle) [83]. In general, for a full description of the structure factor, the information about the relative phases $\phi(hkl)$ between the scattered waves needs to be known too. This is also known as the "phase problem" in crystallography [82], where only the amplitude of diffraction spots can be measured, while the phase information is lost. The phases contain information about the exact positions of the particles or in the case of x-ray crystallography the electron density analogous to the atom positions. Since it is often the case, that the electron density

$$\rho(xyz) = \frac{1}{V}\sum_{hkl} |F_{hkl}| \exp\left[-2\pi i(hx + ky + lz - \phi(hkl))\right] \ , \tag{2.77}$$

needs to be determined, there exist several methods to retrieve the phases $\phi(hkl)$, e. g. the Patterson method [82].

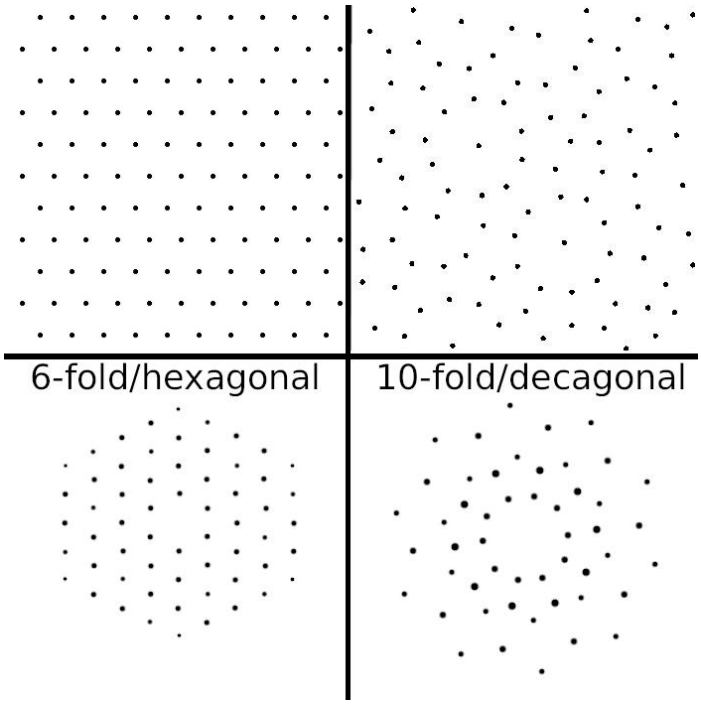

Figure 2.14: Schematic diffraction patterns (Fourier space) of the corresponding hexagonal (6-fold) and decagonal (10-fold) symmetries in real space.

On the other hand, a diffraction spot alone is already an indication of periodicity at the corresponding length scale. Therefore, it is often enough as in this case to only analyse the amplitude of the Bragg peaks in the diffraction pattern. These peaks appear every time the scattering vector is equal to a reciprocal lattice vector and can then be labelled with the indices (hkl), corresponding to the constructive interference of the wave vector scattered by the particles in the plane (hkl) in reciprocal space.
In contrast to the structure factor F_{hkl}, there are no planes defined for $S(\mathbf{q})$, since it is also valid for amorphous structures and the scattered intensity is given by the factor directly (eq. (2.73)). Therefore, $S(\mathbf{q}) \propto I(\mathbf{q})$ holds eq. (2.75), whereas for the F_{hkl} the scattered intensity is calculated by taking its squared modulus $|F_{hkl}|^2 = I(\mathbf{q}_{hkl})$ [83]. Since the diffraction pattern depends on the arrangement of particles, it is a powerful tool to analyse the structure of a periodic crystal or quasicrystals. However, for quasicrystalline symmetries, an indexing scheme has to be defined, which is different from 4-fold and 6-fold-indexing. There are already different proposals by several groups, of which the so-called Steurer indexing will be presented in section 3.6 in more detail.

3 Materials and Methods

This chapter deals with the materials and instruments used in both optical tweezers setups.

On one hand, a reflective liquid crystal-SLM (LC-SLM) consists of a liquid crystal on silicon, which modulates the phase of the light according to the alignment of the molecules in the liquid crystal. On the other hand, a DMD is used as shortly introduced in section 2.5.3.
The text mainly splits into four parts: The first deals with the procedure for preparing the samples. The second part presents the setups, their alignment and control software. The chapter continues with the properties of the quasicrystalline templates used in the experiments and methods of data analysis and finishes with the analysis methods for the particle dynamics.

3.1 Colloidal Samples

3.1.1 Particle Requirements

For trapping experiments, the object has to be dielectric with a higher refractive index than its surroundings. This is true for the polystyrene particles used in this work, with $n_p = 1.59$ at 590 nm [8]. They have a spherical shape, which makes them easier to trap, although it has also been achieved with other geometries [84].

The colloids in one batch of the stock solution will never be perfectly the same in shape and size. For this, the polydispersity is a measure of the heterogeneity of sizes of particles in a batch. The polydispersity index of particle sizes is defined as $PDI = (\sigma/\overline{d})/2$ with the variance of the distribution of particle sizes σ divided by the mean particle diameter $\overline{d}$ [85]. For the particles used in this work (Sigma Aldrich, 2.1 μm) it is 8 % as stated by the manufacturer of the beads. For this project, it is neglectable small.

In the experiments of this project, the particles should furthermore not interact in any different way than with the external light field. It is essential for this project, that the external control over the particles is assured. The particles chosen for this project showed no aggregation or unwanted interactions. The stock solution was kept in a fridge at 2-8 °C according to the manufacturer's recommendation and the final sample cell was stored next to the microscope of the setup at room temperature.

Depending on the experiment, the particle size has to be selected together with the magnification of the objective. E. g. for video particle tracking with bright-field microscopy, it is necessary, to get well visible particles in the Field of view (FOV).

In this case, the particle sizes were given by the manufacturer. In general, it can be determined with scattering experiments by exploiting the Stokes-Einstein relation (2.33). The particle radius is determined by measuring the diffusion coefficient in a solution with well-known viscosity behaviour, e. g. water at room temperature in Dynamic Light Scattering (DLS) or Differential Dynamic Microscopy (DDM) experiments. Although colloids as macromolecules are made up of subunits, they can be well approximated by a sphere. Then the radius describing them is the so-called hydrodynamic radius R_H.

When the particle size has been chosen, the particle concentration of the sample has to be considered next. In general, if low particle interaction is preferred, the concentration should be lower. This is favourable for studying particle dynamics like in MSD and diffusion measurements. To compensate for better statistics, the measurements have to be repeated by a reasonable amount.
Also for calibration and trap-stiffness experiments, the sample should be more diluted to avoid inter-particle interactions, since only the interaction between the particle and the light field is to be measured. For this, the particles should be more than a few diameters apart.

For crystallisation studies, on the other hand, a more concentrated sample is favourable, since inter-particle interactions become important and because of better statistics for structure analysis, e. g. when calculating the structure factor or pair-correlation function.
For the SLM experiments, the upper limit for the particle concentration is predefined. Since the SLM distributes the light intensity across the FOV when used with holograms, more particles mean less intensity per particle and hence less interaction strength depending on the desired pattern.

This is not the case when using the DMD to display the desired pattern directly. If it is illuminated homogeneously, the intensity per particle remains constant, but the unused light will be lost.
However, for the DMD experiments, the amount of particles per FOV is defined by the quasicrystalline templates. Hence a template-dependent concentration will be defined for every template. The particle fraction ϕ_p is the number of particles per FOV N_p, divided by the available positions in the template $N_{template}$

$$\phi_p = \frac{N_p}{N_{template}} \ . \tag{3.1}$$

A value of $\phi_p = 1$ means, that every template position can in principle be occupied by exactly every particle available in the FOV inside the range of uncertainty.

3.1.2 Sample Cells

As stated in the previous chapter, colloidal particles can be easily disturbed and affected by external forces. On one hand, this is a requirement for optical tweezers letting us manipulate particles with laser light. On the other hand, it also leads to sedimentation of the particles due to gravity. The process can be quantified by the gravitational length

$$l_g = \frac{k_B T}{\frac{4}{3}\pi R^3 \Delta\rho a_g} \ . \tag{3.2}$$

$\Delta\rho = \rho_p - \rho_m$ is the difference in density between the dispersed phase and dispersion medium and a_g is the gravitational acceleration on the averaged surface radius of the earth [1]. l_g is defined as the distance from the bottom or top of the sample cell to the point in space where the particle concentration drops to its 1/e-part. For water at $20°C$ and with $R = 1.05\,\mu m$ it is $l_{gH} \approx 1.60\,\mu m$. This means, that the particles rather tend to stay inside a 2D plane and not leave it by moving in the third dimension.
To create an equilibrated 2D layer of particles at the top of the sample cell heavy water (D_2O) can be added to the solvent. For D_2O the gravitational length is $l_{gD} \approx -1.42\,\mu m$, since the density $\rho_m = 1.107\,g/cm^3$ is slightly higher than for the particles at T = 293.15 K,

$\rho_p = 1.055\,g/cm^3$. l_{gD} is negative meaning that particles are pushed in the opposite direction than for H_2O.
In this work polystyrene particles (Sigma Aldrich, polydispersity, polystyrene latex beads) with a diameter of $2.1\,\mu m$ were dispersed in a mixture of filtered water (Purelab Flex, ELGA LabWater, electrical resistivity $18.2 \cdot 10^4\,\Omega m$) and D_2O (Deutero, Deuterium Oxide, D_2O, 99.9 %) with a ratio of about 4 : 5. Hence the density of the final solution was raised to $\rho_m = 1.085\,g/cm^3$ creating an effective 2D system.
Additionally, the setup is constructed in a way, that the scattering force of the laser pushes the particles to the top of the sample cell during a measurement if the light field is focused in the measurement plane.

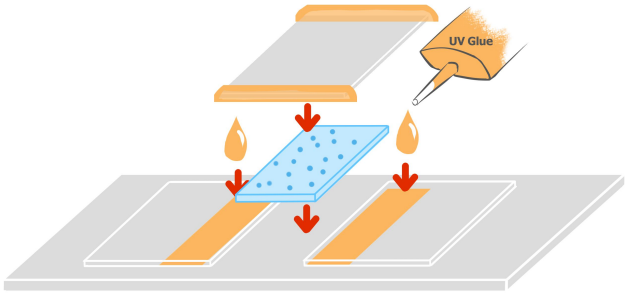

Figure 3.1: Illustration of sample cell construction.

(a) Side view. **(b)** Top view.

Figure 3.2: Schematic illustrations of the sample cell. UV glue is shown in orange.

These sample cells were built from microscope slides (VWR, 76 x 26 x 1 mm) and cover glasses (VWR, Micro Cover Glasses, Square, No.1) acting as spacers. They were sealed with UV glue (Norland optical adhesive, P/N6101, Fa. Norland) as depicted in (fig. 3.1). The two cover glasses used as spacers can either have thickness No. 1 or No. 0. Depending on how large the sample volume should be, a lower thickness should be chosen for less volume. However, the third cover glass on top of the cell needs to have a thickness no greater

than thickness No. 1 (0.13 to 0.17 mm), because of the objective's working distance. Most objectives need a thickness of 0.17 mm to work properly. Otherwise, the wrong coverslip thickness can lead to huge intensity losses due to optical aberrations and hence reduce the ability to gain information from the sample. Especially for objectives with high Numerical aperture (NA) as used in optical tweezers, the loss from having an incorrect thickness coverslip becomes more significant [86]. The best thickness one can use is a No. 1.5H (high performance), because the thickness range from 0.17 mm to 0.18 mm is even closer to the optimal 0.17 mm. For optical tweezers No. 1 thickness is sufficient.

The cells are glued with the help of a 3D-printed mould, where the glasses can be positioned in more or less the same way each time. The glue is cured for 3 minutes under a UV lamp (ELC-500 Light Exposure System, Serial no. 8600082, Electro-Lite Corporation). This is done at least three times in total: After glueing the spacers, the top glass and the final sealing after filling the sample. Furthermore, these sample cells can be reused for many measurements, since they are relatively stable and long-lasting. All glasses have been cleaned thoroughly with isopropanol before use.

In the next section, the DMD and the corresponding optical-tweezers setup will be introduced. The DMD properties and the alignment procedure will be presented and requirements for an optical tweezers setup with this device will be discussed.

3.2 The Digital Micromirror Device

A DMD is a device for manipulating incident light with a small chip consisting of an array of over 2 million separately movable micron-sized mirrors. The DMD used in this work (DLP® 6500 FYE, Texas Instruments) has a resolution of 1080 x 1920 pixels. This results in a size of about 1920 $7.56\,\mu m \approx 14.52\,mm$ in length and 1080 $7.56\,\mu m \approx 8.2\,mm$ in width of the micro-mirror array calculated from the mirror's pitch of $a = 7.56\,\mu m$. This array is mounted on a board with a thermal pad in between for heat dissipation (see fig. 3.3 for a schematic illustration). Additionally, a heat sink can be mounted for further cooling if it is needed. The aluminium mirrors are behind a window of Corning® EAGLE XG® alkaline earth boro-aluminosilicate glass with a transmittance of about 97% for 532 nm wavelength.

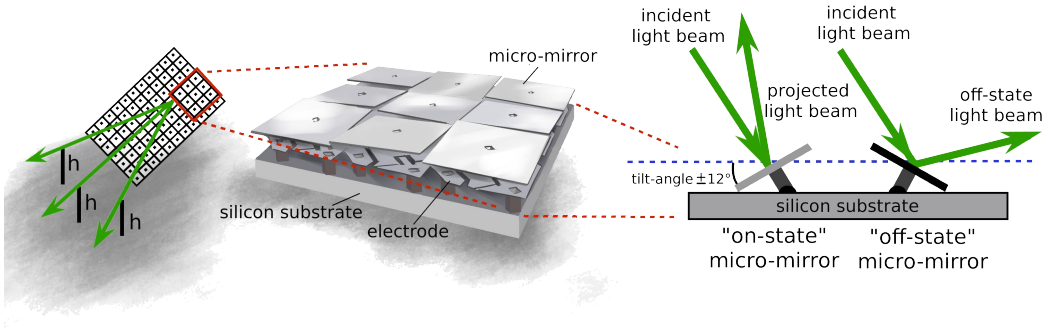

Figure 3.3: The DMD is mounted with a rotation of 45° around the axis perpendicular to the optical table, so the main orders reflected of the two states are in the same plane parallel to the table. The mirrors on a silicon substrate can adopt two states with a tilt of ±12°.

Each micro-mirror can be tilted by ± 12° along with the array's diagonal relative to the flat state with a response time of about $2.5\,\mu s$. For incoherent illumination like e. g. with LEDs, this results in the so-called "on-" and "off-beam" according to the state of the mirror tilt. While the beam one of those beams is used for the application, the other one is usually blocked with a beam dump. The beam from the "off-state" is inverted with respect to the other state and has a thin line around the active area like a frame. This is due to inactive rows of 14 pixels from the edges, which always stay in the "off-state" independent of the state of the remaining mirrors [87]. The DMD is capable of displaying patterns and images through a set of different operation modes. Depending on the connection established to the PC control, the DMD treats the input images as single patterns or like a video. To display a video an HDMI connection is needed, whereas a simple USB connection is sufficient for displaying a series of pictures. Here, the sequence of images can be predefined according to their order of display as well as the time span they will show up on the DMD. This

can be established in the so-called "pattern mode" or "pattern-on-the-fly mode". Although this would have a similar result as for a short video in "video mode" via HDMI, the latter one has a higher transfer rate (60 Hz) and reaction time and is therefore used in this work. Furthermore, for both of the pattern modes the built-in software of "Texas Instruments" to control the DMD has to be used. These modes are more useful for calibration and alignment during the construction of the setup, to check how and if the image is displayed in the sample plane as desired.
Additionally, some images are pre-stored on the DMD, e. g. checkerboards and vertical lines of different widths, which can be useful for alignment and checking the operation of the device.

For the experiments in this work, the images depicted on the DMD have a bit depth of 3. The reason why the bit depth needs to be lowered from 8 to 3 is due to the depiction of images on the DMD via HDMI connection. The DMD then needs to be used in the so-called "video mode", where a bit depth between 8 to 1 can be chosen, which translates into 256 to 2 possible pixel values. If however a bit depth larger than 3 is used, the contrast on the DMD is reduced and areas, which should be dark continuously are periodically turning from bright to dark. This is highly unfavourable for the experiments since there needs to be a contrast between regions contributing to decagonal symmetry and regions that don't. This effect is reduced when a bit depth of 3 or lower is chosen. Therefore, in all measurements, the DMD is used with 3-bit images, i. e. 8 possible grey values.
To ease the centering and positioning of the DMD in the FOV artefacts or flickering should be avoided by matching the exposure time of the DMD to that of the camera. Its value should be more or less the same as the camera's exposure time so that the image on the DMD is depicted long enough to be seen on the camera images. During the measurements the laser light is filtered out for the final images, but the particles are recorded when they are exposed to the light field.

3.2.1 Setup and Requirements for Optical Tweezers with a DMD

In this work, the DMD is used with a laser, which is a coherent light source and hence diffraction effects are appearing as already mentioned in section 2.5.3. Due to the periodically spaced structure of the over 2 million micro-mirrors, the use of a laser light source makes the DMD act like a 2D reflective tilted grating. This leads to the projection of multiple repetitions of the DMD image, with intensities and locations according to the laws of diffraction for a blazed grating. The location of these orders can be estimated with eq. (2.72). However, there are two effects, which contribute to the DMD's final diffraction pattern (fig. 3.4). Firstly the rectangular shape of mirrors acts like rectangular apertures leading to the *sinc*-distribution as in a tilted reflective diffraction grating (see section 2.5.3). The second part is coming from the comb function, which models the mirror array. The

intensity profile $I(x, y)$ at the mirror can be represented as a convolution of multiple 2D functions where x and y are coordinates in the array plane

$$I(x, y) = rect(A_m) * comb(a) * rect(A) * F(x, y) \ . \tag{3.3}$$

$rect(A_m)$ with mirror size A_m is a rectangular function representing each mirror, $comb(a)$ a repeating function for the array spacing structure, $rect(A)$ with the array size A for the array boundaries and $F(x, y)$ is the pattern written on the DMD [88]. For calculating the Fraunhofer diffraction pattern, the Fourier transform of this intensity profile has to be taken

$$I'(u, v) = \Big[\mathrm{sinc}(1/A_m) \cdot comb(1/a) \cdot \mathrm{sinc}(1/A) \cdot F'(x, y)\Big]^2 \ , \tag{3.4}$$

with the coordinates u and v in the image plane [88].
Hence the full description of the DMD diffraction effects is a more complex calculation. But for alignment, the details need not be considered. The description in one dimension provides enough accuracy for application.

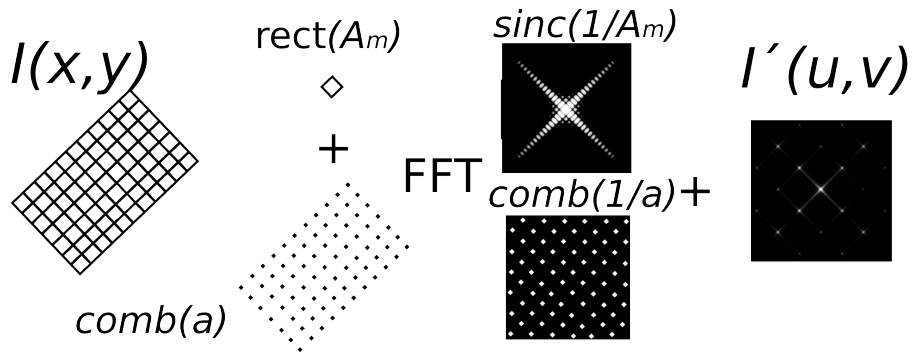

Figure 3.4: Formation of the DMD diffraction pattern [89].

Even if all mirrors are in the same state, the DMD is not acting as a flat mirror due to the tilt of the micro-mirror, since two consecutive pixels will have a phase difference due to different path lengths. Only when all micro-mirrors are in the parked state during standby mode, the DMD is flat and it acts similar to a conventional mirror, where the diffraction effects will vanish.
If one wants to use the device optimally, it has to be aligned in a way, that most of the reflected intensity is used (blaze condition, see eq. (2.71) in section 2.5.3). If not, a part of the intensity will be lost to higher diffraction orders. Therefore, when mounting the DMD, its design and the working principle of the mirrors need to be considered.
For this setup, the array has been rotated by 45° around the axis perpendicular to the optical table. This rotation results in the reflected main orders from the “on-” and “off-state” mirrors being both in the same plane above the optical table since the axis perpendicular to the table coincides with the tilt axis of the mirrors along the diagonal of the chip.

By varying the angle of the beam incident on the DMD, the blaze angle can be identified. In the blaze condition, the position of one maximum diffraction order is matched with the envelope centre of the overall intensity distribution (eq. (2.71) in section 2.5.3). This also means, that the next higher orders surrounding the main one, will all have the same intensity [90]. The blaze condition can then be checked experimentally, e. g. by measuring the intensity of these orders and comparing them to each other.

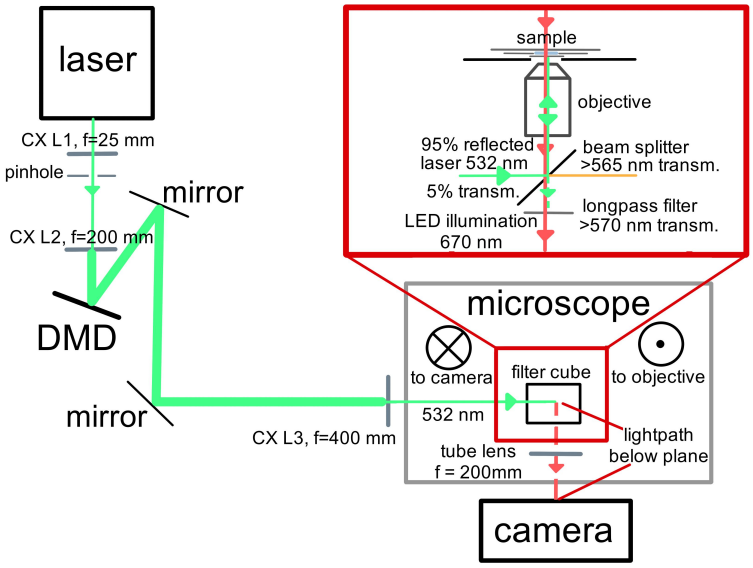

Figure 3.5: Illustration of the optical-tweezers-setup with the DMD used in this work as described in this chapter. For a real picture of the setup, see fig. A.1.
The 532 nm laser beam diameter is filtered and expanded by a telescopic lens system (L1, pinhole (20 μm), L2) to 14.8 mm for homogeneous illumination of the DMD. The beam is redireced by two mirrors and imaged with a lens and a microscope objective into the sample plane. A longpass filter removes the laser light ($< 570\,nm$) for the CCD-camera, to image the particles in the sample.

One requirement for setting up optical tweezers is a tightly focused laser beam with very high intensity. This can be achieved with a laser light source. However, until the laser beam reaches the sample, it interacts with several optical components like lenses and filters, which decrease its power output. For the application in this work, it is important, that most of the initial laser intensity arrives in the sample plane. The power at the sample can be measured as well as calculated from the specifications of the lenses and devices in the light path.

Starting at the laser head, in this setup a 532 nm DPSS laser (opus 532-3000, Laser Quantum Ltd.) with a maximal power output of 3 W is used. It follows a beam expander consisting of two plano-convex lenses (Edmund Optics) with focal lengths $f1 = 25\,mm$ and $f2 = 200\,mm$ to illuminate the DMD fig. 3.5. With the magnification factor of $200/25 = 8$ the initial beam diameter increases from $1.85\,mm \pm 0.20\,mm$ to $14.8\,mm$.

By placing a pinhole in the focal plane of the telescopic system, this beam expander acts also as a spatial filter. The beam diameter is increased and the side fringes representing the unwanted noise are removed from the input Gaussian beam. Only the central Gaussian spot is passing the filter thus creating a homogeneous illumination for the DMD with a collimated and parallel beam.
The incident angle on the DMD was chosen like in Sandmeyer et al. [90], where the DMD is facing the optical path to minimize image distortions while exploiting optimal intensity distribution from the diffraction. Due to the DMD's intrinsic structure diffraction effects can't be avoided when using a coherent light source like a laser as already discussed in section 2.5.3.
Two mirrors (Thorlabs) on kinematic mirror mounts (Thorlabs) are placed after the DMD to guide the beam from the laser to backport of the microscope.

For image formation a plano-convex lens (Edmund Optics) with a focal length of 400 mm before the microscope, together with the microscope objective (Nikon, Plan Apo VC, water immersion, 60x, NA=1.2) form an image in the sample plane. With this telescopic system consisting of the lens and objective, the initial DMD area is reduced by a factor of$\sim 400/4 = 100$. Using the back reflection of the condenser lens the beam can be aligned very accurately by controlling the mirror tilt on the optical table. Inside the microscope, a filter cube is located with a dichroic mirror (585 nm) and a longpass filter (570 nm). This composition transmits the 532 nm wavelength of the laser into the sample, while the dichroic mirror reflects light of this wavelength from the sample, so it does not reach the CCD camera (Mako U-130B, Allied Vision), which is mounted on one of the microscope-side-ports below the sample and below the plane of the light path coming from the DMD. The filter cube blocks the laser light for the camera but transmits the red illumination 670 nm coming from the LED lamp (Thorlabs) above the sample, so the particles in the sample plane can be imaged without being cross-faded by the high-intensity DMD pattern.
In the end, the images recorded are with a CCD camera and stored on a computer for further analysis, e. g. particle tracking (see section 3.7.1).

From the specifications of the devices and lenses the efficiency regarding the preservation of the laser power can be calculated, where the power loss can be divided into three main contributions: 1) Illumination loss is arising from the lenses the light has to interact with along its optical path to the sample. 2) It is dependent on the active components in the setup, meaning the characteristics of the laser and DMD and 3) the size and uniformity of the illumination on the DMD.

Concerning the first aspect, each lens is contributing about 92 % to the transmission, which is the value for the transmission for N-BK7 material at 532 nm wavelength [91]. These can be calculated to get a value of $(0.92)^6 \approx 0.61$ for the transmission of all lenses together.

Additionally, the illumination uniformity is ensured by the spatial filter. If the intensity is not homogeneously distributed in the sample plane, the particles are being exposed to a gradient in the potential, which can induce drift motion.
The pinhole diameter for the filter can be calculated with the known parameters of the

setup. These are the input beam diameter D_{in}, the wavelength of the laser beam λ and the focal length of the first lens f. With the following equation, the diffraction-limited spot size D_{out} can be calculated

$$D_{out} = 1.27\frac{\lambda f}{D_{in}} \ , \tag{3.5}$$

and used to estimate the pinhole diameter $D = 1.5\, D_{out}$ [92], where the factor of 1.5 ensures the passing of most of the intensity while eliminating as much spatial noise as possible. With the diameter of the laser $D_{in} \approx 1.85\, mm \pm 0.20\, mm$ before the spatial filter, $f = 25\, mm$ and $\lambda = 532\, nm$, $D_{out} \approx 9\, \mu m$. Here, a spatial filter with $20\, \mu m$ showed satisfying results. Choosing the pinhole size is always a compromise between a high-intensity beam and a noisy beam. Finally, power meter measurements have been conducted to measure the amount of laser intensity, which arrives at the sample plane behind the objective. The results are presented in the next section.

3.2.2 Calibration and Measurement of Trap Stiffness

As mentioned in section 3.2.1 the laser power was measured at the sample plane and compared to the output displayed on the laser head.

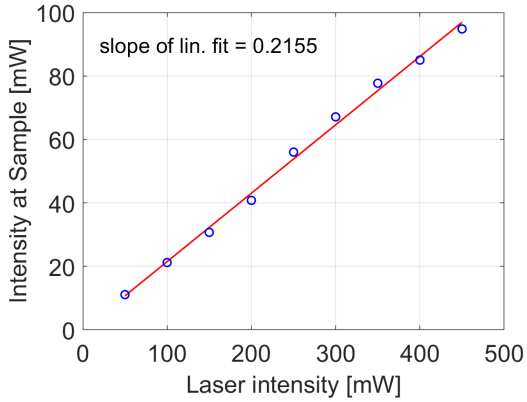

(a) Laser power in mW at sample compared to output at laser head. Measured with power meter placed after a 60x objective and all micromirrors of the DMD in on-state.

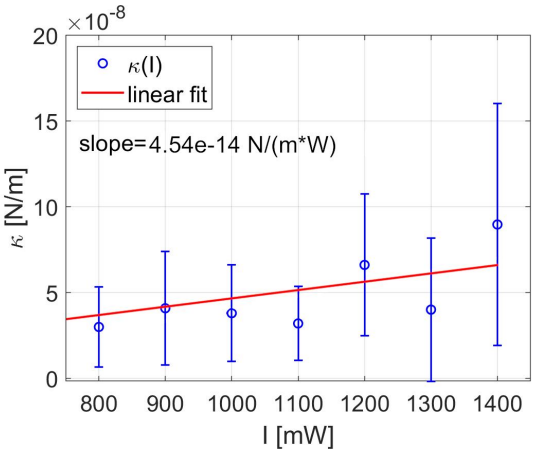

(b) Trap stiffness proportionality to laser power output: $\kappa(I) = 4.54 \cdot 10^{-11} \cdot I$

Figure 3.6: Trap-stiffness dependency on laser intensity in the DMD setup.

The slope of nine measurements from 50 mW to 450 mW in steps of 50 mW gives the intensity, which remains at the sample plane since it's the ratio between the intensity at the sample and the displayed output (fig. 3.6a). The measurement shows, that about 21.55 % of laser output gets to the sample. The rest is being absorbed or lost along with the setup's components (see section 3.2.1).

As a measure of trap strength or the ability to trap and hold a particle at the desired position, the trap stiffness κ is determined. For this, a particle is trapped in a Gaussian beam and its movement in the trap is recorded (see fig. 3.7a). From the distribution of its positions (fig. 3.7b) the stiffness κ can be calculated (fig. 3.6b) via

$$\kappa = \frac{k_B T}{\sigma^2} \ . \tag{3.6}$$

Since the trap can be modelled with a harmonic potential (eq. (2.62)), the particle positions in the trap will follow a normal distribution. Therefore, the width of a fitted Gaussian (fig. 3.7b, red line) to the data in x and y-direction (σ_x and σ_y) gives information about the trap's stiffness. For lower stiffness, the particle can travel further from the trap's centre, than for higher stiffness.

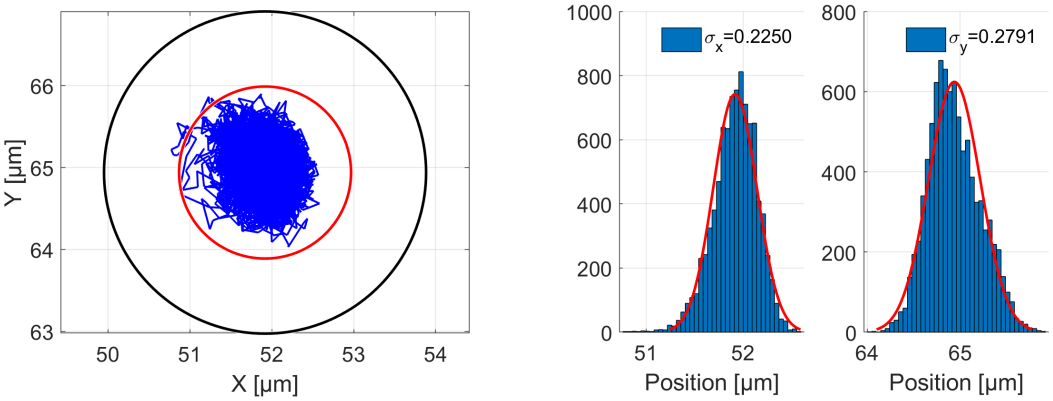

(a) Trajectory of a trapped particle. The particle size is shown with a red circle and the border of the Gaussian trap is marked in black.

(b) Histogram of displacements of a trapped particle whose trajectory is shown on the left. Gaussian fit is shown in red and σ values are in the legend.

Figure 3.7: Results of the calibration for the trap stiffness.

By varying the laser power the dependency between the stiffness and the intensity can be plotted (fig. 3.6b). For every intensity at least 10 values have been averaged from different trapped particles in the same sample. Images were recorded at 10 fps for 15 min at the given laser output power. Since the trap is assumed to be isotropic, values for x and y were not analysed separately. The resulting plot shows the expected linear dependency

$\kappa(I) = 4.54 \cdot 10^{-11} \cdot I$ between the trap stiffness κ and the laser power I, where $\kappa(0) = 0$ (fig. 3.6b).

In the next section, the setup with the SLM will be presented in the same manner as with the DMD beforehand.

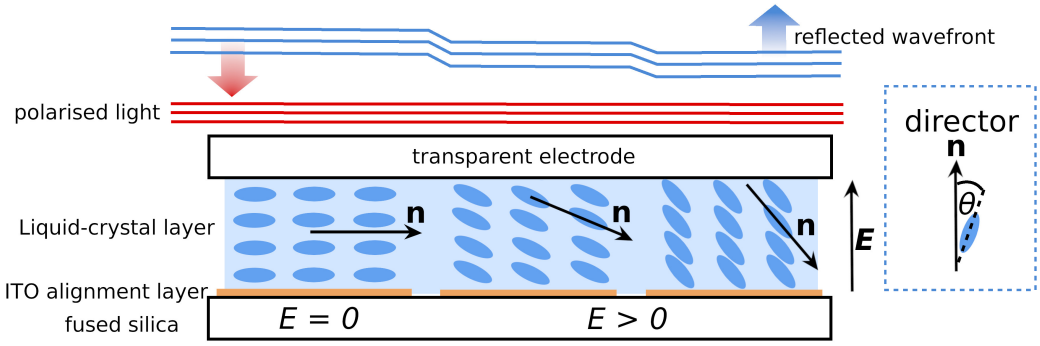

Figure 3.8: Schematic illustration of a spatial light modulator.

3.3 Liquid-Crystal Spatial Light Modulator

An SLM is a device, which as the name implies, spatially modulates the amplitude and phase of an electromagnetic wave. It is used to project images or to create multi-dimensional optical fields. With Holographic Optical Tweezers (HOT) it is possible to create multiple traps simultaneously and control them dynamically limited by the SLM's refresh rate [93].

There exist different kinds of SLMs based on different physical principles. E. g. an Acoustic-Optical Deflector (AOD) deflects light depending on sound waves, that change the refractive index of a crystal. A DMD, presented beforehand, is strictly speaking an SLM based on reflection, whereas a liquid crystal-based SLMs transmits the impinging light. Although both the SLM and DMD are technically light modulators, just the first one will be named SLM in this work for distinction.

LCs are made up of molecules acting as small dipoles, that can be aligned by applying an external electric field. The alignment affects the polarisation of an electromagnetic wave, e. g. of light, passing through. Three main phases can be defined: a smectic, nematic and (a cholesteric or chiral) phase as depicted in fig. 3.8. The degree of alignment in an LC can be quantified with a nematic order parameter $S = \frac{1}{2}\langle 3\cos^2(\theta) - 1\rangle$, where θ is the angle between a molecule and an axis in direction of the vector $\mathbf{n}$ defined like seen in fig. 3.8 [94]. $S = 1$ means all molecules are aligned while a system with $S = 0$ has no order. The smectic phase is the most ordered with $S = 1$, but is not strictly a solid-state, because the molecules can move. In the nematic phase, the molecules have still a preferred direction with $S \lesssim 1$.

In an SLM an array of twisted-nematic liquid-crystal (TNLC) cells is used. Each TNLC cell consists of dipole molecules sandwiched between two glass plates and transparent electrodes. If the electrodes are switched off, the molecules are aligned and twisted by 90° from one glass plate to the second one. A polarised electromagnetic (EM) wave passing through the cell will follow this twisted pathway, so the polarization of the outgoing wave will be turned by 90°.

If an electric field E is applied, several dipoles proportional to the field strength will align in its direction breaking the twisted structure. The polarisation of an entering EM wave will not be affected as much as in the off-state. The phase shift and therefore how much light passes through the TNLC cell can be controlled by the degree of alignment through the strength of the electric field. The higher the voltage applied, the more molecules will be aligned and the higher the polarization of the outgoing light.

In an SLM the TNLC cells are also coated with a reflective layer before the second electrode, so the light enters the cell, passes the LC, gets reflected and passes again through the cell. Each electrode corresponds to one pixel of the target image or pattern. To cover most of the SLM area and therefore each cell, a laser beam has to be expanded beforehand. The input to the SLM is called a hologram or kinoform and contains the phase information for the final image. In the SLM light is modulated in Fourier space and afterwards transformed by a Fourier lens into the image plane. To obtain the right phase information for the transformation, the Gerchberg-Saxton algorithm, named after their inventors, is applied for phase retrieval [95]. It starts with a random phase image while the similarity between the current and the desired image is iteratively checked. A more general algorithm is the error reduction algorithm, which is illustrated in fig. 3.9. The amplitude of the desired image is added to the random phase in the SLM plane. It is transformed to the image plane via an Fast Fourier Transformation (FFT) and the amplitude is removed leaving the phase information. The amplitude of the target is then added and via an inverse FFT transformed back to the SLM plane. It can be shown, that the algorithm converges to a hologram [96].

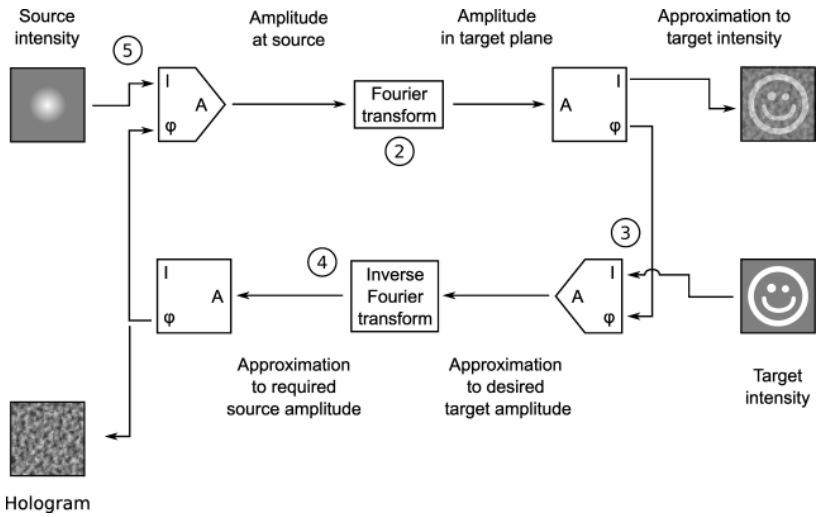

Figure 3.9: Schematic illustration of the Gerchberg-Saxton algorithm for phase retrieval [97].

The drawback of this method is the appearance of more orders apart from the dominant first order. Especially the zeroth order, seen as a bright spot in the middle of the target image, can be avoided but not fully eliminated. On one hand, it causes particles to get

trapped and often damages them due to the higher intensity than in higher orders. On the other hand, it can give rise to a radial repulsive force, driving the particles out of the FOV. This becomes more prominent if the setup is not well aligned.
Another problem can be the appearance of so-called "ghost" traps. These are traps, that are created due to the holographic nature of the technique, and appear on well-defined positions according to the desired pattern [98]. In general, it is possible to remove them, but it is an additional drawback for the use of an SLM.

3.3.1 Holographic Optical Tweezers with Spatial Light Modulator

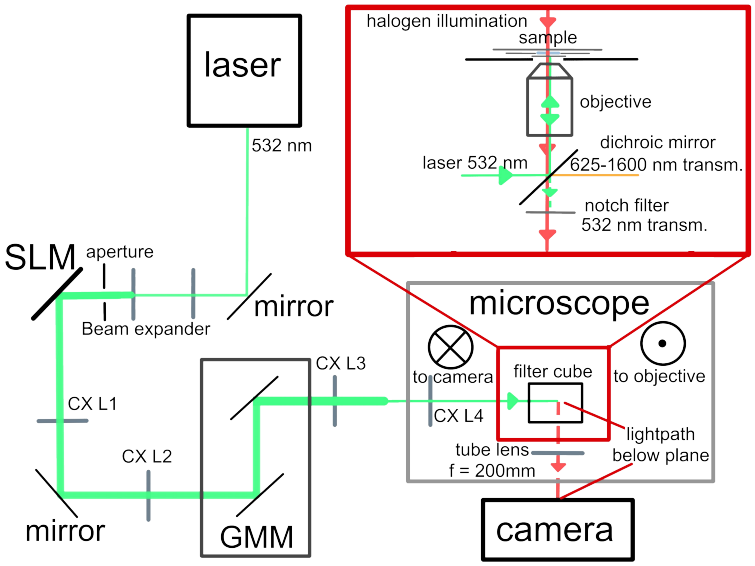

Figure 3.10: Schematic illustration of the Holographic-Optical-Tweezers-Setup with the SLM as described in this chapter. The 532 nm laser beam enters the beam expander to be increased to a diameter of 14 mm. After the SLM, the beam is guided to galvanometer-mounted mirrors (GMM) for beam control in the sample plane. The lenses L3 and L4 decrease the beam to 6.4 mm to overfill the back aperture of the objective which images the pattern in the sample plane. A CCD-camera records the images in the sample plane while the laser beam is filtered out by the notch filter.

In this section, the setup for the HOT will be presented. A DPSS laser (Ventus 532-1500, Laser Quantum Ltd.) with 532 nm wavelength and a maximal power output of 1.5 W was used. The laser current is controlled via a Microprocessor Controlled Power Supply Unit (mpc6000, Laser Quantum Ltd.). The laser beam is redirected by two mirrors and enlarged with a beam expander to fill the whole size of the SLM. The SLM used in this work is an LC-R 2500 by Holoeye. It has a resolution of 1024 x 768 pixels with a pixel pitch of

19 µm and an active area of 9.5 x 14.6 mm, while frame rates up to 72 Hz are possible. The light is modulated by the SLM according to the displayed hologram and reflected to a telescope consisting of two plano-convex lenses (Edmund Optics). Two galvanometer-mounted mirrors (GMM) (Quantum Scan 30, Nutfield Technology, Inc.) are used for beam steering in the sample plane more continuously and flexibly than with the SLM alone. A second telescope lens system before the microscope is used to overfill the back aperture of the objective. The back focal plane of the objective is a conjugate plane of the SLM, so the objective can perform a Fourier transform of the SLM pattern, to image the desired real-space pattern in the sample plane. Inside the inverted light microscope (Eclipse TE20000-U, Nikon) the modulated beam is deflected by a dichroic mirror (DM1, at 532 DCRB, Chroma Technology Corp.) to the sample and acts as a notch filter to reduce the laser intensity for the camera mounted on one of the side ports of the microscope. The laser beam is therefore invisible in the recorded images.

A 60 x magnifying objective (Plan Apo, Oil Immersion, NA=1.4, Nikon) is used to image the particles. The numerical aperture should have a value between 1.2 and 1.4 to create a stable optical trap because the intensity gradient has to be high enough to overcome the scattering force [31].
The depth of the trap is limited by spherical aberrations, which depend on the immersion medium and working distance.

Finally, the sample is pictured onto a CCD camera (Mako U-130B, Allied Vision) and sent to a computer for setup control via a LabVIEW VI (see section 3.4). The whole setup except for the computer and galvanometer is positioned on a pressure-stabilised optical table (Stabilizer, High-Performance Laminar Flow Isolator, I-2000 Series, Newport) inside a metallic box. All instruments are kept in a temperature-controlled room at 20°C.

This setup has to be checked regularly and realigned respectively to allow for a flawless operation and best measurement results, which will be explained in more detail in the next section 3.3.2.

For using the LC-SLM it has to be noted, that with higher particle concentration, the interaction strength decreases for each particle because the laser power has to be distributed throughout the FOV by the SLM. So each particle gets less intensity from the initial source if the particle amount in the FOV increases.

3.3.2 Alignment and Calibration

Drift Motion is an often encountered problem and usually unwanted in soft matter experiments. The causes for the particles to move in a preferred direction are numerous and very diverse. It could either be linked to the sample, e. g. a temperature gradient or a badly sealed sample cell, or originate from the setup, like an imbalance in the optical table due

to low pressure or a small tilt in the sample stage of the microscope, which can be checked with a water level and readjusted accordingly.

Furthermore, it can be checked if the drift is caused by the light path or its source by switching on the laser and observing if unidirectional motion only appears then or increases. Then the light path along the propagation at low laser power can be followed and checked for irregularities.
The source itself, which means the laser, can be examined with a laser beam profiler. It maps the spatial intensity distribution transverse to the beam propagation so it can be compared to a Gaussian profile. If the intensity is not distributed homogeneously around the centre, the particles will move in the preferred direction around the zeroth diffraction order.

Next, each part of the setup, e. g. the mirrors and lenses should be checked separately for misalignment or improper montage. For the alignment, the position of the lens after the beam expander can be adjusted in the plane perpendicular to the light path in x- or y-direction. This lets the peak of the Gaussian profile of the expanded beam shift into the centre of the FOV. If it is not centred, then the particles won't be distributed uniformly around the zeroth diffraction order and a normally unwanted unidirectional drift motion can be seen.

The alignment of the zeroth diffraction order in the centre of the FOV has to be done before each measurement (after turning on the galvanometer). The microscope illumination is turned off and the filter cube is taken out of the light path. Instead of the sample, a mirror is put onto the sample stage, so the laser beam gets reflected and the image plane of the SLM is pictured. The diffraction pattern is a calibration image where the zeroth order is seen. With the galvanometer, the voltage can be adjusted to rotate the mirrors and shift the zeroth order into the centre of the FOV for x- and y-direction separately.

3.4 Control of the Setups with Labview

Both setups (with DMD and SLM) are controlled with programs written in LabVIEW (National Instruments), where they are called "virtual instruments" (VI). Since the SLM and DMD technologies are based on different principles, every setup is controlled by a VI specially written for the device. In the next sections, both programs will be briefly presented.

For the spatial light modulator, a simple VI for a holographic-optical-tweezers setup was used as a template, while adding new subVIs to extend its functionality and tailor it for the specific needs of this project.

The first changes being made in the VI affected the feedback/adaptive part of the multiple tweezers. The aim was to not just move the particles with optical tweezers but to let them

self-assemble into different complex structures. For this, the effective interaction potential between the particles is changed by tailoring the form of the intensity pattern around each particle.

For trapping and moving one or many particles simultaneously, a multiple tweezer setup with a Gaussian intensity profile is used. If the point of highest intensity is in the centre of mass of the particle, then it can get caught in the trap and be moved by small steps from one place in the FOV to another. The size of the spot can be changed via the σ-value of the Gaussian, to allow the particle to move more freely in the trap. If the size of the Gaussian spot gets too large, the particle can eventually escape, because the laser beam will not be focused enough to hold it in its focal point.

For more complex trapping and particle-assembly into ordered structures via feedback programming, different shapes like single- or double-Gaussian rings, flat rings for flat-well potentials etc. have been created. E. g. for a hexagonal lattice, single-Gaussian rings were used with different radii for different lattice spacing. For square lattices, double-Gaussian rings with a radius ratio of $r_2/r_1 \approx 1.4$ can be used.

Additionally, automatically moving traps were programmed, e. g. to move single particles to the nearest cluster, for crystal nucleation experiments, or to move particles to a template of traps at fixed positions for the desired lattice structure. This can be done either one by one or as a whole cluster of up to 10 particles, which can be moved closer to each other to create larger areas with crystalline structures. Inside the cluster itself as well as in the merging process, the structures are left to form on their own via the feedback programming of the local potential. This means, that the particles retain the freedom of forming the desired structure by inter-particle-interaction like finding the destination on a preformed substrate. This procedure was inspired by the work of Martinsons et. al. [99]. To create low-defect colloidal quasicrystals they used a template in their simulations. The particles, which were separated from the template like in a reservoir, were sedimented one by one to the template with gravity as the only acting force. Upon reaching a distance in the length scale of the interaction potential, the gravitational force is no longer the main contributor. Instead, the particle movement is then guided by the template's potential. A screenshot of the VI for the SLM setup can be seen in fig. A.2).

For the DMD a new VI need to be programmed (VI screenshot see fig. A.2). Although some elements were kept the same, the base principle needed to be adapted for the DMD technique. The tracking algorithm stayed the same as well as the part for acquiring and storing images. Since the DMD does not use holograms, the calculation for the kinoform is replaced with a written algorithm in MATLAB (MathWorks Inc.). If it is desired to trap and move particles with multiple traps, then the particles are located and their coordinates re-scaled to match the coordinate system in the DMD size. A mosaic image is created by inserting the shape of the local intensity profile at the current coordinates of the particles found by the feedback algorithm.

For this work however static templates needed to be created. Double-rings in different sizes have been used as a local intensity profile, which was assigned to positions of decagonal Tuebingen tilings with six different distances. The details of the construction of the templates will be presented in section 3.5.

3.5 Light-Field Templates

In the past colloidal particles on quasicrystalline substrates have been studied, e. g. by Schmiedeberg [100] or Mikhael [101]. Instead of creating quasicrystalline light fields through the interference of laser beams, the patterns in this work are generated by overlapping double rings at positions of a decagonal tiling. This tiling is also known as the Tübingen (or "Tuebingen") tiling, and was discovered by Baake et al. in Tübingen, Germany [41], and is made up of pentagons, hexagons, nonagons, utiles and decagons (fig. 2.5). The double rings for the tiling, have a Gaussian intensity profile and should have a specific radius ratio for decagonal symmetry (fig. 3.12), which leads to the appearance of maxima of intensity at the overlaps of these rings.

To ensure that the maxima are located at positions for a decagonal symmetry, the ratio of two dominant lengths in the field potential should be around the golden mean [102], which is an irrational number defined by

$$\phi = \frac{\sqrt{5}+1}{2} \approx 1.618 \ . \tag{3.7}$$

This number appears in a regular pentagon, one of the tiles making up a decagonal quasicrystal. E. g. the ratio of the pentagon's side length L1 to its diagonal L2 is given by the golden mean or golden ratio (fig. 2.6a) [100]. Therefore, the golden ratio can additionally to eq. (3.7) be expressed only with numbers involving 5 as

$$\phi = 0.5 + (5^{0.5})\, 0.5 \approx 1.618 \ , \tag{3.8}$$

showing its relevance to the 5-fold/10-fold symmetries [103], since the golden mean can be found throughout decagonal tilings. E .g. the triangle formed from the two pentagonal lengths is called a golden triangle and the diagonals intersect each other with the proportion of the golden ratio. These relations can be explained by the Fibonacci series defined as $F_n = F_{n-1} + F_{n-2}, n \in \mathbb{Z}, F_0 = 0, F_1 = 1$. In other words, the equation means, that a successive number is constructed by summation of the current number with the previous one in the series. This is the same construction principle appearing in the diagonal and side lengths of a regular pentagon. It can be shown, that the ratio between successive Fibonacci numbers has the golden mean as its asymptotic limit

$$\lim_{n\to\infty} \frac{F_{n+1}}{F_n} = \phi \approx 1.618 \ . \tag{3.9}$$

Since the Fibonacci series has an aperiodic long-range order, it is also a good example of a quasicrystal in one dimension.

All in all, the golden mean is an essential number for decagonal symmetry and hence the radius ratio of the double rings for the templates is set to $r_2/r_1 = 1.6$. Although there are

two unknown variables, r_1 can be fixed by the distances between the centre positions of the rings, since then the ring around one position will cross the second position and vice versa. Therefore, r_2 is now a fixed parameter. Double rings of six sizes are shown in fig. 3.12. For six different template distances, the diameters of the first rings of the template in relation to the particle diameter are as follows: 0.91, 1.26, 1.57, 1.77, 2.11, 2.53.

Template No.	**positions /FOV**	**1st ring factor**	**ring width in µm**	**intensity factor of rings**	**trap size /d_p**
1	883	0.79	0.84	0.3	0.64
2	541	1.0	0.84	0.3	0.80
3	331	1.3	1.01	0.36	1.03
4	272	1.45	1.13	0.4	1.33
5	165	1.85	1.13	0.4	1.58
6	142	2.1	1.40	0.5	1.86

Table 3.1: Parameters of the six templates (fig. 3.11) used to create decagonal quasicrystals. The last column shows the average trap sizes in units of particle diameter ($d_p = 2.1\,\mu m$).

To make the rings overlap at positions recreating the symmetry of the rings' centres and creating minima of different depths in the potential, not only the width of the rings but also the intensity needs to be different for each ring. If both rings would have the same intensity, the adjustment of ring width is not enough to prevent the full FOV to be overloaded with high intensity. The particles wouldn't be able to differentiate between more and less favourable positions for a decagonal symmetry.
Therefore, the intensity of ring 2 is 20 % of the one of ring 1 and increases with the scaling of template positions, since for large template distances the area covered by the rings is slightly smaller and needs to be compensated. The same is true for the ring widths. The width is the same for both rings but increases with template distances. Since the rings' intensity is declining with a Gaussian, the width is calculated from the variance of the normal distribution. All parameters to create the templates are summed up in table 3.1. All templates used in this work are depicted in fig. 3.11.

Template No.	short main distance in µm	long main distance in µm
1	2.07	3.28
2	2.87	4.39
3	3.59	5.71
4	4.03	6.46
5	4.81	8.04
6	5.76	9.15

Table 3.2: Two main lengths of pentagonal tiles in all templates (see fig. 2.6a), i. e. the distances between the potential minima in (fig. 3.11a - fig. 3.11f).

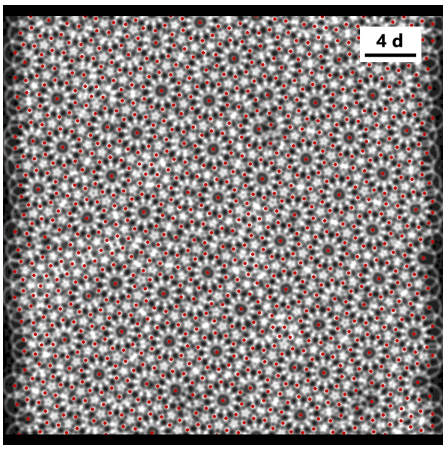

(a) Template 1: Ring radii: $r_1 = 0.91\,d, r_2 = 1.6\,r_1$

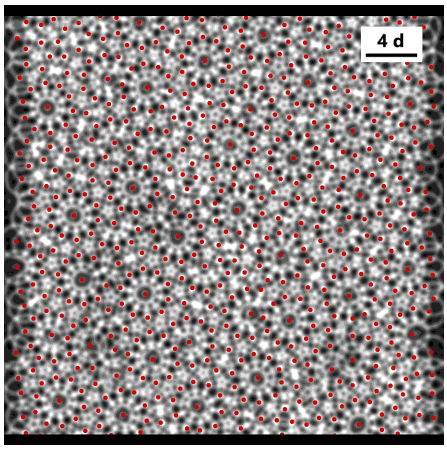

(b) Template 2: Ring radii: $r_1 = 1.26\,d, r_2 = 1.6\,r_1$

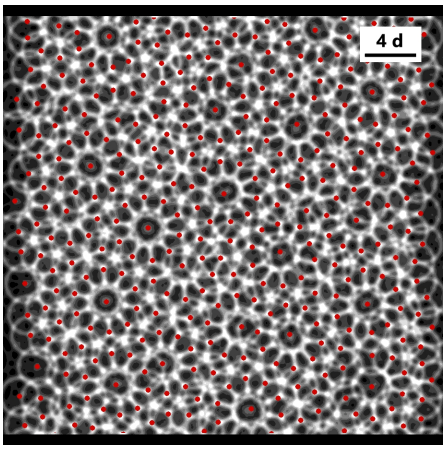

(c) Template 3: Ring radii: $r_1 = 1.57\,d, r_2 = 1.6\,r_1$

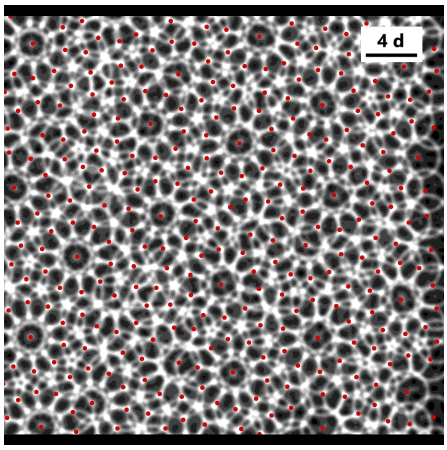

(d) Template 4: Ring radii: $r_1 = 1.77\,d, r_2 = 1.6\,r_1$

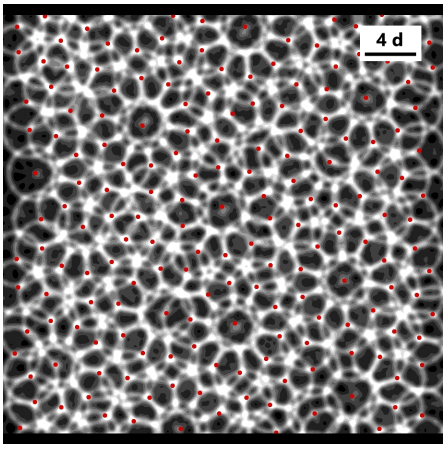

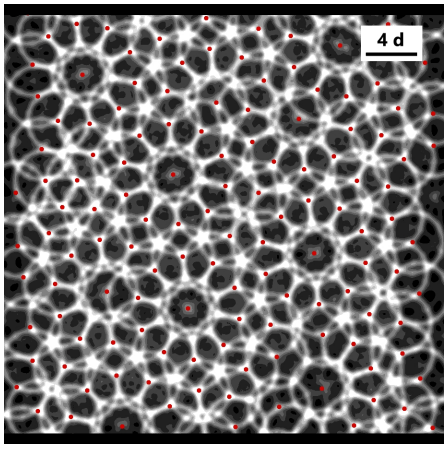

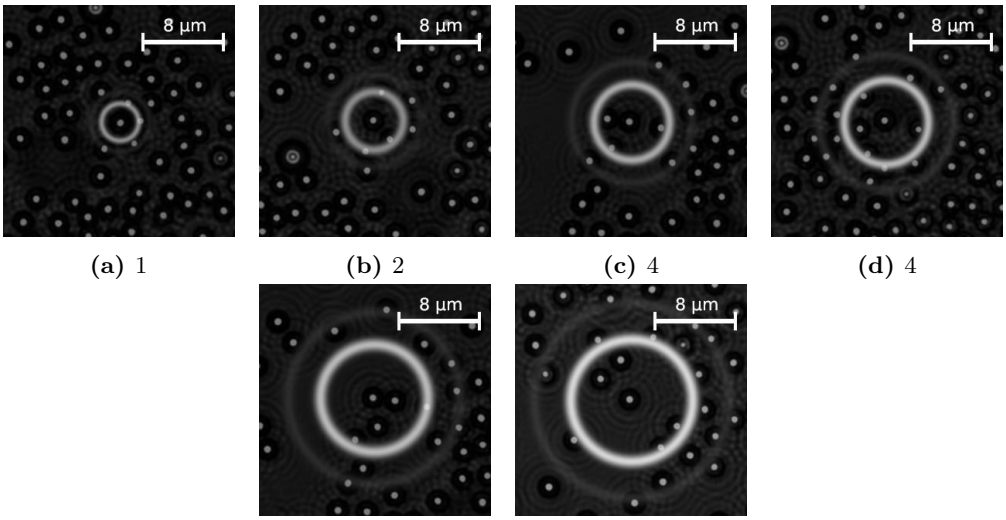

(a) 1 **(b)** 2 **(c)** 4 **(d)** 4

(e) 5 **(f)** 6

Figure 3.12: Ring sizes relative to particles used to create the templates (fig. 3.11a - fig. 3.11f).

3.6 Structure Factor and Crystallography of Decagonal Quasicrystals

In general, a diffraction pattern can be described by a Fourier transform [104]. Therefore, to study the diffraction pattern, the FFT of the particle arrangement, needs to be calculated. In this work, the magnitude of a 2D Fourier transform of recorded images for one measurement is calculated and averaged over one image series consisting of 16000 images. The 2D Fourier transform has been calculated with the built-in function `fft2` in MATLAB (MathWorks). The function calculates the Discrete Fourier Transform (DFT) Y of an m-by-n matrix X, which is defined for two-dimensions as

$$Y_{p+1,q+1} = \sum_{j=0}^{m-1} \sum_{k=0}^{n-1} \exp\left(-\frac{2\pi i}{m} jp\right) \exp\left(-\frac{2\pi i}{n} kq\right) X_{j+1,k+1} \ . \tag{3.10}$$

The 2D-matrix X can represent any data in 2D, like e. g. an image. In this case, the magnitude of the Fourier transform is the most relevant for representing the diffraction pattern of the sample, which is defined as

$$|Y_{p+1,q+1}| = \sqrt{\mathfrak{Re}(Y_{p+1,q+1})^2 + \mathfrak{Im}(Y_{p+1,q+1})^2} \tag{3.11}$$

By just looking at the magnitude of the Fourier transform of an image in this way, the diffraction patterns will be symmetric, i. e. the same Bagg peak will occur twice once for a negative frequency and once for the positive frequency with the same absolute value. The magnitude of $Y_{p+1,q+1}$ is independent of sign of the arguments, since we take the absolute value.
Additionally, $\cos(-x) = \cos(x)$ due to it's symmetry. $\sin(-x) \neq \sin(x)$ but since we take the absolute value for the magnitude $\sqrt{(\sin(-x))^2} = \sqrt{(-\sin(x))^2} = \sqrt{(\sin(x))^2}$. Therefore, the diffraction patterns will be symmetric too.

The diffracted intensity from the FFT $I(\mathbf{q}) \propto N\, S(\mathbf{q}) \cdot P(\mathbf{q})$ (eq. (2.75)) has still a component from the form factor $P(\mathbf{q})$ of the particles. To get the structure factor $S(\mathbf{q})$ the intensity $I(\mathbf{q})$ needs to be divided by the form factor $P(\mathbf{q})$ of the particles, which has been determined by calculating the DFT of single particles, i. e. a sample with a very low particle concentration (fig. 3.13a). Here, the particle interactions can be neglected. Furthermore, they are distributed randomly in the FOV. Hence for the structure factor $S(\mathbf{q}) \to 1$ holds and the form factor is, in this case, the main contributor to the diffraction intensity. This leads to

$$\frac{I'(\mathbf{q})}{P(\mathbf{q})} \propto N\, S(\mathbf{q}) \ , \tag{3.12}$$

where $I'(\mathbf{q}) = I(\mathbf{q}) - \langle I(\mathbf{q}) \rangle$ is the intensity of an image subtracted by its mean $\langle I(\mathbf{q}) \rangle$, i. e. the average value of all pixels in the image. This is done, to remove the strong signal around frequencies close to zero and thus lower the intensity of the values of interest. Performing the 2D-DFT leads to the characteristic pattern for the respective symmetry of the structure leading to a pattern as depicted in fig. 3.13b.

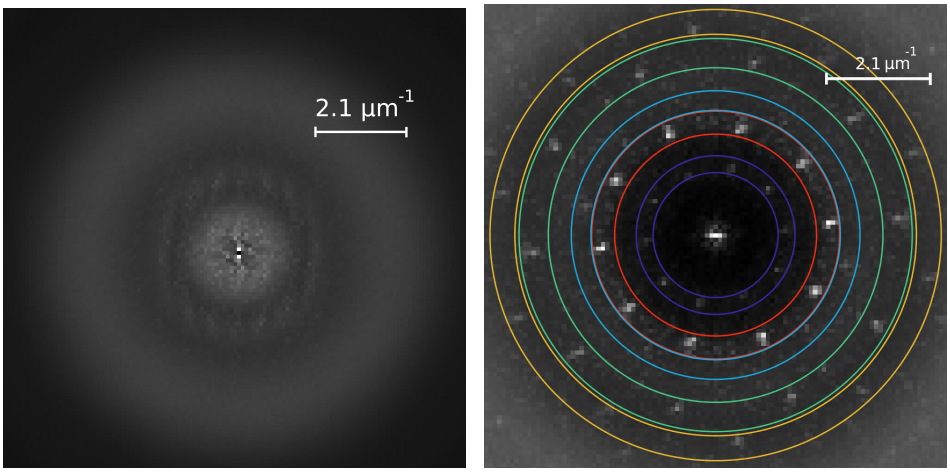

(a) Form factor of particles. There seems to be an anisotropy, which has not been removed by averaging over the particles due to low particle concentration and therefore not enough statistics.

(b) Evaluated ring areas (one area between rings of the same colour) plotted on the structure factor of particles in template 3 (fig. 3.11c) at 600 mW laser power.

Figure 3.13: Form factor of particles calculated from a dilute sample and evaluated ring areas.

To analyse the Bragg peaks in more detail, a ring-shaped area is taken at wave vectors, where the peaks are located. The values in this area are averaged radially for every angle and plotted as a 1D profile. Thus for every ring, an area will be analysed, which encompasses 10 peaks in total. The ring areas are shown on the structure factor of a measurement in fig. 3.13b. Each ring profile is fitted with a Gaussian sinusoidal function

$$f(\beta) = a_1 + a_2 \sin(2\beta + a_3) + \sum_{n}^{10} b_n \exp\left[-(\beta - b_{pos(n)})^2 / c_n\right] \ , \tag{3.13}$$

where n is the number of the peak, in this case, numbered from 1 to 10, β is the angle on the ring of the structure factor, a_1, a_2, a_3 are background-fit parameters and $b_{pos(n)}$ are parameters for the location of the peaks on the ring. Their values are ideally about 36° apart for 10-fold symmetry. Since the structure is not perfect, the angle between the peaks will deviate slightly from 36°. This deviation will be used, to calculate the location accuracy in section 4.1.4. The parameters to describe the fit are b_n, signifying the amplitudes or heights of the Gaussians and c_n, used to calculate the width of the Gaussians $\sigma = c_n/2$. The area

of the Gaussians is approximated from both of these parameters with $A_{BP} = \sqrt{(2\pi)}\,\sigma\,b_n$. The sinusoidal shape of the background stems from the definition of the intensity on a ring over a squared pixelated image. Since the ring doesn't hit all pixels evenly in their centre along the way, the pixel value is once over- and once underestimated. If the background is changing radially from the image centre then this process is periodical since it hits the centres of the pixels best in the vertical and horizontal position and less accurate in the diagonals of the image (fig. 3.14). To account for this, a sinusoidal function is fitted in addition to the Gaussians.
In summary, for every ring the Gaussian fit parameters for the height, width and area are averaged over all ten peaks. Meaning 3 parameters for one ring with up to $3x5 = 15$ values in total for every template, depending on the amount of evaluable rings.

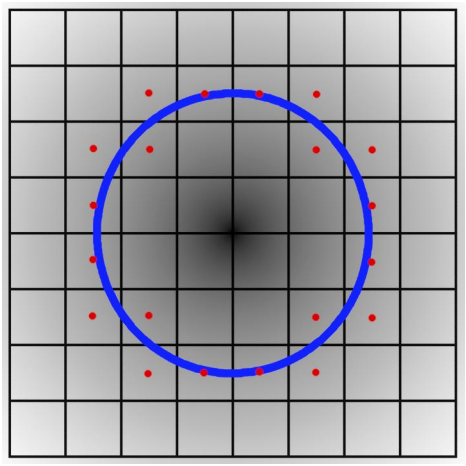

Figure 3.14: Graphical explanation for the sinusoidal background. Red dots are centres of the pixels, which contribute to the intensity profile of the blue ring. Pixels, which are closer to the ring, contribute more accurately.

While three basis vectors are enough for the description of 2- to 6-fold crystals, a new indexing scheme is needed for higher rotational symmetries such as for quasicrystals. Several different indexing schemes have been proposed. For example, Steurer et al. [105] or Yamamoto et al. [106] use five indices h_i, where four of the basis vectors $\mathbf{b}_i$ $(i = 1, 2, 3, 4)$ are co-planar and the fifth $\mathbf{b}_5$ is perpendicular to them. Since the quasicrystals studied here are two-dimensional, the fifth basis vector pointing out of the plane can be neglected. The four in-plane vectors are pointing from the centre to four vertices of a regular pentagon, which is a building block appearing in decagonal quasicrystals (fig. 3.16) [107]. The fifth vector in the pentagon $(-1, -1, -1, -1, 0)$ is not independent, since $-\mathbf{b}_1 - \mathbf{b}_2 - \mathbf{b}_3 - \mathbf{b}_4 = (-1, -1, -1, -1, 0)$ and is therefore not part of the basis. In the following the indexing for 2D-decagonal quasicrystals as elaborated by Walter Steurer and Torsten Haibach [108] will be presented. The five-dimensional diffraction vector $\mathbf{H}$ is defined as

$$\mathbf{H} = \sum_{i=1}^{5} h_i \mathbf{b}_i^* \tag{3.14}$$

with the integers h_i and $\mathbf{b}_i^* = b^*(\cos(2\pi i)/5, \sin(2\pi i)/5, 0)$ for $i = 1, 2, 3, 4$ and $\mathbf{b}_5 = b^*(0, 0, 1)$ [108]. Diffraction spots in the decagonal 2D-plane can be described by a set of 5 indices $(h_1\, h_2\, h_3\, h_4\, h_5)$, with $h_5 = 0$ for 2D-decagonal quasicrystals, which stands for one orientation of the lattice planes [53]. An example of this indexing is shown in fig. 3.16 on the Fourier space of a decagonal template fig. 3.11c used in this work.

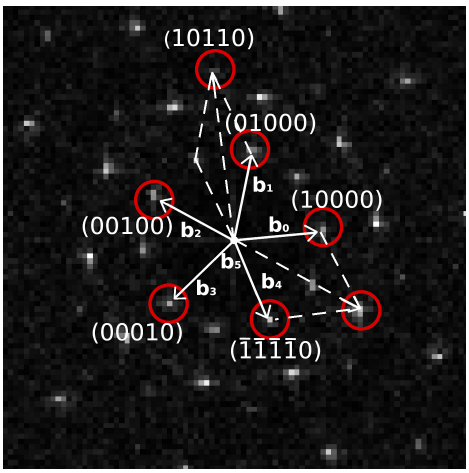

Figure 3.15: Indexing scheme for decagonal symmetry after Steurer et al. [105], shown on FFT of the decagonal structure of template 3 fig. 3.11c used in this work. The four in-plane basis vectors $\mathbf{b}_i$ are shown pointing to Bragg peaks marked with Steurer indices. $(\overline{1}1111\overline{0})$ is constructed by summation of the inverse basis vectors $\mathbf{b}_i$ and therefore not independent.

The vectors $\mathbf{b}_i$ in Cartesian physical space can be regarded as projections of the reciprocal basis vectors $\mathbf{d}_i^*$ $(n = 1, 2, 3, 4, 5)$ of a 5D periodic lattice given by

$$\mathbf{d}_i^* = b^* \left(\cos\left(\frac{2\pi i}{5}\right), \sin\left(\frac{2\pi i}{5}\right), 0, \cos\left(\frac{6\pi i}{5}\right), \sin\left(\frac{6\pi i}{5}\right) \right) \tag{3.15}$$

and $\mathbf{d}_5^* = b_5^*(0,0,1,0,0)$ for $i = 5$ (see fig. 3.16). The unit vectors in 5D direct space $\mathbf{d}_i$ can be calculated from the condition $\mathbf{d}_i \cdot \mathbf{d}_j^* = \delta_{ij}$ to

$$\mathbf{d}_i = \frac{2}{5b^*}\left(\cos\left(\frac{2\pi i}{5}\right) - 1, \sin\left(\frac{2\pi i}{5}\right), 0, \cos\left(\frac{6\pi i}{5}\right) - 1, \sin\left(\frac{6\pi i}{5}\right)\right) \tag{3.16}$$

and $\mathbf{d}_5 = \frac{1}{b^*}(0,0,1,0,0)$ for $i = 5$ (see fig. 3.16). The lattice constant $d_i = d = \frac{2}{\sqrt{5}b^*}$ of direct space is the side length of a pentagon (see L1 in fig. 2.6a).

There are also schemes with 6 indices as proposed by Ranganathan et al. [109] or Fitz Gerald et al. [110], where five base vectors are coplanar and the sixth, perpendicular to them along the axis of 10-fold symmetry. These schemes can be viewed in more detail from the corresponding references.

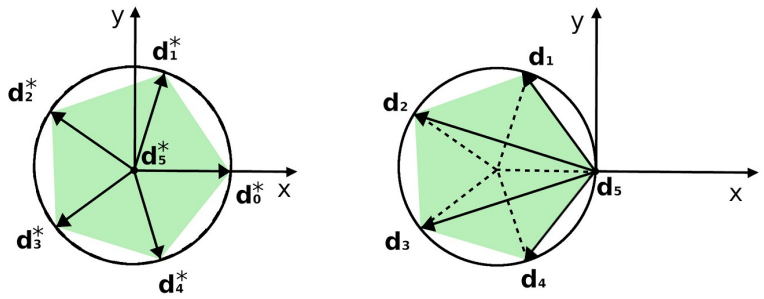

Figure 3.16: Basis vectors for decagonal symmetry in reciprocal (left) and direct space (right) after Steurer et al. [105]. The fifth independent vector is the one perpendicular to the plane $\mathbf{d}_5^*$ and not $\mathbf{d}_0^* = -\mathbf{d}_1^* - \mathbf{d}_2^* - \mathbf{d}_3^* - \mathbf{d}_4^*$.

3.7 Analysis of Particle Dynamics

In this section, the video particle tracking and the p-hop-algorithm are presented. With the help of these methods, the particle dynamics can be described and new insights are gained into the behaviour of particles in the light fields.

3.7.1 Particle Tracking

After the images have been recorded with the CCD camera and stored, the particle positions need to be determined. This can be done with subpixel accuracy by using a centroid-finding algorithm. There exist ready-to-use programs, e. g. by John C. Crocker and Eric R. Weeks for IDL [111] or Daniel Blair and Eric Dufresne for MATLAB (MathWorks Inc.) [112]. Algorithms for real-time tracking, limited only by the camera frame rate and computational speed or memory capacity are available too [31]. If a high-speed camera and high computational power are used, in principle the temporal resolution can be highly improved. Nevertheless, a limit exists, since the spatial resolution decreases with increasing frame rate due to noise [31].
Finally, the particle coordinates need to be calculated into micrometres. For this, the CCD-to-image-pixel-conversion factor is defined with a ruled micrometre, which is imaged with the same microscope objective and camera as used in the measurements. For a 60x-objective like used in the experiments, it is $\approx 0.086 \mu m/pixel$. Now the particle positions can be used for further analysis of the particle trajectories, MSD or the structure of the sample.

3.7.2 Particle Jumps with P-hop-Algorithm

The light field is acting as a template for the particles to form a structure expressing a 10-fold quasicrystalline symmetry. As long as the light field stays on, the particles are interacting with the potential in a different way, than they would in the absence of an external force field. Therefore, their motion will be distinct from a random walk and a free-diffusion model. This can be seen by studying their MSD and trajectories.
The minima in the potential will cause the particles to perform "jumps" or "hops". To identify these in the particle trajectories, the so-called p-hop-algorithm proposed by Candelier et al. [113], has been modified to evaluate the particle motion in the light fields. Based on Smessaert and Rottler [114], the following hop identifier function is defined

$$p_{hop}(t) = \sqrt{\left\langle (\mathbf{r}(t^A) - \overline{\mathbf{r}}(t^B))^2 \right\rangle_A \cdot \left\langle (\mathbf{r}(t^B) - \overline{\mathbf{r}}(t^A))^2 \right\rangle_B} < p_{th} \ , \tag{3.17}$$

where $t^A \in A$ and $t^B \in B$ and the average $\overline{\mathbf{r}}(t^B))$ is taken over $t^B \in B$ and for $\overline{\mathbf{r}}(t^A))$ accordingly. For this, the trajectory is first separated into two sections of equal size $A = [t - T, t - \frac{T}{2}]$ and $B = [t - \frac{T}{2}, t]$ around the time t. $p_{hop}(t)$ is calculated every $T = 400$ time steps translating to a time span of $T = 40\,s$. p_{hop} measures the averaged distance between the mean position in section A $\overline{\mathbf{r}}(t^A)$, and all trajectory points in section B $\mathbf{r}(t^B)$, and vice versa. Therefore, T can be interpreted as a measure of resolution of $p_{hop}(t)$. Since the function is large for rapid changes around $t - \frac{T}{2}$, it detects jump-events for values above a threshold $p_{hop} > p_{th}$. The ideal value for the threshold p_{th} would be, where a lower value would only detect noise as jumps and not minimal fluctuations inside of a cage or minimum of the light field potential. If p_{th} is chosen to low, then it detects jumps although there is no noticeable change in particle movement from the trajectory over time $\Delta\mathbf{r}(t)$. However, if the threshold is selected too high, then the algorithm can overlook smaller changes in the trajectory, e. g. "wiggling" inside of a trap, or movement along the more shallow minima created by the rings.

In my case, it would be more convenient to use a different input for the p-hop-function than the trajectory $\mathbf{r}(t)$. The change in the $\mathbf{r}$-vector would not register all of the jumps in the particle's trajectory, since only changes in the radial part $|\mathbf{r}(t)| = \sqrt{x^2 + y^2}$ would be registered. That is if the particle would move on a circular path, then p_{hop} would not change its value, despite particle jumps. Therefore, $\Delta r(t_i)$ is defined as the sum

$$\Delta r(t_i) = \sum_{j=1}^{i} \Delta s_j\,, \quad i = 1, ..., N-1\,, \tag{3.18}$$

of the distances Δs_i between two consecutive points (x_i, y_i) and (x_{i+1}, y_{i+1}) of the trajectory separated by $0.1\,s$ and

$$\Delta s_j = \sqrt{\Big(x(t_{j+1}) - x(t_j)\Big)^2 + \Big(y(t_{j+1}) - y(t_j)\Big)^2} \tag{3.19}$$

along the whole length of the trajectory $j = 1, .., N-1$. $\Delta r(t_i)$ is a monotonously increasing function. To facilitate the identification of the jumps, the monotonous function is substracted by a built-in MATLAB-function `detrend(x)`, which removes a best straight-fit line from the data in `x`.

When the threshold value has been chosen and the times t_{hop} where particle jumps are registered have been determined, the time between two consecutive jumps can be defined as

$$\tau_h^{(j)} = \left| t_{hop}^{(j+1)} - t_{hop}^{(j)} \right| \quad j = 1, ..., N-1\,. \tag{3.20}$$

For further analysis, the probability distribution functions of hop times can be considered. The results of this will be presented in section 4.2.1.

Additionally, to the PDF of hop times $P(\tau_h)$, the PDF of distances in between the jumps can be determined and compared to the distances between template-minima.

The length d_r between two jumps is calculated as

$$d_r = \sqrt{\Big(x(t_{k+1}) - x(t_k)\Big)^2 + \Big(y(t_{k+1}) - y(t_k)\Big)^2} \quad k = 1, ..., N-1 \ , \tag{3.21}$$

where N is the total number of jumps. The probability distribution of these jump distances $P(d_r)$ will be presented in section 4.2.2.

3.7.3 Packing Coefficient and Residence Time

To closer define the time a particle spends in a template position, e. g. trapped in a position of higher intensity, it needs to be defined first when a particle is entering a trap and when it is leaving it.
The time a particle spends in a template position defined as the residence time τ_r reads

$$\tau_r = |t_{in} - t_{out}| \ . \tag{3.22}$$

Although the exact values of t_{in} and t_{out} are hard to determine, they can be at least estimated with methods, that separate the trajectories into different regimes. One method uses the packing coefficient Pc_j as a measure for the compactness of a trajectory j. A formula from Renner et al. [115] has been slightly adapted for use in this work. It is defined for a time interval n as

$$Pc_{j,n} = \frac{1}{S_{j,n}^2} \sum_{i=j}^{j+n-1} \Big[(x_{i+1} - x_i)^2 + (y_{i+1} - y_i)^2\Big] \ , \tag{3.23}$$

where $S_{j,n}$ is the area of the convex hull of the segment of trajectory j between time points i and $i+n$ for the calculation of one convex hull. The term inside of the sum is equal to $(\Delta s_j)^2$ from eq. (3.19) used to calculate $\Delta r(t_i)$, which in turn is calculated for the phop-function as a measure for the length of the trajectory at time i. (x_i, y_i) are the particle coordinates at time point i and successive coordinates (x_{i+1}, y_{i+1}) are separated by $0.1\,s$
In mathematics, a set is convex if two of its points can be connected via a line, which is fully contained in the set itself. E. g. a shape like in fig. 3.17 (a) is not convex. The convex hull of a shape is defined as the smallest convex set that contains the shape. In this case, the shape is a set of coordinates of particles in the time interval n. Therefore, the area of the convex hull is a polygon containing every coordinate from i until $i + n$ either inside or at its border [116]. The convex hull has been calculated with the function `convexhull` in

Matlab (MathWorks).
To increase the impact this area S_j has on the packing coefficient, in the formula above (eq. (3.23)) its square is used. Hence the weight of this parameter is increased, since the packing coefficient $Pc_{j,n}$ is defined as a sum of areas measuring the space the particle explored in the time interval n, relative to the convex hull at the same time interval.

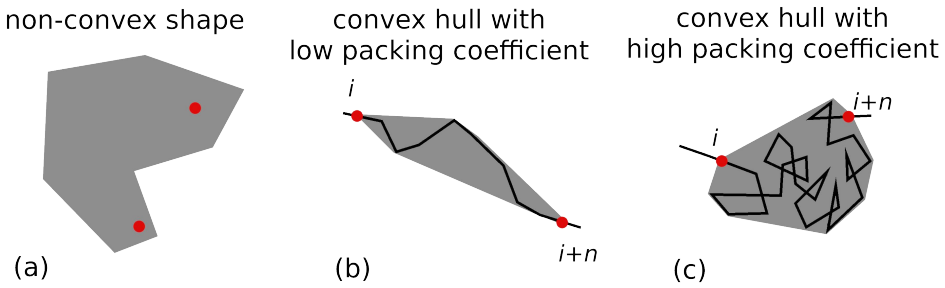

Figure 3.17: Convex hull illustrations of different sets.(a) A non-convex set. (b) Convex hull at small packing coefficient. (c) Convex hull at high packing coefficient.

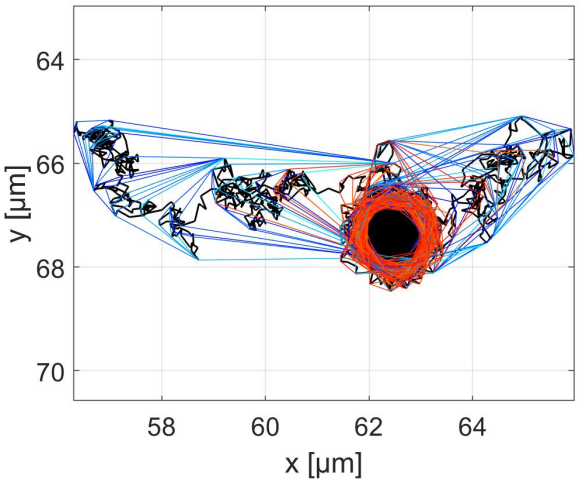

Figure 3.18: Exemplary particle trajectory (400 mW, $\phi_p = 1.2$, template 3.) with convex hulls coloured red for $Pc_{j,n} > Pc_{th} = 0.002\,\mu m^{-2}$ and blue for $Pc_{j,n} < Pc_{th}$. $Pc_{j,n}$ is calculated with eq. (3.23).

If the particle coordinates are spread further apart indicating high particle mobility (fig. 3.17 (b)), the convex hull will be larger in contrast to the area the particle explored during the time n. This results in a lower packing coefficient since the convex hull squared is in the denominator. If in the same time interval n the mobility is restricted, then the particle coordinates will be more concentrated in a smaller area. Therefore, $Pc_{j,n}$ will be larger since the convex hull is now more compact and contributes with a low value (fig. 3.17 (c)). Therefore, a high packing coefficient above a threshold value $Pc_{j,n} > Pc_{th}$ signifies a confined movement, e. g. like the motion in a harmonic trap (see fig. 3.18). Those parts of a trajectory which are less compact would then be indicative of a diffusive or superdiffusive regime. The packing coefficient is therefore a helpful tool to locate confined movement in single-particle trajectories.

Additionally, from the MSD plateau, the value which is asymptotically approached, the size of a confinement can be estimated with [115]

$$L^2 \simeq 6\langle \Delta r(t) \rangle_{plateau} \ , \tag{3.24}$$

where $\langle \Delta \mathbf{r}(t) \rangle_{plateau}$ is the MSD-plateau value and L is the typical size of the confinement or compartment, i. e. independent of the shape of the confinement it is the main length describing it. E. g. for a harmonic potential it can even be written exactly as $L^2 = 6k_BT/\kappa$.

With these tools, the behaviour of the particles in the light fields can be characterised. The residence times τ_r of trapped particles can be determined since t_{in} and t_{out} are now defined by the times, where the packing fraction exceeds the threshold Pc_{th}.

In section 4.2 the differences between the templates, different laser intensities and particle fractions will be analysed and discussed.

4 Experiments and Discussion

In this chapter, the experiments with the DMD will be presented first. Here, the particles' structure and dynamics were studied in the six light fields with decagonal symmetry. Beforehand, the decagonal templates will be analysed and used as reference values which can be compared to the measurements. After every section, the results will be discussed. In the end, the SLM measurements and findings will be presented and briefly discussed.

4.1 Structure of Colloids in Decagonal Light Fields

4.1.1 Structure Analysis of Templates

Template No.	**ring 1 in µm^{-1}**	**ring 2 in µm^{-1}**	**ring 3 in µm^{-1}**	**ring 4 in µm^{-1}**	**ring 5 in µm^{-1}**
1	2.32	3.76	4.40	6.08	6.12
2	1.76	2.80	3.28	4.56	5.36
3	1.36	2.16	2.56	3.60	4.20
4	1.20	2.00	2.32	3.28	3.80
5	0.96	1.52	1.84	2.48	3.04
6	0.80	1.36	1.52	2.16	2.56

Table 4.1: Wave vector lengths for the Bragg peaks / radii of the rings where peaks are located in structure factors of templates (fig. 4.1a - fig. 4.1f).

Since the template positions are point-like, there will be a neglectable contribution of a form factor. Therefore, $I(\mathbf{q}) \approx S(\mathbf{q})$ and the FFT of the point-template can be treated as its structure factor. The structure factors for all templates are shown in fig. 4.1.
In general, the Fourier transform is non-zero at specific points spanned by integer multiples of a finite set of basis vectors as described in section 3.6. The diffraction pattern of decagonal quasicrystals in particular is tiled with regular pentagons (fig. 4.2). When the side length of

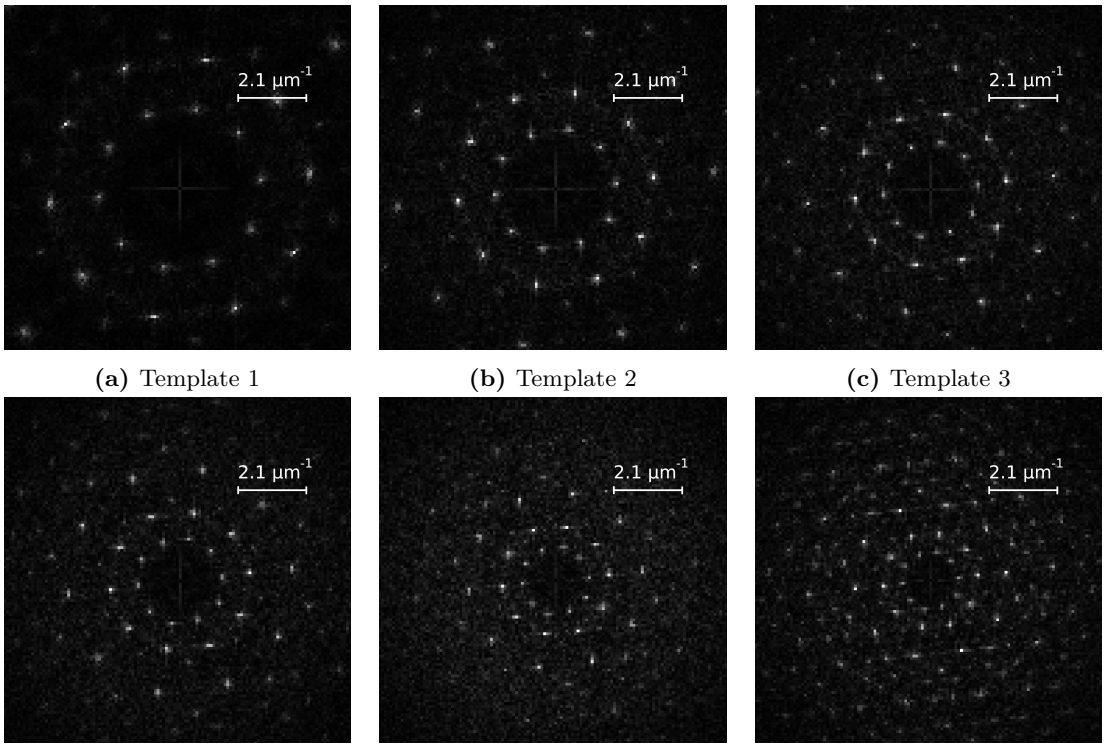

(a) Template 1 **(b)** Template 2 **(c)** Template 3

(d) Template 4 **(e)** Template 5 **(f)** Template 6

Figure 4.1: Structure factor of template points (fig. 3.11a - fig. 3.11f, red dots).

the smallest appearing pentagon is assigned a unit length of 1 (blue in fig. 4.2), then the first wave vector **a** will have a length of $a_{red} = a = \approx 1.6$, because it is the diagonal of the blue pentagon with side length 1. This can be continued with the next larger pentagon (red), whose side length a is the diagonal of the smaller pentagon (blue) and so on, continuing in the pattern of the Fibonacci series (eq. (3.9)). Therefore, the next larger diagonal $a_{green} = 1.618\,a \approx 2.6 = b$ with the length b of the second wave vector. With the definition of the Fibonacci series and eq. (3.9) the sum of the previous lengths is
$a_{blue} + a_{red} = 1 + 1.6 = 2.6 = b$.

The second and third wave vectors $\mathbf{b}_i$ and $\mathbf{c}_i$, can be constructed by adding two vectors $\mathbf{a}_i$ at different angles. The fourth $\mathbf{d}_i$ and fifth $\mathbf{e}_i$ are the resulting vectors of the addition of adjacent second wave vectors, while the angle between the vectors is two times smaller than for the fifth.
Therefore, the templates used in this work, follow the Lifshitz-Petrich model of minimising the free energy as introduced in section 2.3.1.

With larger template distances the rings are getting closer to the centre and hence the wave vectors are smaller (table 4.1). This is expected since $\mathbf{q} \propto l^{-1}$, where l is the length scale in real space. Furthermore, the first two wave vectors coincide with the larger (wave vector

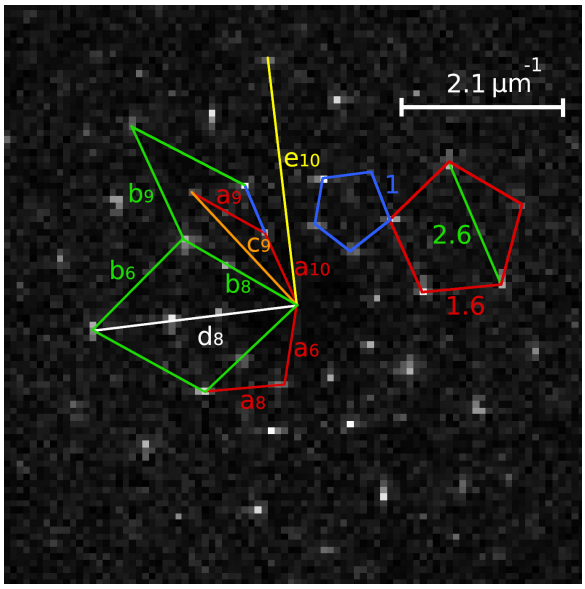

Figure 4.2: Relationship between the pentagon length scales in the diffraction pattern of template 5 fig. 3.11e.

for ring 1) and smaller main lengths (wave vector for ring 2) in the decagonal pattern (see fig. 2.5). This is true for every template and the ratio of the consecutive first wave vectors is the golden ratio as calculated above.

Additionally, it is to be noted, that although the distance ratio between templates 3 and 4 is only ≈ 0.10 and there seems to be no difference in the templates by eye (fig. 3.11c, fig. 3.11d), it is still possible to differentiate between their structure factors. The location of the peaks on one ring is around 2 pixels apart, thus the wave vectors differ around $0.16\,\mu m^{-1}$ which is ~ 0.07 times the particle diameter (see table 4.1).

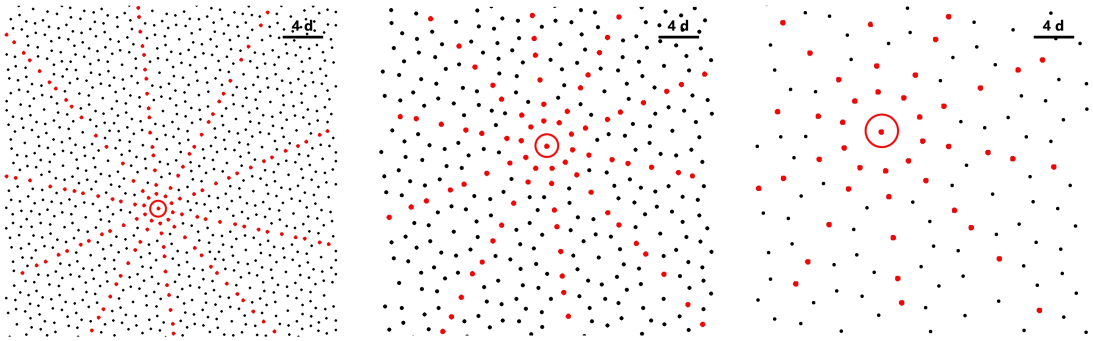

(a) 10-fold bond order directions for template 1.

(b) 10-fold bond order directions for template 3.

(c) 10-fold bond order directions for template 6.

Figure 4.3: 10-fold bond order directions marked in red for different templates.

When looking at the bond directions in the decagonal templates, which have been highlighted in fig. 4.3, the repetition of short and long distances (S,L) along the bond direction follows a specific pattern. It is again the pattern of the Fibonacci sequence (eq. (3.9)), $L\,S\,L\,L\,S\,L\,S\,L\,L\,S$ etc. Therefore, the repetition of this pattern at 10-fold bond order leads to the 10 Bragg peaks we see in the structure factor.

4.1.2 Bragg Peak Analysis of Templates

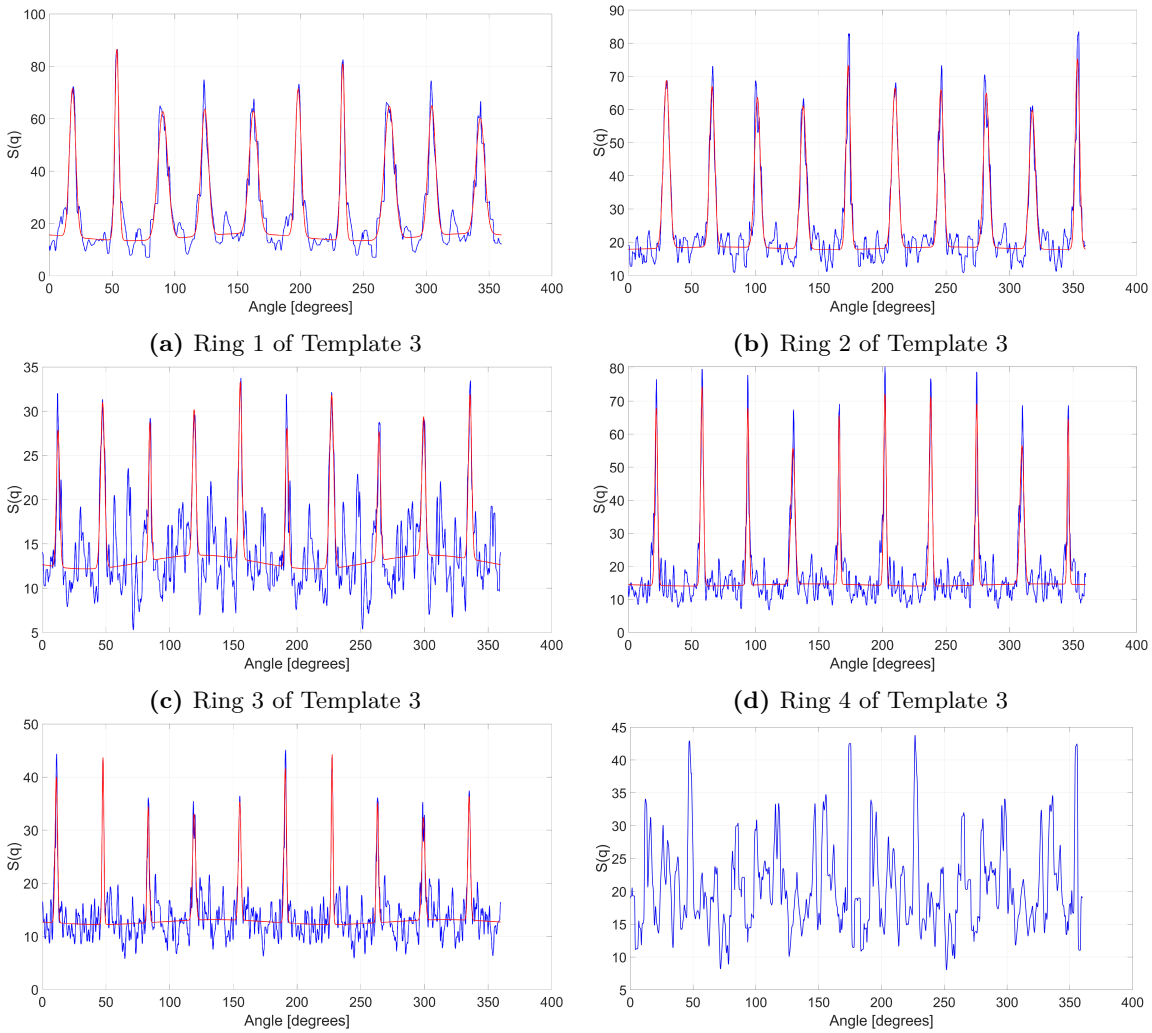

(a) Ring 1 of Template 3

(b) Ring 2 of Template 3

(c) Ring 3 of Template 3

(d) Ring 4 of Template 3

(e) Ring 5 of Template 3

(f) Ring 3 of Template 5

Figure 4.4: Ring profiles (blue) of $S(q)$ of template 3 (fig. 4.1c) and (f) ring 3 of template 5 (fig. 4.1e) with Gaussian fits to Bragg peaks (red).

The Bragg peaks are now being further analysed after the procedure described in section 3.6. A ring profile of the structure factors is taken at wave vectors, where the Bragg peaks are located. The resulting ring areas are depicted in fig. 3.13b and the calculated distances for every ring and template are listed in table 4.1. Up to 5 such rings can be determined depending on the template used. The ten peaks can be fitted with eq. (3.13) and their heights b_n and widths $\sigma = c_n/2$ will be analysed for each ring and template. In fig. 4.4a- fig. 4.4e the ring profile along with the fit is shown for all five rings. On each ring, the ten peaks are different in size and width, but each peak is appearing twice, meaning that there are only 5 distinct peaks. This is due to the symmetry of magnitude of the FFT as explained in section 3.6.

Overall it can be seen in the template profiles (fig. 4.4), that for rings 1 and 2 the noise is the lowest and the peaks are well defined, whereas for rings 3 and 5, the peaks are less well distinguished from the background noise. Especially for ring 3, it is difficult to fit the 10 peaks and for some templates, it is not possible at all (fig. 4.4f).

As seen in the ring profiles, the data for ring 3 is the least analysable. The peaks at this wave vector-only form for templates 2, 3, 4 and 6 have very low values (fig. 4.5a- fig. 4.5c). For templates 1 and 5, the peaks on the third ring weren't discernible from the noise and hence a fit couldn't be performed (fig. 4.4f). Additionally, for template 1, only rings 1 and 2 showed analysable peaks.

When looking closer at the fit parameters, the trend for the amplitude and the area is similar. Although both the height and width of the peaks contribute to the area with $A_{BP} = \sqrt{(2\pi)}\,\sigma\, b_n$, the width σ does not seem to have a large influence on the peak area. Here, we can see (fig. 4.5a, fig. 4.5c), that rings 2 and 4 have the most pronounced peaks, while the second has the highest.

Overall the height and therefore the area decreases to higher q. The width follows the same trend (fig. 4.5b), however, the width does not have a maximum for the second ring, but decreases continuously, except for templates 4 and 6. Another observation is the high values for template 6 relative to the other templates, especially for the peaks in ring 2.

Looking at the sigma values, which are treated as a measure of the width of the peaks, the values are decreasing with higher q values. Only for template 6 and also slightly for template 4, there is a deviation, where the fourth ring shows an increase of peak width compared to the third.

The analysis results of the template structure factors from above will serve as reference (desired) values for comparison with the particle arrangement measured in the light field, which will be presented and discussed in section 4.1.3 to section 4.1.4.

In the measurements with the DMD setup, different parameters are studied, which can influence the structure formation with the six templates.
The amplitude of the potential at the template positions (fig. 3.11) is controlled by the intensity of the laser. Hence it is assumed that a lower or higher intensity could have a

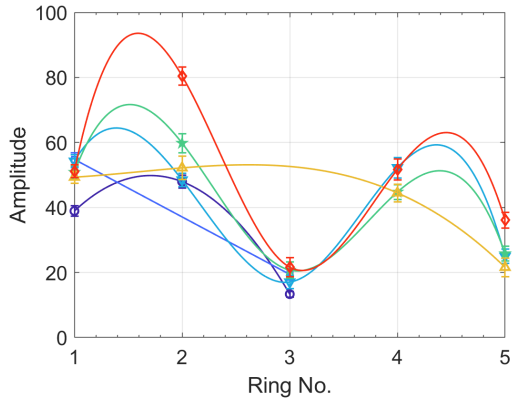

(a) Amplitudes of fitted Gaussians to template Bragg peaks.

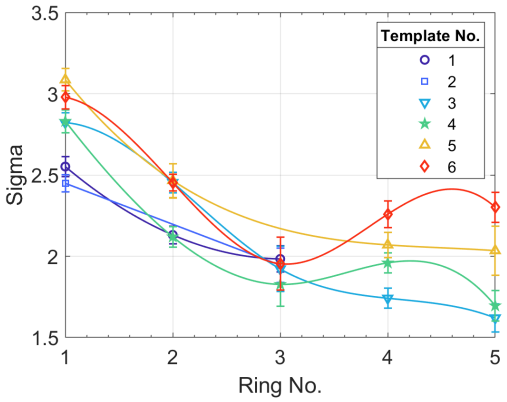

(b) Sigma values of fitted Gaussians to template Bragg peaks.

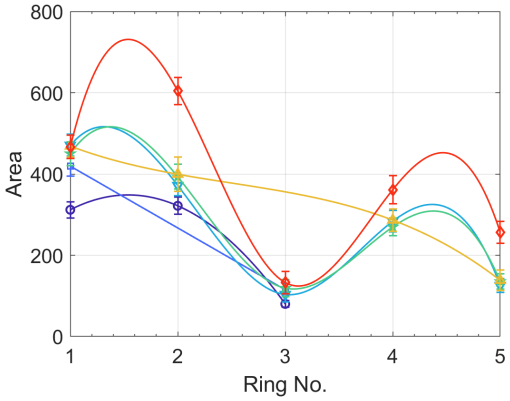

(c) Areas of fitted Gaussians to template Bragg peaks.

Figure 4.5: Height, width and area of fitted Gaussians to Bragg peaks of the template structure factor. The lines are a guide to the eye.

different effect on structural stability and the strength of 10-fold symmetry. The studied intensities are 125 mW, 250 mW, 500 mW and 600 mW.
Furthermore, the particle fraction ϕ_p, i. e. the number of particles per FOV and template positions is studied for one intensity and the six different templates. If all template positions would be occupied by particles, the maximal 2D-surface fraction can be calculated to ensure, that e. g. template 1 with the shortest distances is not too crowded, which means below the maximum packing fraction of 63 %. The surface fractions $\phi_{2D} = \pi r^2 N/A_{FOV}$, with particle number N and FOV size A_{FOV} for the templates are as follows: 62.9 %, 38.5 %, 23.6 %, 19.4 %, 11.7 %, 8.8 %. This means, that the number of particles to occupy every position of the first template is at the limit of 63 %. Further on this number decreases already for the next higher template to 38.5 %.

Each measurement for one set of parameters, i. e. one particle fraction and one intensity/laser-power-output, is averaged from 8 separate image sets with 2000 images each at 10 fps, while the particles' positions have been randomised after every 2000 images. This results in structure factors calculated by dividing the magnitude of an average FFT of 16000 images, by the form factor of the particles (fig. 3.13a).

4.1.3 Structure Factor with different Template Distances

To analyse the Bragg peaks, ring profiles of the structure factor images (fig. 4.6) are taken at wave vectors of the peaks (table 4.2). When comparing the ring locations of the measurements to the template references (table 4.1), there is a minimal shift to lower q values for some rings of the measurements (fig. 4.7). The deviation seems to be increasing for templates with smaller distances, while a value of zero signifies no deviation between template and measurement wave vectors.
Moreover, the deviation also increases for higher q, e. g. in ring 4. Some wave vectors couldn't be compared, e. g. ring 1 for template 6, since not all Bragg peaks were visible in the measurement (see fig. 4.6e, fig. 4.6f).

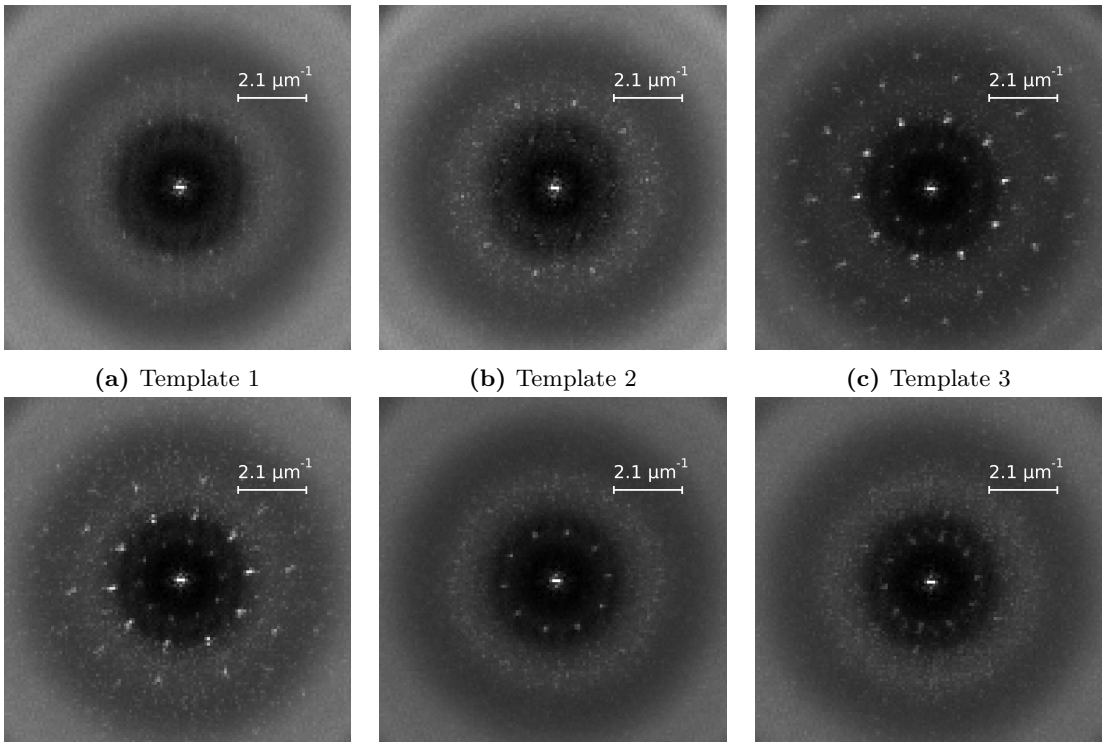

(a) Template 1 **(b)** Template 2 **(c)** Template 3

(d) Template 4 **(e)** Template 5 **(f)** Template 6

Figure 4.6: Structure factor of measurements with templates 1 to 6 at 600 mW and $\phi_p = 1.5 \pm 0.1$.

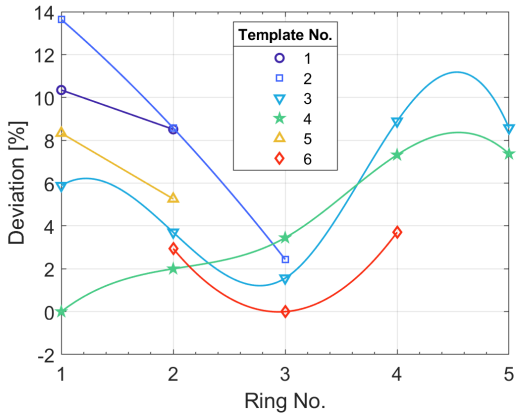

Figure 4.7: Inconsistency between Bragg peak locations of measurements (fig. 4.6) and templates (fig. 4.1).

Template No.	ring 1 in μm^{-1}	ring 2 in μm^{-1}	ring 3 in μm^{-1}	ring 4 in μm^{-1}	ring 5 in μm^{-1}
1	2.08	3.44	-	-	-
2	1.52	2.56	3.20	-	-
3	1.28	2.08	2.52	3.28	3.84
4	1.20	1.96	2.24	3.04	3.52
5	0.88	1.44	-	-	-
6	-	1.32	1.52	2.08	-

Table 4.2: Wave vector lengths for Bragg peaks/radii of the rings where peaks are located in structure factors of measurements (fig. 4.6a - fig. 4.6f).

However, if the peaks were distinguishable from the background, the ring profile can be fitted with eq. (3.13). Like in the ring profiles of the templates (fig. 4.4a-fig. 4.4e), the peaks are most pronounced for rings 1 and 2, where the noise is the lowest. For rings 3 to 5 the background noise increases and the peak height is overall lower.

In contrast to the reference template 3 profile of ring 5 (fig. 4.4e), the profile of the measurement is noisier (fig. 4.8e). Like for the templates, every fifth peak is repeating itself, because of the definition of the Fourier transform (eq. (3.11)) and its representation in the 2D plane.

Next, the profiles will be analysed in more detail, where the fit parameters b_n, σ and the area are plotted for each ring.

At first, the measurement with 600 mW and different particle fractions is analysed for every template and compared to the reference results. It is to be noted, that the number of particles per FOV was more or less similar for every template with 400 to 600 particles. However, the particle fraction is varying strongly since it is dependent on the number of template positions, which are decreasing from template 1 to 6 (see table 3.1). The fractions listed consecutively with the template number are as follows: 0.54, 0.85, 1.46, 1.82, 3.14, 4.06. Overall the dependence of height (amplitude), width (sigma) and area of the fitted peaks varies with the templates (fig. 4.9a-fig. 4.9c). Only for template 3 peaks for every ring could be fitted. Therefore, here we can see similar curves to the template reference (fig. 4.5). E.g. for the amplitude and area, a maximum is reached for the second ring and a minimum for the third, while it slightly rises again for the fourth ring only to decrease to the fifth ring.

Template 2 and 5 only could be evaluated for the smaller wave vectors until ring 2. In fig. 4.8e noisy data for the fourth ring in the structure factor template 5 in comparison to ring 3 of template 3 (fig. 4.8c) is shown. The remaining templates also do not show more than 3 data points, which makes a comparison to the template reference more difficult. The data points however show accordance.

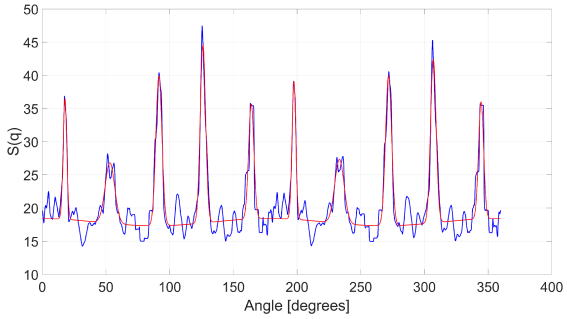

(a) Ring 1 of Template 3

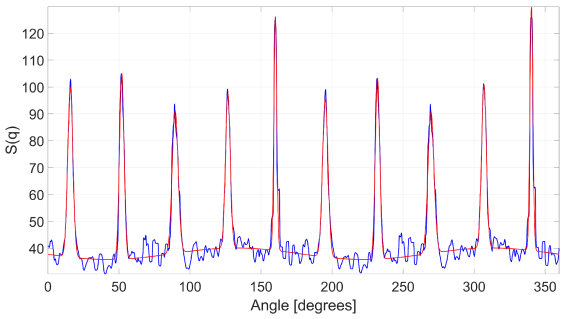

(b) Ring 2 of Template 3

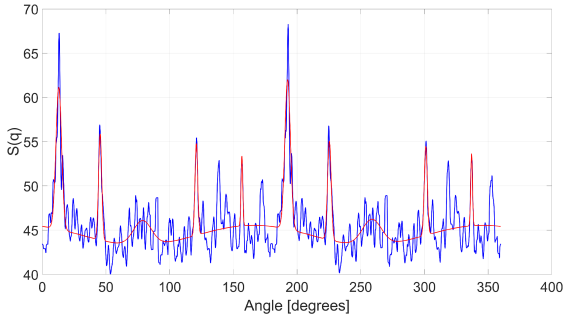

(c) Ring 3 of Template 3

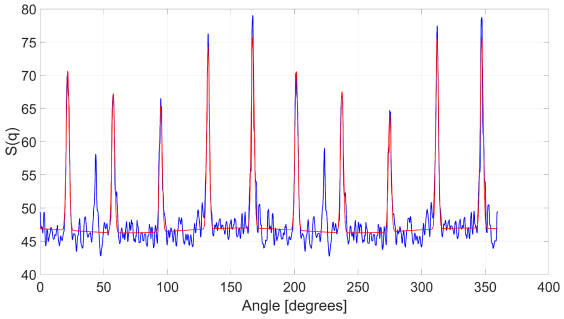

(d) Ring 4 of Template 3

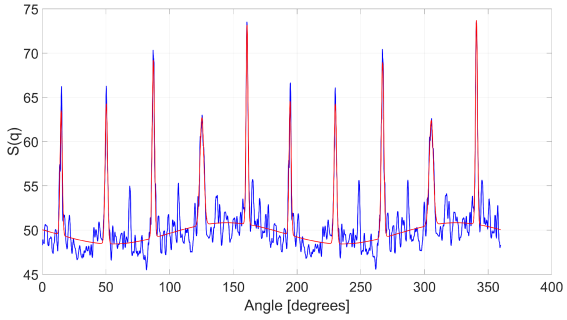

(e) Ring 5 of Template 3

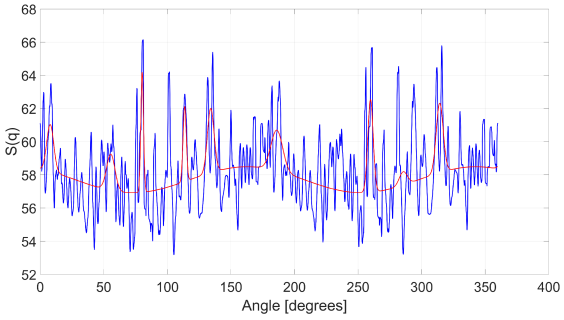

(f) Discarded fit of Ring 4 of Template 5

Figure 4.8: Ring profiles (blue) of $S(q)$ of template 3 (a-e) and ring 4 template 5 (f) with Gaussian fits to Bragg peaks (red) measured at 600 mW and $\phi_p = 1.5 \pm 0.1$.

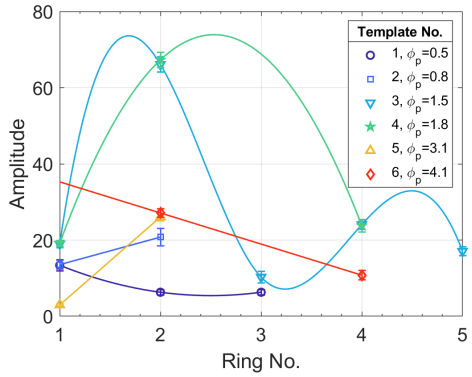

(a) Amplitudes of fitted Gaussians to Bragg peaks.

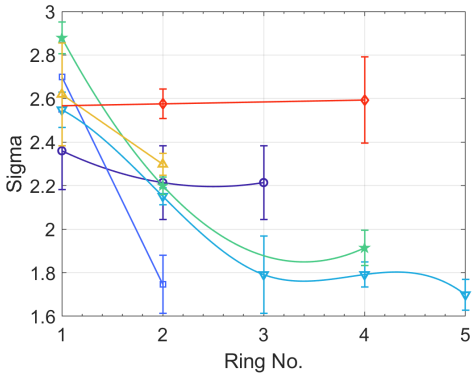

(b) Sigma values of fitted Gaussians to Bragg peaks.

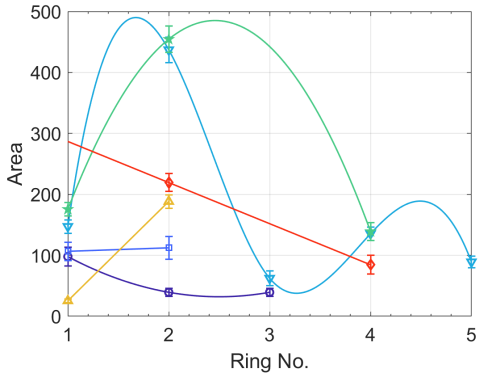

(c) Areas of fitted Gaussians to Bragg peaks.

Figure 4.9: Height, width and area of fitted Gaussians to Bragg peaks of structure factor from measurement at 600 mW, for different particle fractions and templates, see the legend. With uncertainties from fit errors. The lines are a guide to the eye.

4.1.4 Effect of Particle Fraction and Laser Intensity on Structure Factor

To study the effect of particle fraction a fixed intensity of 600 mW and template 3 were being used. At this intensity, the light field is high enough to make sure, that most of the particles get trapped in the template positions and hence form an evaluable structure. Template 3 has been chosen, since it shows the most resemblance to the reference data of the template and is the template, which shows analysable peaks in all five rings (fig. 4.10a-fig. 4.10c). For the amplitude, the first ring varies the most with particle fraction. Ring 2 has the highest and rings 3 and 5 have the lowest values following the template trend.

When the measurement results are compared to the reference-template-data shown in black

(fig. 4.10a), ring 4 is the one with the highest deviation. Here, the height is much lower than expected by the template.
Although the from factor has been removed from the measured diffraction patterns, there still seems to be a minimum of intensity in the background of the peaks between $\sim 2.48 - 4.40\,\mu m^{-1}$. This falls into the range of ring 4 for template 3 and could be an explanation for the deviation peak heights compared to the template diffraction pattern, which does have a more homogeneous dark background (fig. 4.1c).

When the particle fraction is increased, while the laser intensity is kept constant, the heights of the peaks decrease for rings 1 and 3 (fig. 4.10a). For rings 2, 4 and 5 the lowest values are found for a particle fraction of 1. The trend of the area is analogous to the amplitude data (fig. 4.10c). However, the spread of values for different ϕ_p is decreasing except for the first ring.
In the plot for the peak-widths (fig. 4.10b), the two highest fractions $\phi_p = 1.5$ and $\phi_p = 2.2$ show lower values than for $\phi_p = 1.0$. Therefore, the lower peaks for $\phi_p = 1.0$ are wider, so the area is more similar to the values for the other particle fractions.
All in all, the width of the peaks is decreasing to higher rings following the template data.

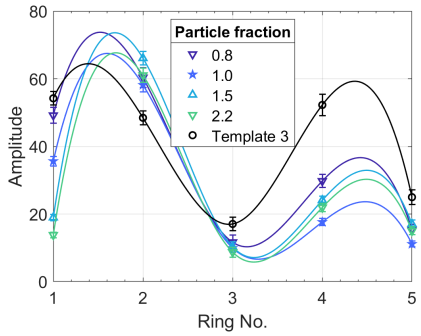

(a) Amplitude data from fit for Template 3 at 600 mW and 4 different particle fractions ϕ_p.

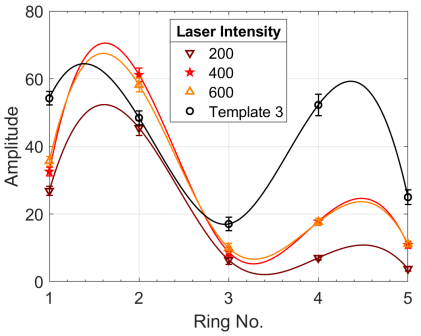

(d) Amplitude data from fit for Template 3 at different intensities and particle fraction $\phi_p = 0.9 \pm 0.1$.

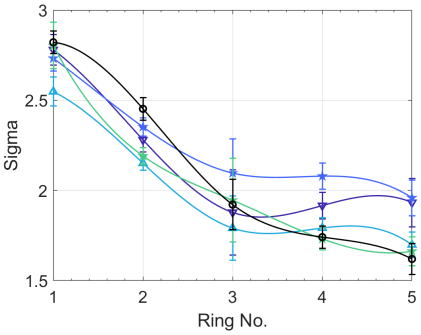

(b) Sigma data from fit for Template 3 at 600 mW and 4 different particle fractions ϕ_p.

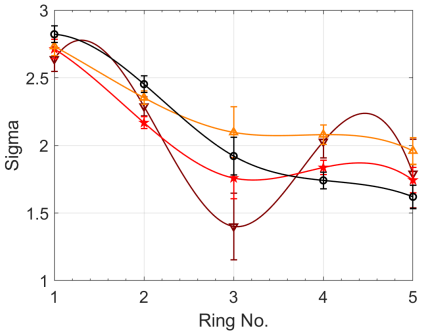

(e) Sigma data from fit for Template 3 at different intensities and particle fraction $\phi_p = 0.9 \pm 0.1$.

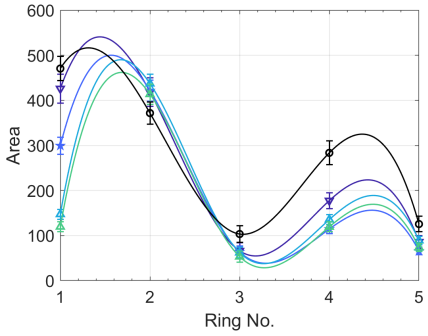

(c) Area data from fit for Template 3 at 600 mW and 4 different particle fractions ϕ_p.

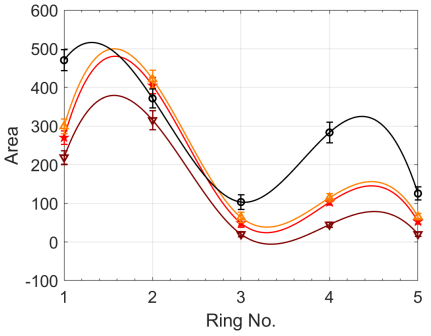

(f) Area data from fit for Template 3 at different intensities and particle fraction $\phi_p = 0.9 \pm 0.1$.

Figure 4.10: Fit parameters to Bragg peaks of the structure factor of measurements with template 3 for different particle fractions (a-c) or different laser intensities (d-f). With uncertainties from fit errors. The lines are a guide to the eye.

To study the intensity-dependence, the third template was being used again this time at a fixed particle fraction of $\phi_p = 0.9 \pm 0.1$ (fig. 4.10d-fig. 4.10f). This fraction signifies, that every template position can be occupied by $\approx 90\,\%$ of particles in the FOV. The overlaps in the template are points of higher intensity compared to the rest of the template, while the amplitude of the potential is controlled by the laser power. For one fixed template pattern, the particles are monitored for very low intensities, where only a weak 10-fold pattern without sharp Bragg peaks is formed (i. e. 125 mW and 250 mW), up to higher intensities (500 mW and 600 mW), where the structure can be further analysed due to a strong pattern signal in the structure factor.

Here, the trend reflects one of the reference data and is also similar to the measurements at different particle fractions (fig. 4.10d-fig. 4.10f). The amplitude and area are increasing with higher laser intensity, while at the lowest intensity of 200 mW the values are the lowest too. A deviation is found at the peak width for ring 3 (fig. 4.10d). For 200 mW the value is much lower than for 400 mW and 600 mW, but also the fit error is larger. Hence the line as guide-to-the-eye has a higher curvature than the others. Overall the peak width is comparable in the intensity range of 200 mW to 600 mW.

As a measure for location accuracy of the peaks the standard deviation s of deviation $dev = \frac{36-\beta_n}{36}$ from the ideal separation between the peaks of 36° is calculated

$$s = \sqrt{\frac{1}{N-1}\sum_{n=1}^{N}(dev_n - \overline{dev})^2}\ . \tag{4.1}$$

Since the mean of 10 peaks on one ring is vanishing, $\overline{dev} = 0$, the standard deviation becomes

$$s = \sqrt{\frac{1}{N-1}\sum_{n=1}^{N}{dev_n}^2}\ . \tag{4.2}$$

The curves for templates 3, 4 and 5 have a similar shape (fig. 4.11a). The deviation for rings 2 and 4 is the lowest. Template 5 has the highest deviation and especially ring 3 is striking. The remaining templates 1, 2 and 6 also show a similar trend, where the values for higher q are decreasing. Templates 1 and 2 show the least variation among all other templates. In (fig. 4.11b) the difference in deviation $s = s_m - s_t$ between measurements and templates is plotted. The deviations are higher than for the templates (fig. 4.11a) and only for template 3 data for all rings could be evaluated.

The Bragg peak locations for template 3 will be analysed further for different intensities and particle fractions. As seen in (fig. 4.11c), the laser intensity does not seem to have a high dependency on the location accuracy. Except for ring 3, the deviation is decreasing with higher intensity and there is one value for ring 5 at 200 mW, which seems to be an outlier. A similar trend is seen for different particle fractions (fig. 4.11d). The location accuracy for the peaks on ring 3 is getting worse with particle fraction as well as laser intensity.

To sum up, the location accuracy is slightly lower than for the template reference, but overall follows the same trend and shows a slight tendency to less accuracy with higher particle fraction and higher accuracy with increasing intensity.

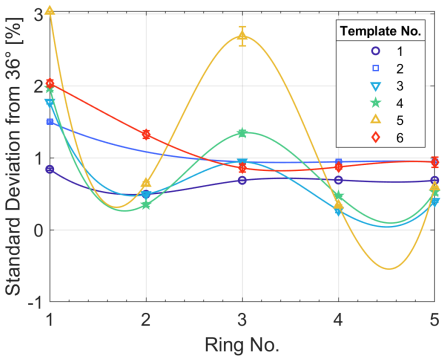

(a) Location accuracy of Bragg peaks of templates as deviation from ideal positions at 36°.

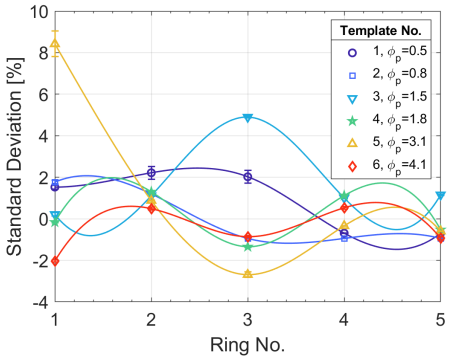

(b) Location accuracy of Bragg peaks of measurements at 600 mW with regard to template accuracy (fig. 4.11a).

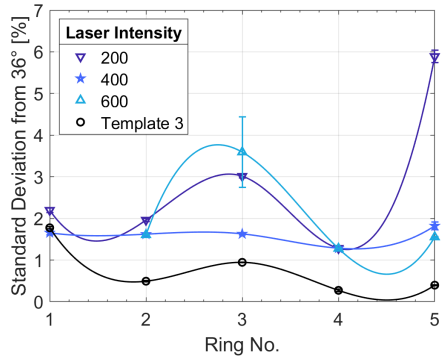

(c) Location accuracy of Bragg peaks of measurements at different intensities and $\phi_p = 1.3 \pm 0.1$.

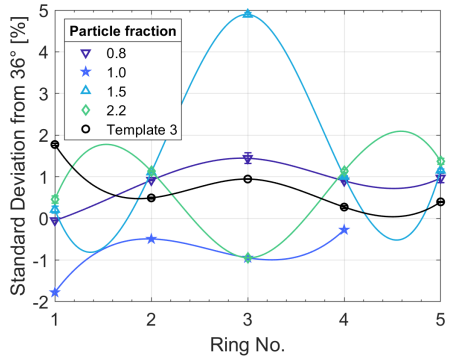

(d) Location accuracy of Bragg peaks of measurements at different particle fractions and 600 mW.

Figure 4.11: Standard deviation of deviation from ideal Bragg peaks positions, separated by 36°. With uncertainties from fit errors. The lines are a guide to the eye.

4.1.5 Radial Distribution Function

The radial distribution functions show peaks at different distances for templates 3 and 5. When comparing the radial distribution of the structures formed from the particles with the ones of the templates as a reference, the maxima fall on top of each other (fig. 4.12). The first peak is the most pronounced and stems from particles, which are separated by one

particle diameter, which is the smallest separation possible for hard spheres. The locations of the second and third peaks in $g(r)$ (fig. 4.12) match the numbers in table 3.2, which are the values of the main lengths in the templates and coincide with the peaks of the templates (black lines) as expected. The height of the template peaks has been multiplied by a factor of 0.09 in the plots to ease the comparison with the $g(r)$ of the measurements. The peaks of the measured structures are broader and lower than for the template reference. This is due to imperfections in the structure since the particles are moving and the template structure is static.

For one template the curves for all intensities fall on top of each other. The height of the peaks, however, varies with laser intensity. While it rises for higher intensities for template 3, the peaks are highest for 600 mW in template 5.

When scaling the x-axis with the shortest main lengths in the respective templates, the 2nd peaks stemming from this length fall on top of each other (inset of fig. 4.12b). The higher peaks are deviating more in between the templates as well as with respect to the x-axis. E. g. the third peaks of templates 3 and 5 already do not match and the location of the fourth peak is not found at an integer value.

When comparing the radial distribution of all templates to the measurement, the first peaks only match the first two templates (fig. 4.13). Here, the template distances are the closest to the particle diameter d with $0.91\,d$ and $1.15\,d$ respectively. Hence the particles, which are touching each other are still in template positions.
As the template distances get larger the second peak of $g(r)$ matches the first peak in g(r) of the template. Since the smallest possible distance for the particles is closer than prescribed by the template, some particles can be, temporarily, located in between the template positions if they are not trapped at a tiling position contributing to the peaks.

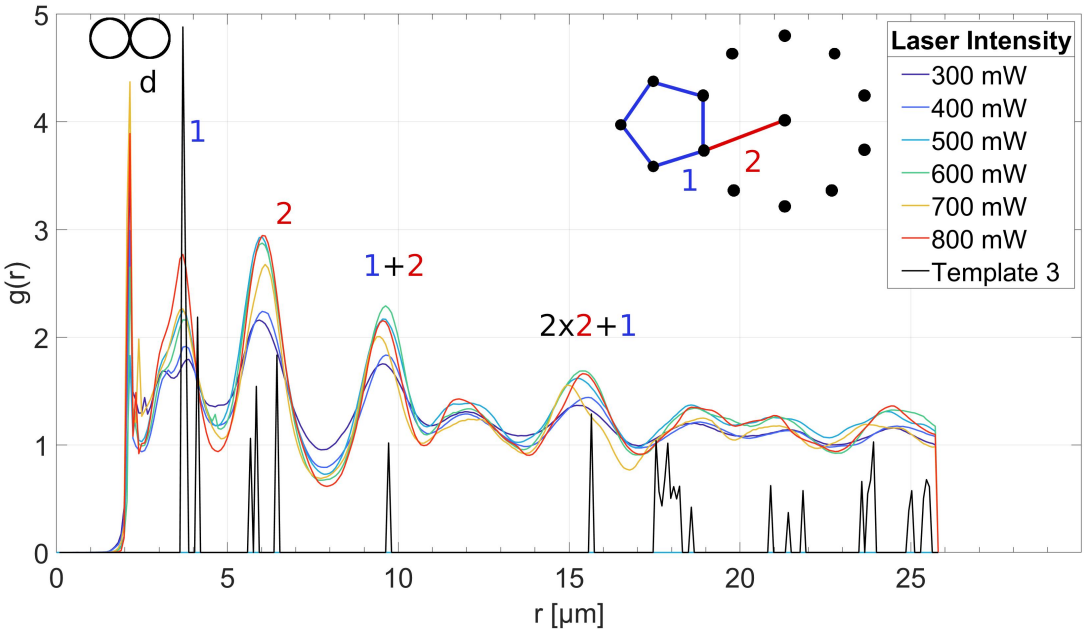

(a) Averaged radial distribution for template 3. Inset: Tiling distances "1" and "2" as short and long main length.

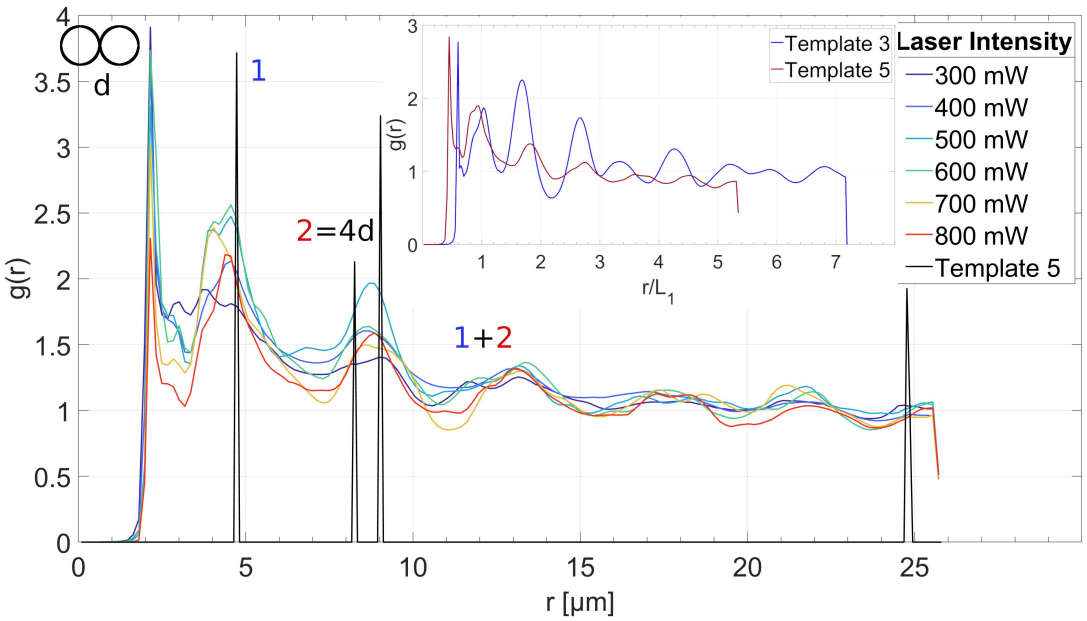

(b) Averaged radial distribution for template 5. Inset: g(r) for template 3 (blue) and 5 (red), where the x-axis has been divided by the shortest main length of the respective template.

Figure 4.12: Averaged radial distributions $g(r)$ for template 3 and 5 ($\phi_p = 0.9 \pm 0.1$) at different intensities (see legend) and possible inter-particle distances 1 and 2 (see inset in(a)) leading to peaks, where d is the particle diameter and 1 and 2 are the main lengths in the tiling as depicted. Template reference data is drawn in black.

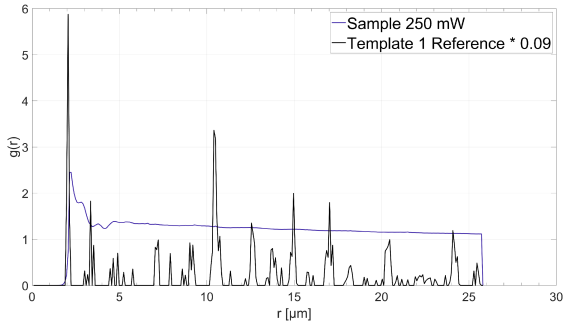

(a) Radial distribution of template 1 and sample measured with the same template.

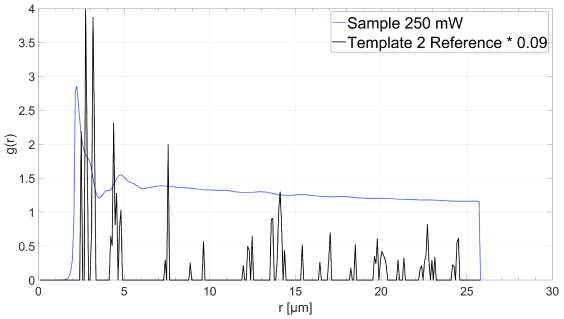

(b) Radial distribution of template 2 and sample measured with the same template.

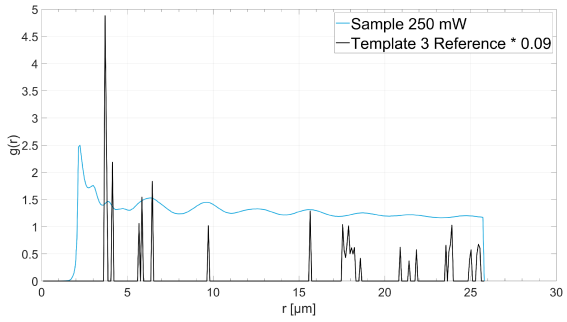

(c) Radial distribution of template 3 and sample measured with the same template.

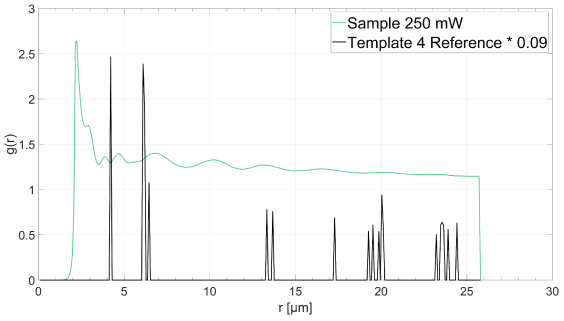

(d) Radial distribution of template 4 and sample measured with the same template.

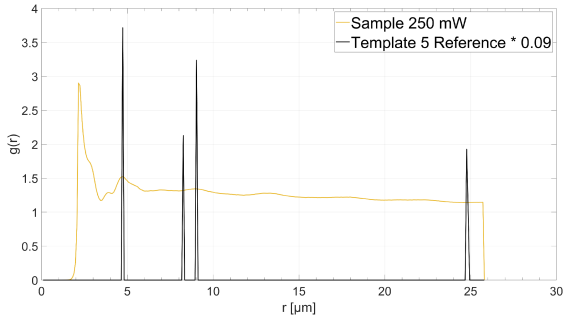

(e) Radial distribution of template 5 and sample measured with the same template.

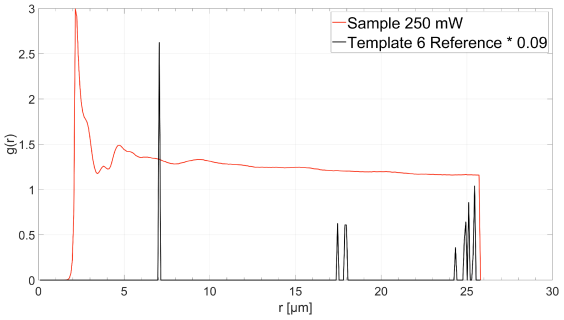

(f) Radial distribution of template 6 and sample measured with the same template.

Figure 4.13: Radial distribution functions of measurements (250 mW, $\phi_p = 0.9 \pm 0.1$) compared to template reference.

4.1.6 Discussion on Structure Formation

For short tiling distances as well as for long distances the signal in the structure factor is less similar to the template reference structure factor than for medium lengths in templates 3 and 4 (fig. 4.6). The signal in templates 5 and 6 appears lower due to the lower density of repetitions in the FOV at larger template distances. Since the number of repetitions, and therefore particles at template positions, contribute to a larger diffraction amplitude for one specific direction. The appearance of a peak is an indicator of a configuration of positions preferred by the given symmetry. Hence a higher density of points for one bond order orientation raises the diffraction amplitude and contributes to the intensity of the Bragg peak (eq. (2.76)).

For template 3 the structure factor was most pronounced with a strong signal (fig. 4.6c). Here, the tiling distances with regard to the particle and FOV sizes led to a greater 10-fold signal than with the other templates. This trend is also appearing in the results of the dynamics experiments following in the next section.

It was shown in the measurements (section 4.1.4), that different particle fractions only had a small effect on the overall structure signal. However, for ring 2 the peaks tend to be higher and more narrow than the reference in contrast to the other rings, where the peaks are lower and wider. At higher particle fractions the probability is higher to encounter particles separated by a shorter distance. Therefore, the Bragg peaks in ring 2 are higher and more narrow than for the other rings.

There seems to be no clear trend for the Bragg peaks with increasing particle fraction (fig. 4.10a-fig. 4.10c). By neglecting the lowest measured particle fraction of $\phi_p = 0.8$, the trend goes to lower but wider peaks for lower concentrations. It is possible, that the data for the lowest concentration is less reliable due to errors in defining ϕ_p.
The error bars plotted here are from fit-error data. Alternatively, the standard deviation from averaging over the ten peaks on a ring could be calculated.
However, what can be seen from this data is, that the measurements are following the template trend and there is a similar overall trend for the ring-dependency, i. e. the minimum at ring 3.

This can be explained with the construction and combination of Bragg peaks on rings 3-5 from the wave vectors forming rings 1 and 2.
The peaks on the first ring stem from the longer main length, whereas the shorter length contributes to the second ring (fig. 2.6b). Since the second ring is created from the smaller length scale, its intensity is higher, because a smaller length can have more repetitions in the FOV and hence contribute to a higher signal (see fig. 4.3). The Bragg peaks located on rings 3 to 5 can be constructed from adjacent vectors on ring 1 and are lower in intensity (fig. 4.2). The signal of ring 3 is lower than that of ring 5 since these peaks stem from the combination of longer length scales. As in the case of ring 1, the peaks of the less occurring longer length are lower in intensity. Ring 4 is constructed by summation of vectors of the

shorter length on ring 2, which are separated by 72°. This is twice the angle of the adjacent ring 2 vectors, which form the fifth ring, and can therefore be constructed from the 5 in-plane basis vectors.

Another factor that can influence the Bragg peak intensity is the surface fraction. For template 1 the upper limit for particles to arrange in 3D is reached with 63 % and it's close to the maximal packing fraction in 2D, which is reported to be around 0.8525 % [117]. Therefore, a 10-fold arrangement according to template 1 will be more difficult to achieve, resulting in lower Bragg peak amplitudes of templates 1 and 2 (fig. 4.6a,fig. 4.6b).

There are traps with different strengths and sizes in the templates. As mentioned, the laser intensity influences the strength of the potential and therefore the stiffness of the traps. Positions with a higher probability to find particles are located at template positions with a stronger light field potential. For high laser intensities, the particles differentiate between these positions of different potential strengths and hence are more often found in template positions, which contribute to the decagonal symmetry. If the laser intensity is decreased, the colloidal interactions become more important and some particles leave the potential minima to other positions, which are not necessarily contributing to a 10-fold signal in the structure factor. Therefore, the amplitude, width and therefore area of the peaks get larger for higher intensities. As for the location accuracy, a higher intensity seems to improve the peak location with an exception for ring 3.

An explanation for a better location accuracy could be delivered with lower particle mobility at higher laser intensity. Since the stiffness of a trap rises with laser power, the probability for a particle to be trapped rises with higher intensities. Therefore, the Bragg peaks should be located at the predefined positions.

For a well-reproduced decagonal symmetry of the template, the laser power should be set to the lowest value, where the structure factor does not improve with an increase in intensity. Hence where the Bragg peaks are clearly distinguished from the background noise.
A higher intensity will reduce particle dynamics and therefore the ability to reduce or heal defects in the tiling, but also decrease the background noise in the diffraction pattern due to diffuse scattering. On the other hand, if the intensity is too low, the trap stiffness at the template positions is reduced and inter-particle interactions will dominate over the external potential.

For template 1 and 2 the first $g(r)$-peaks coincide with the shortest main length analogous to the second wave vector of the structure factor (fig. 4.13a-fig. 4.13b, table 4.1). Since the shortest tiling distances are similar to the particle diameter (2.1 µm), the first peak of the radial distributions of measurements and templates fall on top of each other.
For greater tiling distances in templates 3 to 6, the first peak does not coincide with the $g(r)$-peak of the respective template. Here, the particles are located in between the template positions resulting in the first peak at $\sim 2.1\,\mu m$. Due to the construction of the templates from the double rings, the overlaps are also appearing in between the positions e. g. in the

centres of the pentagons, creating additional intensity maxima. Therefore, particles can occupy distances, which are shorter than prescribed by the main template distances.

Template 6 shows the greatest deviation between template and measurement (fig. 4.13f). Here, the first peak of the template only slightly matches the second measurement peak. The distances in template 6 were the largest of all templates. Because of this great discrepancy between tiling distance and particle size of $5.76/2.1 \approx 2.74$, it is more difficult for the particles to align according to the pattern of the template without defects or additional particles at places, which do not contribute to the 10-fold rotational symmetry.
Moreover, when comparing the number of repetitions that contribute to the long-range orientational order in the FOV between the templates, it is lower, the greater the distances between the template positions. Hence they also have an impact on the signal in the structure factor with regard to the size of the FOV. If the repetitions are occurring less frequently as in template 6, then the peaks in the structure factor as well as in the radial distribution will not be as pronounced in contrast to the background.

The radial distributions for templates 3 and 5 have been analysed in more detail since they were also used in the particle dynamics experiments. Distances that are either prescribed by the template or in the case of the first peak by the particle diameter, have been assigned to the peaks of $g(r)$ as seen in fig. 4.12. When scaling the x-axis with the shortest main lengths of the respective tilings, mainly the second peaks fall on top of each other. For higher peaks, the deviation is greater between the templates and the peaks mostly do not match with the scaling of the x-axis, indicating that the higher peaks do not relate to the short main length. Instead they could stem from the longer main length or other lengths which can not be well defnied for peaks at greater distances, where the uncertainty increases.

Furthermore, in template 3 even the sixth peak of $g(r)$, is well pronounced. In contrast, the curves in template 5 approach the value of 1 at larger distances signifying a transition from an ordered to a disordered structure. This again shows, that the particles in template 3 exhibit a more ordered structure according to the pattern than for the other templates.

4.2 Particle Dynamics on Quasicrystalline Templates

For an in-depth study of particle movements in the decagonal light fields, the trajectories were plotted and analysed. In fig. 4.14 some trajectories were plotted colour-coded after the particle's location on top of a snapshot of the measurements. Trajectories that are near a template position at the start are coloured green, those that are in or near a trap either at the start or at the end of the measurement are coloured blue and trajectories, which are passing a template position during the measurement, but are not located inside of a trap at the start or end are coloured yellow. The pink trajectories are of no interest here since they are located outside of the template. It can be seen by comparing the images to each other, that in template 3 the fraction of blue particles relative to all is much higher than in template 5. Furthermore, in template 5 there are many green trajectories, i. e. particles, which are near a trap in the beginning but not at the end (fig. 4.14a). Therefore, there are more particles in template 5 which escape trap positions during the measurement.

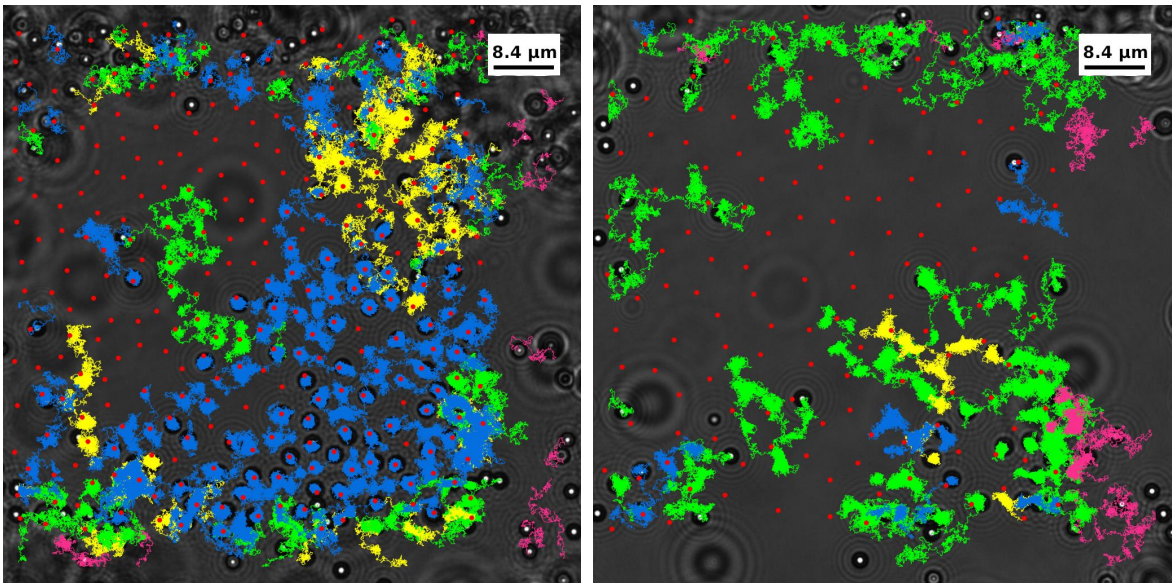

(a) Trajectories on a snapshot of a measurement (400 mW, $\phi_p = 0.4$, Template 3).

(b) Trajectories on a snapshot of a measurement (400 mW, $\phi_p = 0.5$, Template 5).

Figure 4.14: Particle trajectories on a snapshot of measurements, with particles trapped at the start (green), end or start and end (blue), and particles, which pass traps during a measurement (yellow), but are not near a trap at the start or end. The trajectories in pink are from none of these cases and are mostly tracking noise. The template positions are represented by red dots.

Further on, the particle behaviour will be measured in the light field at different laser intensities. The particle fraction was kept constant and low, $\phi_{p3} = 0.118 \pm 0.006$ for template 3 and $\phi_{p5} = 0.33 \pm 0.06$ for template 5, so inter-particle interactions could be neglected. To finish, the influence of the particle concentration will be studied by increasing the particle fraction and recording the sample at a fixed laser intensity of 400 mW.

4.2.1 Probability Distribution of Jump Times

Form the phop-algorithm as introduced in section 3.7.2, particle jumps are registered over a threshold value $p_{th} > p_{hop}(t)$ and their coordinates in space and time can be retrieved.

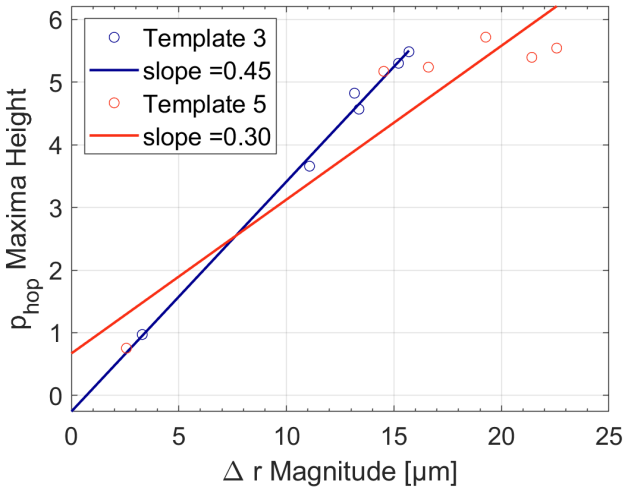

Figure 4.15: Proportionality between heights of Phop-maxima and the length of Δr covered in the time interval $T = 40\,s$ of the phop evaluation.

There exist a proportionality between the heights of the maxima in $p_{hop}(t)$ and the magnitude of a jump $|\Delta r|$, where Δr is the input for the phop-algorithm as defined in eq. (3.18). The magnitude can be quantified with a distance

$$|\Delta r| = |\Delta r(t_2) - \Delta r(t_1)| \,, \tag{4.3}$$

where $t_1 = t_{hop} - T$ and $t_2 = t_{hop} + T$ are two points in time around the jump time point t_{hop} and $T = 40\,s$ is the time interval for phop-evaluation (see red parts of $\Delta r(t)$-trajectory in fig. 4.16c-fig. 4.16d). Then $|\Delta r|$ is proportional to the height of the peaks in p_{hop}

$$p_{hop} = b_i \, |\Delta r| \tag{4.4}$$

with the slope form fit $b_3 \approx 0.45$ for template 3 and slightly lower for template 5 with $b_5 \approx 0.30$. fig. 4.15 shows the proportionality.

The registered jumps can be plotted on the particle's trajectory, like in fig. 4.16a-fig. 4.16b as red dots. When looking at the trajectories of particles in templates 3 and 5, one can already see some differences by eye. For template 5 there is a more diffuse particle track (fig. 4.16b), while the trajectory of template 3 seems to have more well-defined spots of high density, where the particle lingers for a while. The registered jumps (red dots) in the trajectory of template 3 are located inside compact parts of the trajectory, but not in between, where the trajectory is less compact (fig. 4.16a). In contrast in template 5, the jumps are more evenly distributed on the trajectory.

After determining the coordinates of the jumps with the phop-algorithm, the hop times τ_h (eq. (3.20)), i. e. the times between these jumps can be retrieved next. However, these times can have different interpretations. For one it can signify a particle's jump from one template position to a neighbouring one, or an escape of a particle from a cage of surrounding particles which should however be dependent on the particle concentration.
On the other hand, jumps can also be registered, while the particle remains in an individual minimum as seen in fig. 4.16a-fig. 4.16b. Therefore, registering the fluctuations of particle positions inside of the trap.

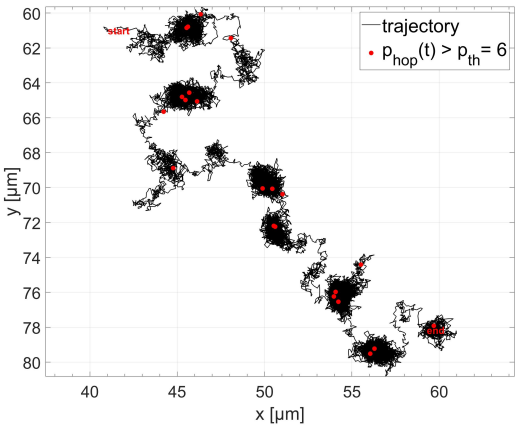

(a) An exemplary particle trajectory in template 3 (Jumps marked as red dots).

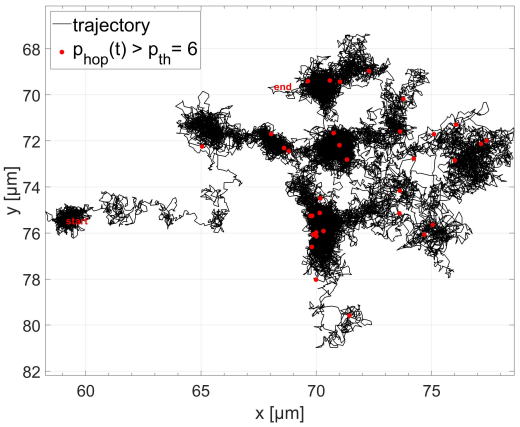

(b) An exemplary particle trajectory in template 5 (Jumps marked as red dots).

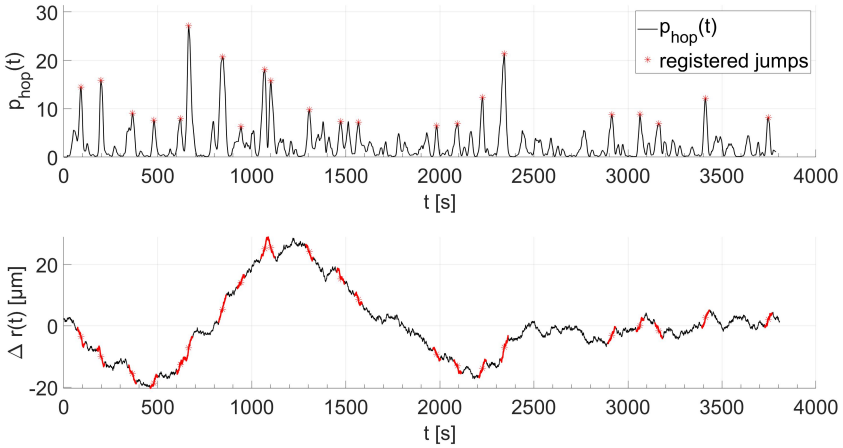

(c) Phop-function and $\Delta r(t)$ for the trajectory depicted in fig. 4.16a.

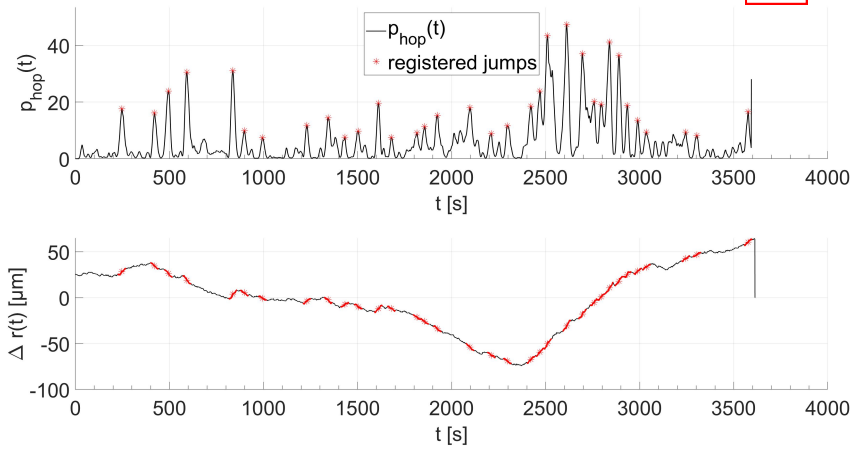

(d) Phop-function and $\Delta r(t)$ for the trajectory depicted in fig. 4.16b.

Figure 4.16: Particle trajectories and phop-function for template 3 (400 mW, $\phi_p = 1.2$) and 5 (400 mW, $\phi_p = 0.4$) with corresponding $\Delta r(t)$-values after eq. (3.18). The threshold value for identifying jumps is $p_{th} = 6$.

To register jumps with as little noise as possible, p_{th} should be chosen at around the height of the maxima in p_{hop}. In fig. 4.16c-fig. 4.16d the phop-function is plotted together with the values for $\Delta r(t_i)$ as defined in eq. (3.18). With a threshold of $p_{th} = 6$, the algorithm registered particle escapes, as well as the most prominent changes in particle trajectories inside of a minimum. If a lower threshold would have been chosen, the phop-algorithm would additionally register noise. A value greater than 6 would omit some larger jumps. Therefore, in this case, $p_{th} = 6$ delivered the most reasonable results.

For several particles, the hop times τ_h are averaged over $\gtrsim 2000$ jumps per measurement for one intensity and particle fraction. The probability distribution of these averaged hop times $P(\langle\tau_h(t)\rangle)$ is plotted for the intensity-dependent measurements and the measurements with variable particle fractions. It shows, that the distributions can be fitted at short t_s and long times t_l separately with an exponential

$$f_s(t) = a_s \exp[-t/t_s], \quad f_l(t) = a_l \exp[-t/t_l] \ , \tag{4.5}$$

in an adequate range of τ_h, where the trend is exponential.

From the fit parameters, the mean short and long hop times can be retrieved and plotted against the intensity and particle fraction (fig. 4.17e-fig. 4.17f). For both templates the longer hop time increases with laser intensity and reach a plateau for the highest measured laser powers (fig. 4.17e). For short times the values fluctuate around $t_s = 163\,s \pm 18\,s$ for template 3 and $t_s = 121\,s \pm 27\,s$ for template 5 (see horizontal lines in fig. 4.17e). As the intensity increases the difference between short and long times becomes more evident. E. g. for the lowest measured intensity of 300 mW, there is an overlap for both times inside the errors.
For long times, however, the curves diverge above 300 mW. The difference between short and long times is less for template 5 and therefore the longer times of template 5 are below those for template 3.

The influence of increasing particle fraction seems to have no effect on the short hop times, which fluctuate around $t_s = 131\,s \pm 20\,s$ for template 3 and $t_s = 136\,s \pm 38\,s$ (see horizontal lines in fig. 4.17f) similarly to the trend for different intensities, but with greater deviations. For the longer times, the times seem to decrease slightly for template 3, while it's oscillating for template 5, i. e. increasing for $\phi_p = 0.4, \phi_p = 0.9$ and $\phi_p = 1.2$ and decreasing for $\phi_p = 0.7$ and $\phi_p = 1.1$. The mean of these fluctuations is around $236\,s \pm 38\,s$, whereas the lowest data point for template 3 is at $272.8\,s$. Furthermore, the mean of shorter times for template 5 is at $109\,s \pm 27\,s$, which is only $\sim 127\,s$ lower than the mean for long times. This shows, that the short and long times of template 5 are more similar and split into the two regimes of times between jumps is not as clear as for template 3.

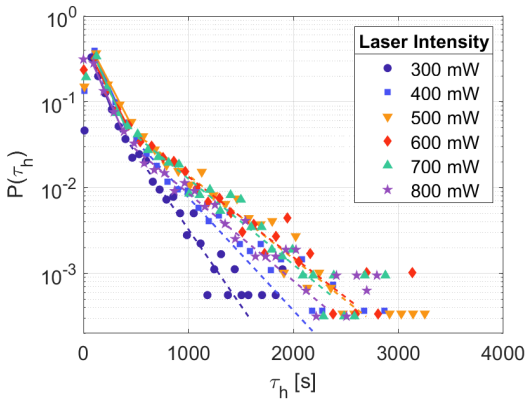

(a) Probability distributions for hop times dependent on laser intensity for template 3 at $\phi_p = 0.118 \pm 0.006$.

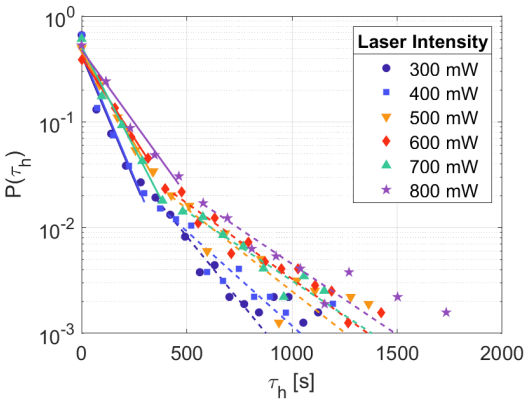

(b) Probability distributions for hop times dependent on laser intensity for template 5 at $\phi_p = 0.33 \pm 0.06$.

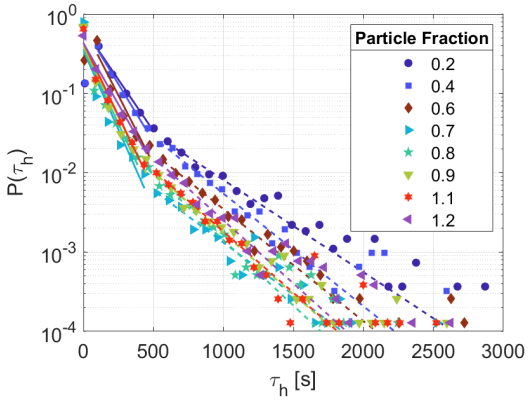

(c) Probability distributions for hop times dependent on particle fraction for template 3 at 400 mW.

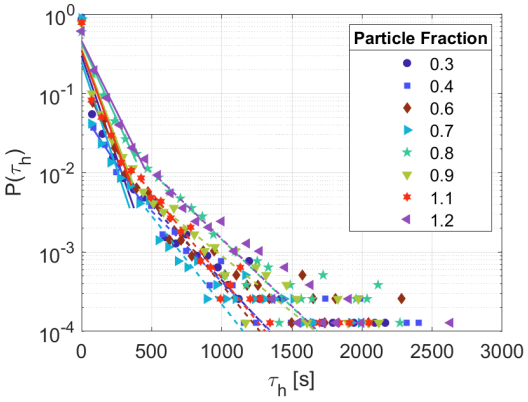

(d) Probability distributions for hop times dependent on particle fraction for template 5 at 400 mW.

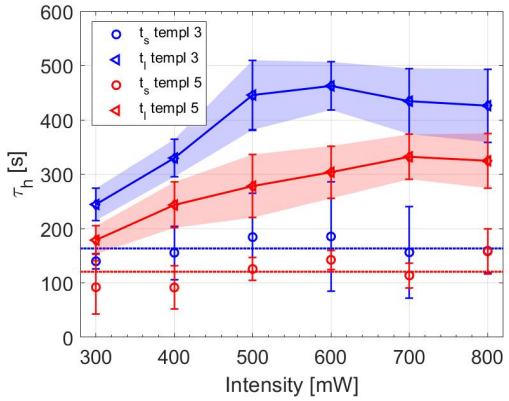

(e) Average short and long hop times dependent on laser intensity.

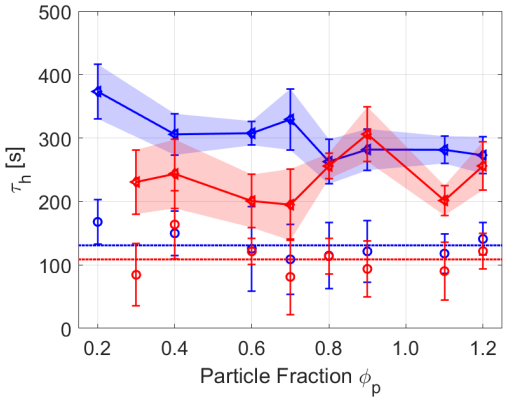

(f) Average short and long hop times dependent on particle fraction.

Figure 4.17: Probability distributions of hop times, dependent on intensity (a)-(b) and particle fraction (c)-(d), with exponential fits at short (solid lines) and long times (dashed lines). (e)-(f) Short and long hop times, t_s and t_l, from exponential fits in (a)-(d). The lines are drawn at mean values for short times.

4.2.2 Probability Distribution of Particle Distances

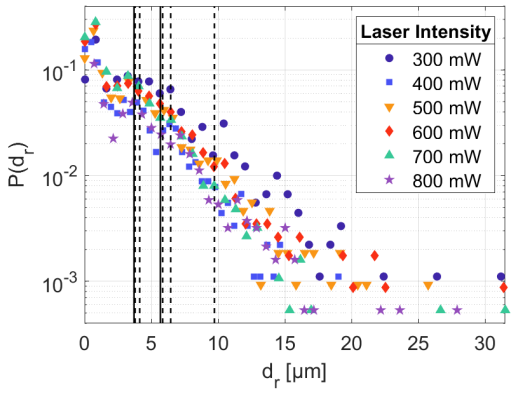

(a) Probability distributions for jump distances dependent on laser intensity for for template 3 at $\phi_p = 0.118 \pm 0.006$.

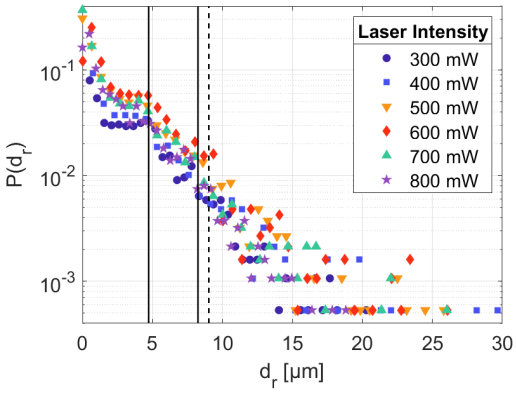

(b) Probability distributions for jump distances dependent on laser intensity for for template 5 at $\phi_p = 0.33 \pm 0.06$.

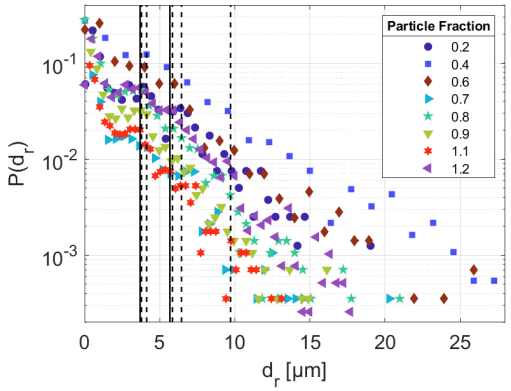

(c) Probability distributions for jump distances dependent on particle fraction for template 3 at 400 mW.

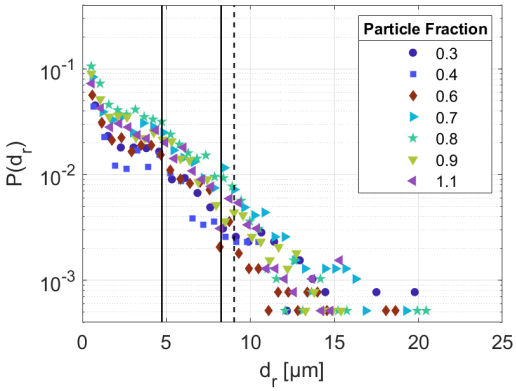

(d) Probability distributions for jump distances dependent on particle fraction for template 5 at 400 mW.

Figure 4.18: Probability distributions of jump distances dependent on intensity (a)-(b) and particle fraction (c)-(d). The black solid lines show the main tiling distances of the respective template after table 3.2.

Like for the hop times, the probability distribution of the distances between registered jumps can be plotted (fig. 4.18), but no exponential fit can be performed. The curves show at least two more or less pronounced peaks at distances, which fall on top of the main lengths found in the respective templates. For this, the location of solid black lines in fig. 4.18 can be compared to values in table 3.2) and also to the peak locations of $g(r)$ in fig. 4.12. This shows, that the particles have a higher probability to jump a distance, which is prescribed by the template structure.

For template 5 however, there is a plateau starting at around the particle diameter ($\sim 2.1\,\mu m$) and ending at the short main length in the template ($\sim 4.81\,\mu m$). A second peak is indicated at the second longer main length of the tiling.
The dashed lines in the distributions (fig. 4.18) indicate the positions of higher $g(r)$-peaks of the templates (fig. 4.12, black lines). They also seem to be overlapping with peaks for some curves, e. g. 300 mW for template 3 (fig. 4.18a).

4.2.3 Residence Times from Packing Coefficient

To estimate the size of the confinement the particles encounter in the templates, the MSD of confined particles has been calculated and the approached plateau value was determined. Using eq. (3.24) the confinement length scales can then be determined. In fig. 4.19 the average values for measurements with templates 3 and 5 at different laser intensities and particle fractions are plotted.

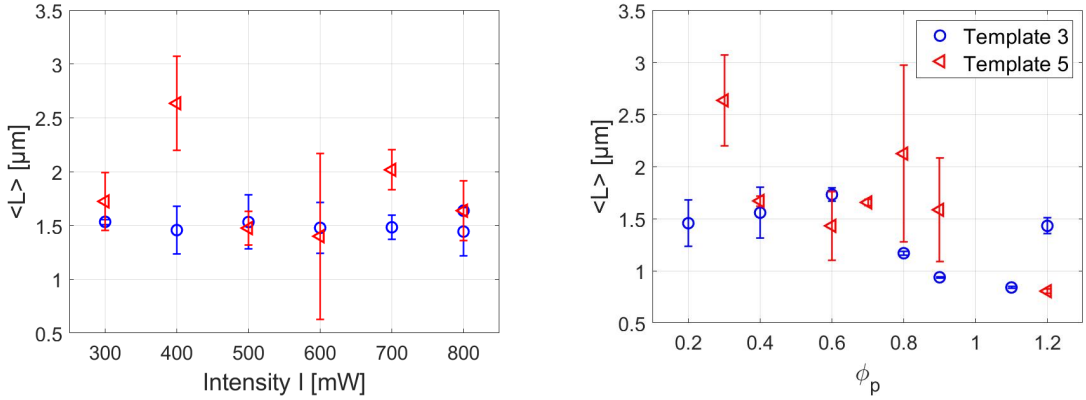

(a) Average confinement lengths dependent on laser intensity. For legend see fig. 4.19b.

(b) Average confinement lengths dependent on particle fraction.

Figure 4.19: Average confinement lengths L for Template 3 (blue circles) and 5 (red triangles).

For template 3 the general trend is a lower length scale L for higher intensity as well as higher packing fraction. The values are in the range of $L = [1\,\mu m, 1.8\,\mu m]$. The confinement

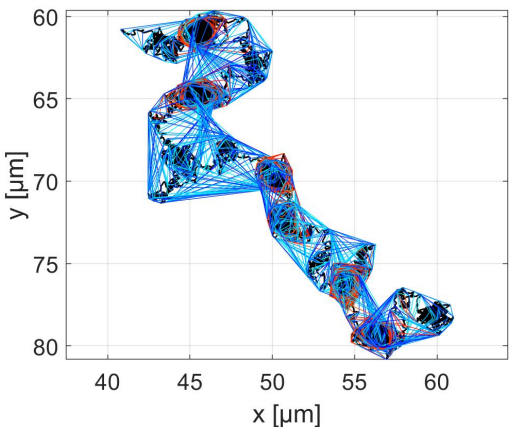

(a) Trajectory in template 3 (400 mW, $\phi_p = 1.2$).

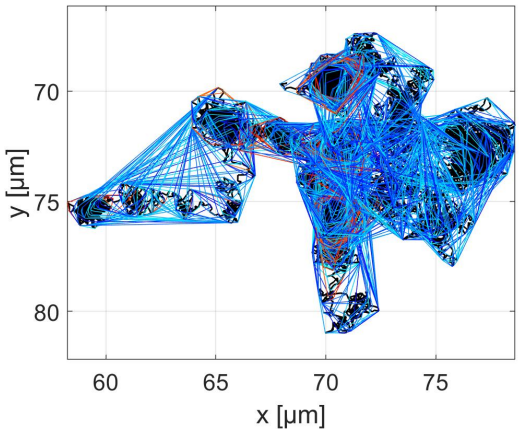

(b) Trajectory in template 5 (400 mW, $\phi_p = 0.4$).

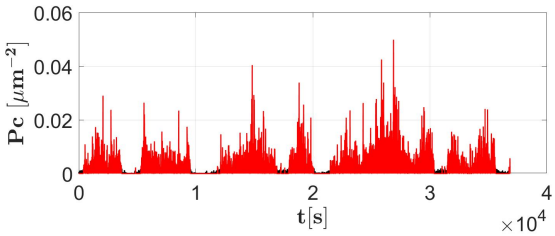

(c) Packing coefficient $Pc(t)$ for the trajectory depicted in fig. 4.19a.

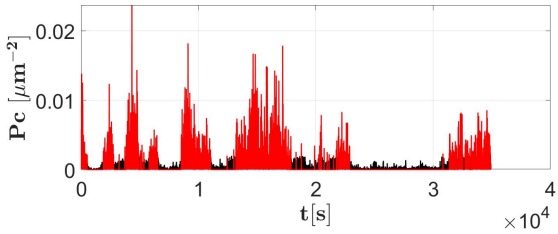

(d) Packing coefficient $Pc(t)$ for the trajectory depicted in fig. 4.19b.

Figure 4.20: (a)-(b) Exemplary particle trajectories with convex hulls as calculated for the packing coefficient. The reddish colour of the convex hull indicates a higher packing coefficient and therefore a confined particle movement. (c)-(d) Packing coefficient $Pc(t)$ plotted against the measurement time. The red intervals were $Pc > Pc_{th}$ is above a threshold $Pc_{th} = 0.002\,\mu m^{-2}$ were used to estimate the residence times τ_r.

sizes are mostly larger for template 5 compared to the sizes in template 3. Furthermore, they span a greater range of values, i. e. from $\sim 1\,\mu m$ to $\sim 2.6\,\mu m$ and the error bars are longer, meaning that the standard deviation for each value is greater. Hence the trap sizes are spread over a greater range for template 5 than for template 3. Overall the confinement sizes are smaller for high intensities and high particle fractions like for template 3.

For estimating the time a particle spends confined, the packing coefficient has been calculated using eq. (3.23), where the time interval n has been set to 120 s. In fig. 4.20a-fig. 4.20b two trajectories in templates 3 and 5 are shown together with a convex hull, colour-coded after the values of the calculated packing coefficient. A blueish colour indicates a low packing coefficient below a threshold value Pc_{th} and therefore a less compact trajectory, while a reddish colour indicates a confined movement. The threshold Pc_{th} has been chosen so, that the MSD of trajectories with Pc_{th} was indicative of confined motion, i. e. that can be described with eq. (2.58) showing a plateau value as in fig. 2.9.

The convex hulls in fig. 4.20 can be compared to the same trajectories in fig. 4.16a and fig. 4.16b, where the registered particle hops are marked as red dots. It shows, that most of the jumps are located, where the packing coefficient is high. For the trajectory in template 5, however, particle hops can also be found where the trajectory is less confined (fig. 4.16b).

The duration of intervals with a packing coefficient above the chosen threshold ($Pc_{th} = 0.002\,\mu m^{-2}$) has been determined (red parts in fig. 4.20c-fig. 4.20d) and averaged over the times from all trajectories for one intensity and particle fraction. The probability distributions have been plotted like the distributions of the times in between two registered particle jumps from the phop-function (fig. 4.21a-fig. 4.21d). Here, an exponential function can be fitted until $\sim 1500\,s$ from where the values at higher times become too uncertain for a fit. Furthermore, the first data points have been omitted too because of deviations from the exponential trend.
Additionally, it shows, that for very long times ($\simeq 3400\,s$) the probability rises for some intensities and particle fractions. This is especially visible in fig. 4.21a and stems from particles, which have been confined during the whole duration of the measurement, which lasted $\sim 3600\,s$. These can be on one hand particles, which were stuck to the glass of the sample, but were tracked like other particles. On the other hand, there are particles, which were trapped in the light field or confined in a cage leading to a higher probability here. But the peak at longer times also needs to be interpreted with caution since the uncertainty in this range is high.

The residence times τ_r can then be retrieved from the exponent of the fit like for the jump times τ_h before and plotted against the laser intensity and particle fraction (fig. 4.21e-fig. 4.21f).
The times τ_r retrieved here are slightly higher than the long hop times t_l as determined by the phop-algorithm. Like for the hop times (fig. 4.21e-fig. 4.21f), the values for template 3 are also higher than for template 5. Moreover, the trend for higher laser power and particle fraction is similar to the long dwell times t_l from phop. The residence times τ_r found here (fig. 4.21e), are increasing with higher laser intensity and the dependence on the particle fraction is similar to the times from phop (fig. 4.17f). The residence times for template 3 are decreasing, while there seems to be no dependency for template 5.

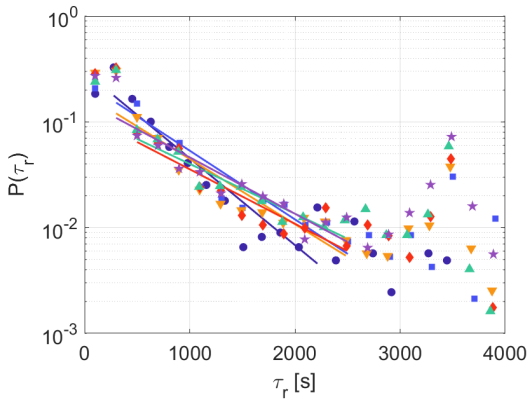

(a) Probability distributions for residence times dependent on laser intensity for for template 3 at $\phi_p = 0.118 \pm 0.006$. For legend see fig. 4.21b.

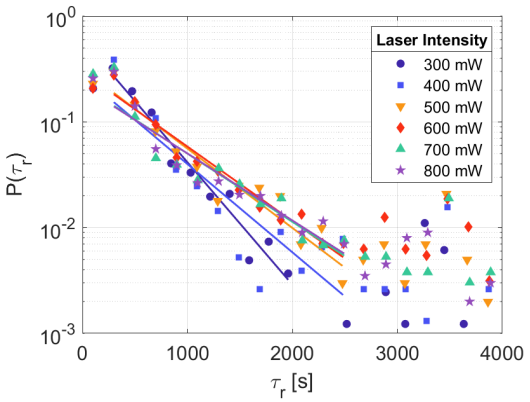

(b) Probability distributions for residence times dependent on laser intensity for for template 5 at $\phi_p = 0.33 \pm 0.06$.

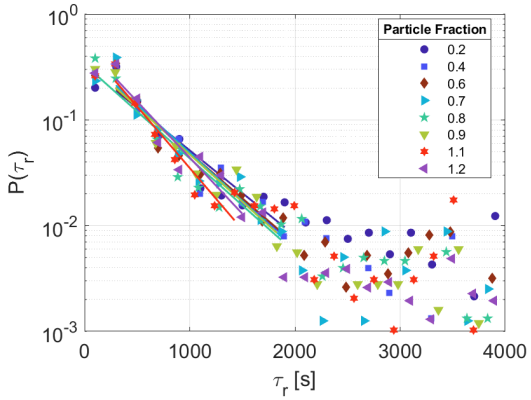

(c) Probability distributions for residence times dependent on particle fraction for template 3 at 400 mW.

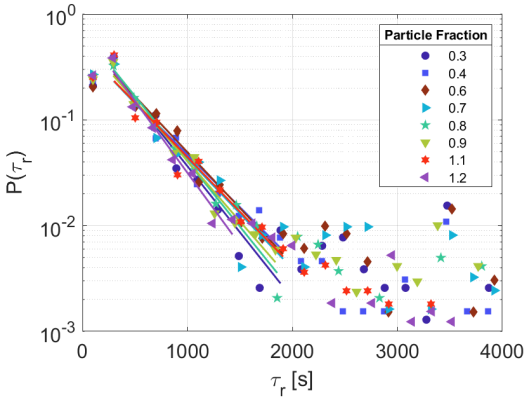

(d) Probability distributions for residence times dependent on particle fraction for template 5 at 400 mW.

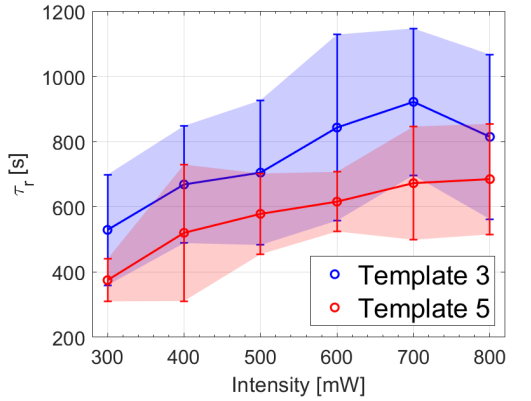

(e) Average residence times dependent on laser intensity.

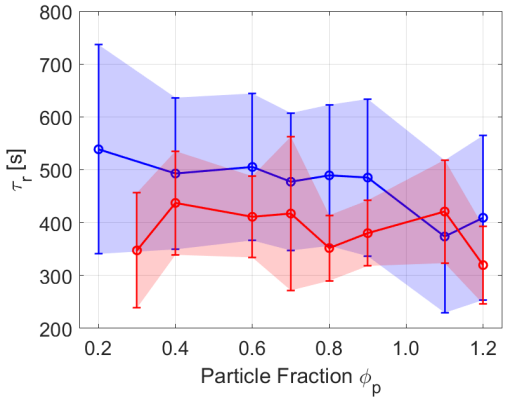

(f) Average residence times dependent on particle fraction.

Figure 4.21: Probability distributions of residence times dependent on intensity (a)-(b) and particle fraction (c)-(d). (e)-(f) Average residence times, $\tau_r = \langle \tau_r \rangle$ as estimated from exponential fit to distributions of residence times from packing coefficient.

4.2.4 Two-dimensional Probability Distribution of Particle Distances

For a less abstract view of the particles' behaviour in the light field, the 2D probability density function $P(\Delta R(\Delta t)|R_0)$ of the distances the particles moved during a time period Δt is calculated. This function is similar to the one elaborated by Su et al. [118] but has been slightly adjusted for this work. It is similarly calculated as the two-dimensional Van Hove function (see eq. (2.24)). The starting positions R_m are defined 8 s after the first registered jump in the phop-algorithm as $R_m = R_{hop}(t_m) + R_{hop}(t_m + 8\,s)$. The time shift of 8 s turned out to be a good estimate, for defining the position a particle is located in a potential minimum R_m. These can be verified by inspecting the particle trajectories, where regions of a high density of successive particle positions are an estimate for a particle being in a minimum similar to a harmonic trap (compare fig. 4.16a with fig. 3.7a).
The average is taken over all of these trajectories, starting inside of a local minimum R_m as defined above

$$P(\Delta R(\Delta t)|R_0) = \frac{1}{M}\sum_{m}^{M} P(\Delta R(\Delta t)|R_m)\ , \tag{4.6}$$

where M is the total number of particle trajectories in one measurement. To improve the statistics the average is taken over all measurements N with the same template

$$\langle P(\Delta R(\Delta t)|R_0)\rangle = \frac{1}{N}\sum_{n}^{N} P(\Delta R(\Delta t)|R_0)\ . \tag{4.7}$$

The average probability for a particle to move a distance ΔR during a time span $\Delta t = 80\,s$ can be visualised in a 2D-plot of $\langle P(\Delta R(\Delta t)|R_0)\rangle$ (fig. 4.22). A time delay of 80 s has been chosen, since it is much longer than the average time a particle needs for a jump, i. e. the longer hop times as retrieved above (fig. 4.17e–fig. 4.17f).

The overall probability is decreasing from the centre to the periphery, but not in the same way for all directions. Firstly, there is an asymmetry, which is stronger in template 3, where the probability extends until $\sim 5\,\mu m$ to the left and $\sim 3\,\mu m$ to the right. This shows a preferred motion for particles and can be indicative of drift motion probably caused by inhomogeneous intensity distribution in the light pattern. Furthermore, for template 3 the decrease shows a 10-fold orientational dependency reflecting the templates' decagonal symmetry, i. e. the probability decreases slower in 10 directions, which are equidistant 36° apart from each other. This happens for distances greater than $\sim 4\,\mu m$, which is around the same value as for the main short length in template 3 with $3.59\,\mu m$ (see table 3.2).

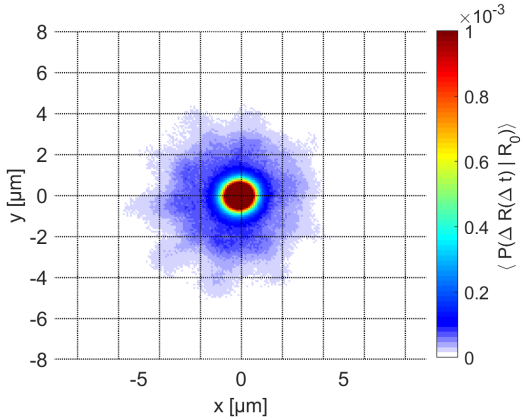

(a) Mean 2D Probability distribution of particle distances for template 3.

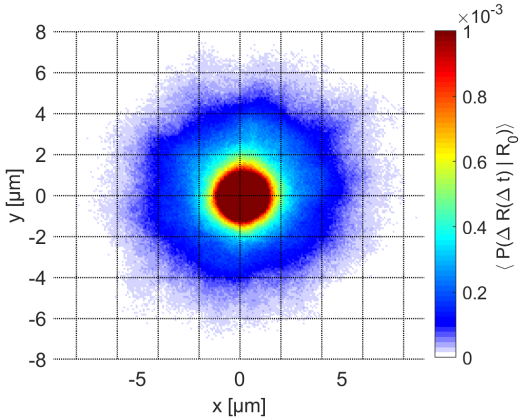

(b) Mean 2D Probability distribution of particle distances for template 5.

Figure 4.22: Averaged 2D probability density distributions for a particle to move a distance ΔR during a time span $\Delta t = 80\,s$. The distributions reflect the decagonal symmetry of the templates.

For template 5 however, the 10-fold pattern is less pronounced with diffuse edges and the probability is non-zero until distances of $\sim 7\,\mu m$ as opposed to $\sim 4\,\mu m$ in template 3. This indicates, that the particles cover a longer distance in 80 s and are not influenced by the template's 10-fold symmetry as much as in template 3. The main short distance for template 5 is $4.81\,\mu m$ and is also around the same distance $\sim 5\,\mu m$, where a direction-dependent probability is slightly indicated, but not as much as in template 3.

All in all, the 2D plots show the influence of the templates on the particles with respect to the ability to reproduce the 10-fold symmetry of the templates. It results that it is stronger in template 3 than 5.

4.2.5 Discussion on Particle Dynamics

The hop times as calculated from the jumps registered in $p_{hop}(t)$ showed a split into two regimes (see section 4.2.1). The phop-function registered small jumps as well as longer less probable ones. The different cases can be separated with exponential fits of the probability distribution into a fast and slow time regime (fig. 4.17) and can be explained with a lower probability for a particle to escape a trap than to move inside of the potential of the trap where the later events have also been registered as jumps due to the sensitivity of the chosen threshold value $p_{th} = 6$. The value was a compromise between registering particle jumps from one trap to the next one while registering as little noise as possible.
For template 3 the long hop times decreased with particle fraction. This can be explained by

higher inter-particle interactions, which become dominant over the influence of the template. The interactions are reducing the trap strength and therefore the dwell time as already shown in [119].
Short hop times however, seem not to be affected by an increased particle fraction (fig. 4.17e-fig. 4.17f). The process of particle fluctuations at this time scale is random and neither influenced by the particle fraction nor the laser intensity.
The difference between the fast and slow regimes is much lower for template 5 concerning changes in particle fraction. It can be assumed, that the particles in template 3 are occupying the positions of higher intensity and therefore of the tiling positions much more effectively than in template 5.

Considering the influence of laser intensity, the longer hop times increase with laser power, while the shorter times fluctuate around 120 s and 160 s for templates 3 and 5 respectively independent of laser power (fig. 4.17e). For template 3, the long hop times increase stronger than for longer template distances in template 5. This shows, that slow and fast jumps can be differentiated more easily for template 3, whereas for template 5, the split into the two regimes is less evident, which is similar to the trend for different particle fractions.

Comparing the jump times in between the templates, the larger template distances show shorter times as for smaller template distances independent of particle fraction and laser intensity above 300 mW. This seems counterintuitive, considering the shortest length in template 3 is 3.59 μm, while it is 4.81 μm for template 5 after table 3.2.
For a possible explanation, let's consider the confinement sizes as determined via the MSD plateau values. For template 3 they are lower on average and have a lesser variation of values. The confinement sizes as experienced by the particles are more diverse for template 5. Since the templates have at least 3 sizes of areas with high intensity and therefore higher trapping probability, the particles can theoretically be found at one of these points. For template 3, the particles seem to be predominantly found in one type of confinement. Comparing this with the longer hop times, they also seem to stay longer at these positions, indicating a high trap stiffness. Particles that reach one of these positions, which coincide with the tiling positions as seen in the structure experiments, have a higher probability to stay in the trap for most of the time of the measurement.
For template 5 the larger distances together with a greater variety of confinement sizes lead to the observed results of the particles in template 5 showing shorter hop times and that they are exploring a greater variety of traps from the template.
The residence times as retrieved from the packing coefficient confirm this. They are mostly shorter than for template 3, meaning that the confinements in template 5 are less efficient at trapping than in template 3. The particles can therefore explore more of the template with shorter dwell times.
The increase in residence times with laser intensity is due to the increase in trap strength as was the case for the long dwell times from the phop-algorithm. For higher particle fractions the trend is similar to the one for the dwell times determined from the phop-algorithm and is related to the higher inter-particle interactions at higher concentrations (see also [119]).

The trap strength and therefore the effectivity of the template to trap particles will be reduced.

Because of the similar trend for the long hop times t_l and the residence times τ_r from the packing coefficient, it can be assumed that the long-time jumps from the phop-algorithm are reflecting the jumps in between traps more closely than the short times. However, there is a discrepancy of values by a factor of two between the long hop times t_l and the residence times τ_r. The residence times are either overestimating the true dwell time in the trap and/or the long jump times are underestimating it. Both scenarios are possible since both the phop-algorithm and the packing-coefficient calculation depend on the choice of the threshold values, which can have a non-significant impact on the results.
The threshold values here were chosen according to the sizes of the traps from the MSD, which in turn are estimates of the true size of the trap, hence the possibility for deviations. Furthermore, the jump times could be determined more accurately than the residence times from the packing coefficient, where the latter showed higher uncertainties and therefore less convincing results.

There were also differences in the jump and dwell times between the two studied templates. It could be seen that for template 5 the longer times t_l did not signify full jumps from one template position to the next, but rather "smaller" more probable jumps out of one trap to a location in between the template positions. Since the tiling distances are longer in template 5, a particle needs a longer time to cover the distance to the next trap and performs smaller jumps encountering spots with different potential strengths along its path.
This is also shown in the greater range of confinement sizes encountered by the particles in template 5 since there are traps of different sizes and depths in each of the templates. The values in table 3.1 are an average of the 3 different sizes, which were defined by the boundaries of areas with high intensity. Although the rings width and intensity ratio has been adjusted for the ring sizes, the trap sizes relative to the particle diameter are nevertheless different for all six templates. (see table 3.1).

The ability of a trap to hold a particle is not only dependent on the laser intensity (strength of the potential) but also on the size of the trap boundaries d_t relative to the particle size d_p. If $d_t \leq d_p$ or $d_t >> d_p$ then the particle will be kept less well in the trap. In the first case, the particles can not discriminate well between template positions and the background if the traps are too small, so inter-particle interactions become more important. Therefore, the particles are less likely to be trapped in a template position resulting in a structure factor with less defined Bragg peaks as seen in fig. 4.6a-fig. 4.6b. In the case of $d_t >> d_p$, the trap will not be focused enough and the scattering force will dominate over the gradient force driving the particle out of the trap's centre.

The probability distribution of particle distances for one and two dimensions confirms the results from above.
First of all, the distribution of jump distances (fig. 4.18) is in accordance with the locations of the peaks in $g(r)$ (fig. 4.12). Maxima in the PDF appear around similar values as in $g(r)$ and coincide with the main short and long distances in the tiling (table 3.2). While the

PDF for template 3 showed more pronounced maxima at discrete positions, for template 5 there was also a plateau starting at distances smaller than the shortest template distance (fig. 4.18). This tells us that the particles are also located in between the template positions. This is also supported by the probability distributions in 2D (fig. 4.22b), which show more diffuse edges and a greater range of distances in the same time interval as template 3. In contrast template 3 showed a more defined 10-fold symmetry in the 2D PDF (fig. 4.22a). It indicates that the particles are more able to reproduce the 10-fold pattern of template 3 than of template 5.

4.3 Experiments with the Spatial Light Modulator

In this section, the experiments conducted with the SLM will be presented briefly and discussed. The aim was to create quasicrystals with feedback programming as described in section 3.4. One of these experiments showed an unexpected result, which indicated 12-fold quasicrystals at first. But this turned out to be a misinterpretation, showing another interesting phenomenon in crystal formation instead.

4.3.1 Self-Assembly of Hexagonal Colloidal Crystals

Stable crystalline structures with 6- or 4-fold rotational symmetries could be formed from colloids in holographic optical fields. A magnification of 60 x together with particle diameters of 2.8 μm and 2.1 μm were used, to create hexagonal structures through self-assembly from feedback programming. An adaptive potential field is formed locally at the current particle position as described in section 3.4. If a Gaussian ring-shaped intensity profile is used, the formation of clusters with 6-fold rotational symmetry is facilitated (see fig. 4.26). The overlapping of the Gaussian rings leads to intensity maxima on spots, where the particles are to be expected in a hexagonal pattern. Due to entropic reasons, the 6-fold crystal is the most stable structure in 2D for hard spheres.
A square lattice with 4-fold symmetry can be induced with double-Gaussian rings with a radius ratio of $r_2/r_1 \approx 1.4$. However, since the smaller ring still enables the formation of a hexagonal pattern, it is more difficult to achieve a 4-fold symmetry. The square lattice needs to compete with the more dominant 6-fold symmetry. Therefore, hexagonal crystal structure is not completely suppressed forming in some regions, which hampers the formation of pure 4-fold symmetry.

As can be seen in fig. 4.23 clusters with hexagonal symmetry are forming with a Gaussian-ring intensity profile. By increasing the radius, the lattice spacing increases accordingly.

4.3.2 Crystal Twinning

When analysing the structure in Fourier space, one has to be careful when studying the rotational symmetries. A 12-fold quasicrystal can in principle be confused with another phenomenon in crystallography called crystal twinning. Here, two crystals with the same composition and lattice structure can intergrow in a way, that their lattice is rotated with respect to each other. This phenomenon can also be seen in nature for certain minerals. Crystal twinning can lead to the finding of a mistakenly higher symmetric order of the

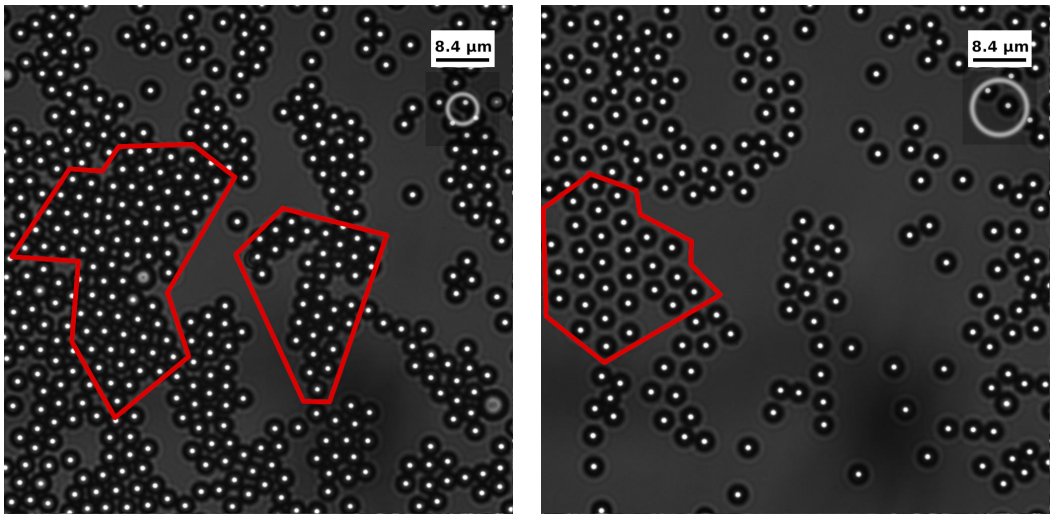

(a) Hexagonal clusters with lattice spacing $\sim d_p$.

(b) Hexagonal clusters with wide lattice spacing $1.9\,d_p$.

Figure 4.23: Hexagonal clusters with different lattice spacing from feedback-programming. The particles' local intensity profile used here is depicted in each upper right corner. Particularly ordered areas are bordered red.

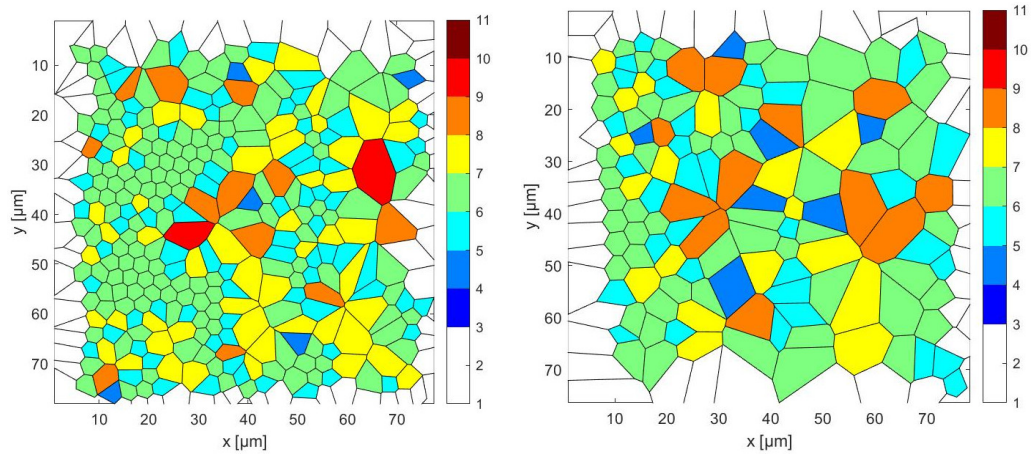

(a) Hexagonal clusters with lattice spacing $\sim d_p$.

(b) Hexagonal clusters with wide lattice spacing $1.9\,d_p$.

Figure 4.24: Voronoi diagrams of hexagonal clusters with different lattice spacing from SLM-feedback-programming (fig. 4.23). Voronoi cells with 6 edges are coloured green. Areas with 6-fold symmetry can be easily seen by eye. The hexagons on the left are slightly smaller indicative of shorter inter-particle distances.

sample than for each crystal alone. That's why the diffraction pattern of two hexagonal crystals rotated about 30° against each other will show 12 peaks like in the structure factor

of a 12-fold quasicrystalline structure, since each hexagonal area contributes 6 peaks, while one is rotated against the other so that all 12 peaks are separated equidistantly for one length scale.

This was the case for two hexagonal regions in an otherwise amorphous structure, which formed during a measurement with high particle concentration (fig. 4.25a). The Fourier space shows 12 pronounced peaks (fig. 4.25b), although no corresponding quasicrystalline pattern can be found in real space. Instead, two large regions with 6-fold symmetry have formed, which are rotated about 30° against each other. Hence the structure factor shows the overlap of two 6-fold diffraction patterns rotated about the same angle of 30° as the structures in real space.

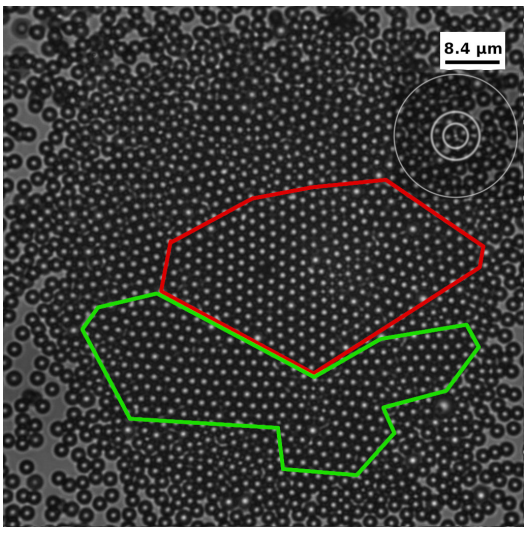

(a) Screenshot of a sample with hexagonal twins. The particles' local intensity profile used here is depicted upper right corner.

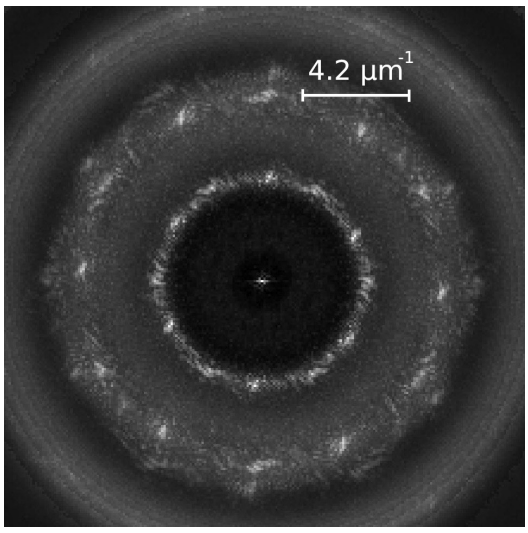

(b) Structure factor of the sample with hexagonal twins. 12 Bragg peaks can be seen similar to a 12-fold symmetry.

Figure 4.25: Hexagonal twins as neighbouring hexagonal areas (twin boundaries in green and red), whose orientation is about 30° rotated against each other.

Crystal twinning has also a place in the history of quasicrystal discovery. It was a hypothesis to explain the diffraction patterns of aluminium-manganese alloys (Al_6Mn) discovered in 1986 by Shechtman et al. Linus Pauling was one of the first to oppose the idea of a newfound structure and explained the "forbidden" symmetry with crystal twinning [120]. Instead, it became evident, that the structure was not composed of twins because it was not possible to match a Bravais lattice in the x-ray diffraction pattern. The pattern of the quasicrystal found by Shechtman et al. showed no row of periodically spaced spots in any direction, but a long-range positional and orientational order [36]. This eliminated the hypothesis of the structure resulting from multiple twins of periodic crystals. Nevertheless, it is indeed possible for quasicrystals to form from twinning at the unit-cell level as has been shown by Prodan et al. [121].

4.3.3 Clusters with Quasicrystalline Building Blocks

For quasicrystal formation, the interaction potential has to be adjusted to support two length scales like those found in the Barkan-Diamant-Lifshitz Model (BDL) [63], for minimising the free energy of the system (section 2.3.1) . E. g. double Gaussian rings were used with an adequate ratio between the two radii, which can be tuned. However, when using interaction potentials like proposed in previous simulations [48],[122], no large regions with quasicrystalline structures were found in this system, which stayed stable during one measurement of about 10 min. Instead, small clusters did appear, that consisted of a mixture of square-triangle-tilings from different symmetries in each cluster. E. g. for an intensity profile mimicking a modified exponential potential [123], so-called sigma structures were found locally and hexagonal as well as square tilings did form, but no overall 12-fold symmetry was found (fig. 4.26). The clusters were too small and too wide apart from each other to merge into a greater structure and contribute significantly to the diffraction pattern.

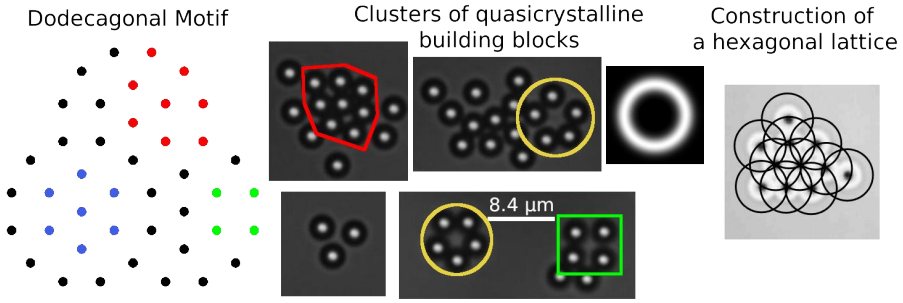

Figure 4.26: On the left, a dodecagonal motif after [124] is shown with coloured sigma tile (red), hexagon (green) and square (blue). In the middle part, clusters with a local sigma structure, pentagons, squares and triangles formed with a local ring-shaped intensity profile as depicted. On the right, is a visual explanation for the formation of a hexagonal lattice from Gaussian rings.

For a different approach to growing quasicrystals with as few defects as possible, templates with traps at fixed positions for a desired quasicrystalline symmetry have been used. E. g. for the dodecagonal symmetry a motif by van der Linden et al. (as seen in fig. 4.26) has been used [124].
Nevertheless, this approach did not lead to a successful formation of quasicrystals. The particles were rather found in the periphery of the image than in its centre since they got repelled by the zeroth diffraction order of the SLM. Using a dodecagonal frame template as a chain of a repeating 12-fold pattern did not improve the self-assembly process into a desired quasicrystalline structure.
The comparatively low resolution of the SLM with 1024 x 768 pixels could have additionally limited the ability to form more complex lattices. It remains to be proven if an SLM with higher resolution will show the desired results.

5 Conclusion

To sum up this work, it has been shown, that a Digital Micromirror Device can be implemented in a setup for multiple optical tweezers. User-defined light fields can be generated directly without the need for calculation of holograms as with the Spatial Light Modulator in Holographic Optical Tweezers and with a higher resolution (1920 x 1080 pixels).

This has been implemented in experiments with spherical PS particles in DMD-projected light fields with 10-fold rotational symmetry. The patterns were created by overlaying double rings on positions of "Tuebingen" tilings, at six different tiling distances.

The particles' behaviour was influenced by the light field, which resulted in a detectable 10-fold symmetry in the structure factor of the particle arrangements as prescribed by the templates. The six different tiling distances in the templates showed significant differences in the intensity of the structure factors' Bragg peaks.
Under different laser intensity and particle concentration, the particles form structures, which show a stronger or weaker 10-fold order in the diffraction pattern. For larger template distances the structure factor also showed a lower 10-fold signal, which is related to the lower ability to trap particles at the tiling positions. Only those particles, which are located at positions producing constructive interference for specific wave vectors, will contribute to a Bragg peak and define the rotational symmetry of the structure.

The templates' short and main length was also reflected in the radial distributions of the particle arrangements. While the first most pronounced peak stems from the closest distance between two particles modelled as hard spheres ($\sim d_p$), the second to fourth peak could be related to the main length scales of the template tilings.

The in-depth study of particle trajectories showed that there are two diffusive regimes, i. e. a slow regime, resulting from local particle jumps in between the tiling positions, as well as a fast regime, representative of the fluctuations inside of the potential minima. It has been obtained, that higher intensity contributes to a higher trap stiffness at the tiling positions so that the time between jumps increases. The movement inside a trap is neither affected by the increase in intensity nor by an increase in particle fraction. For template 3 the dwell times are slightly decreasing until the highest measured particle fractions of 1.2, indicative of dominating interactions between the particles themselves. However, for template 5, the longer times show an oscillating behaviour, where the mean is closer to the mean of short

times than for template 3. This implies that there is no clear separation of the two jump-time regimes in template 5. Hence template 3 has a higher impact on the behaviour of the particles than template 5, which is also confirmed by the more constant value of confinement sizes retrieved from MSD plateaus of particles in template 3.
Additionally, by analysing the packing coefficient as elaborated by Renner et. al [115], the residence time in a confined area could be retrieved from the compactness of trajectories. It showed, that the particles in template 3 were longer confined or trapped in contrast to particles in template 5.
This is following the results of the 2D probability distributions of particle locations, which reflected the decagonal symmetry of the templates as has been similarly shown by Su et al. of particles diffusing over decagonal substrates [118].

It could be shown, that the long times as retrieved from the phop-algorithm show the same dependency on laser intensity and particle fraction compared to the residence times as determined from the packing fraction. The values of the residence times were however about two times higher than from the phop algorithm, showing that the particle jumps are underestimating the dwell time in a trap. Furthermore, longer template distances, i. e. in template 5, led to shorter dwell times from phop as well as from the packing coefficient in contrast to the shorter distances in template 3. This seems counterintuitive at first, but the registered jumps in template 5 stem from particles, which are covering distances in one jump that are shorter than the tiling distances in the template. This can be also seen in the high probability for particles to jump a length, which is smaller than the template distances. The distances in template 3 are shorter and therefore more likely to be covered by a single particle jump, whereas the long times for template 5 stem from jumps to weaker traps in between the template positions. This could be also seen from the wide range of confinement sizes in template 5. The MSD plateau values of confined particles for estimating the confinement sizes are in accordance with the difference in trap sizes between templates 3 and 5. Finally, the distribution of jump distances in two dimensions also verifies, that the symmetry of template 3 is recreated more accurately by the particles than for template 5.

The work in this project can be continued further in many ways. For one the study of the particle trajectories can be analysed with other methods than the phop-algorithm and packing coefficient presented here. E. g. the diffusion can be studied in more detail for confined motion and the motion outside of a trapped state.
Furthermore, the study of particle dynamics can be continued by studying more tiling distances than the two measured here. Finally, the particle arrangements and dynamics can be examined for symmetries other than 10-fold.

The experiments with the holographic optical tweezers can also be resumed. It is possible, that the arranging of particles into quasicrystalline structures without a template can be achieved as already seen for hexagonal lattices in the SLM setup. The self-assembly of spherical particles with feedback programming via laser-optical fields would be a remarkable achievement for the future. The limits of this technique could be tested for various

structures and adaptive light field potentials and additional memory effects could be programmed too.
The feedback algorithm can be also further developed into programming orientational-dependent intensity profiles, thus mimicking patchy particles or different intensity profiles for separate subgroups of tracked particles, i. e. creating binary systems.

References

[1] Christoph Zunke. "Driven and Obstructed Colloids in Random Energy Landscapes". PhD thesis. Heinrich-Heine-Universität Düsseldorf, Oct. 2017.

[2] Mher Ghulinyan. "One-dimensional photonic quasicrystals". In: *Light Localisation and Lasing: Random and Quasi-random Photonic Structures*. Ed. by Mher Ghulinyan and LorenzoEditors Pavesi. Cambridge University Press, 2014, pp. 99–129. DOI: 10.1017/CBO9781139839501.006.

[3] Vinothan N. Manoharan. "Colloidal matter: Packing, geometry, and entropy". In: *Science* 349.6251 (2015). ISSN: 0036-8075. DOI: 10.1126/science.1253751.

[4] Fan Li, David P. Josephson, and Andreas Stein. "Colloidal Assembly: The Road from Particles to Colloidal Molecules and Crystals". In: *Angewandte Chemie International Edition* 50.2 (2011), pp. 360–388. DOI: 10.1002/anie.201001451.

[5] Michael Schmiedeberg and Holger Stark. "Colloidal ordering on a 2D quasicrystalline substrate". In: *Phys. Rev. Lett.* (2008). ISSN: 00319007. DOI: 10.1103/PhysRevLett.101.218302.

[6] *Dynamische Atom-Molekül-Wissenschafts-Symbolvektorikone*. URL: https://de.vecteezy.com/vektorkunst/550979-dynamische-atom-molekul-wissenschafts-symbolvektorikone (visited on 02/23/2022).

[7] *Vektor-DNA-Symbol*. URL: https://de.vecteezy.com/vektorkunst/420730-vektor-dna-symbol (visited on 02/23/2022).

[8] *Sulfat-Latex-Beads, 8 % w/v, 1 µm*. URL: https://www.thermofisher.com/order/catalog/product/S37498?SID=srch-srp-S37498#/S37498?SID=srch-srp-S37498 (visited on 04/27/2020).

[9] Zhan Wei Li et al. "A versatile model for soft patchy particles with various patch arrangements". In: *Soft Matter* 12.3 (2016), pp. 741–749. ISSN: 17446848. DOI: 10.1039/c5sm02125a.

[10] Stefano Sacanna and David J. Pine. "Shape-anisotropic colloids: Building blocks for complex assemblies". In: *Current Opinion in Colloid Interface Science* 16.2 (2011), pp. 96–105. ISSN: 1359-0294. DOI: https://doi.org/10.1016/j.cocis.2011.01.003.

[11] Emanuela Bianchi, Ronald Blaak, and Christos N. Likos. "Patchy colloids: state of the art and perspectives". In: *Phys. Chem. Chem. Phys.* 13 (14 2011), pp. 6397–6410. DOI: 10.1039/C0CP02296A.

[12] "Introduction". In: *Introduction to Soft Matter*. John Wiley Sons, Ltd, 2007. Chap. 1, pp. 1–37. ISBN: 9780470517338. DOI: 10.1002/9780470517338.ch1.

[13] C. Patrick Royall, Wilson C. K. Poon, and Eric R. Weeks. "In search of colloidal hard spheres". In: *Soft Matter* 9 (1 2013), pp. 17–27. DOI: 10.1039/C2SM26245B.

[14] *DLVO*. URL: https://www.sciencedirect.com/topics/pharmacology-toxicology-and-pharmaceutical-science/dlvo-theory (visited on 04/27/2020).

[15] M. A. Rutgers et al. "Measurement of the hard-sphere equation of state using screened charged polystyrene colloids". In: *Phys. Rev. B* 53 (9 Mar. 1996), pp. 5043–5046. DOI: 10.1103/PhysRevB.53.5043.

[16] *Latex Bead Technical Overview*. URL: https://www.thermofisher.com/de/de/home/life-science/cell-analysis/qdots-microspheres-nanospheres/idc-surfactant-free-latex-beads/latex-bead-technical-overview.html (visited on 04/27/2020).

[17] Peter Pusey and W. Megen. "Phase Behavior of Concentrated Suspensions of Nearly Hard Colloidal Spheres". In: *Nature* 320 (Mar. 1986), pp. 340–342. DOI: 10.1038/320340a0.

[18] John Desmond Bernal and J Mason. "Packing of Spheres: Co-ordination of Randomly Packed Spheres". In: *Nature* 188 (1960), pp. 910–911.

[19] Thomas C. Hales. "The Sphere Packing Problem". In: *J. Comput. Appl. Math.* 44.1 (Dec. 1992), pp. 41–76. ISSN: 0377-0427. DOI: 10.1016/0377-0427(92)90052-Y.

[20] Francesco Arceri et al. *Glasses and aging: A Statistical Mechanics Perspective*. 2020. arXiv: 2006.09725 [cond-mat.stat-mech].

[21] Tomonari Dotera. *Quasicrystals in soft matter*. 2011. DOI: 10.1002/ijch.201100146.

[22] M.S. Silberberg. *Principles of General Chemistry*. McGraw-Hill Higher Education, 2013. ISBN: 9780077762063.

[23] Hajime Tanaka. "Bond orientational ordering in liquids: Towards a unified description of water-like anomalies, liquid-liquid transition, glass transition, and crystallization Bond orientational ordering in liquids". In: *Eur. Phys. J. E* (2012). ISSN: 12928941. DOI: 10.1140/epje/i2012-12113-y.

[24] Hajime Tanaka. "Importance of many-body orientational correlations in the physical description of liquids". In: *Faraday Discuss.* 167 (0 2013), pp. 9–76. DOI: 10.1039/C3FD00110E.

[25] Wolfgang H. Meyer. "Polymer physics. by Ulf W. Gedde, Chapman & Hall, London 1995, x, 298 pp., softcover, £69.00, ISBN 0-412-62640-3". In: *Advanced Materials* 8.10 (1996), pp. 863–864. DOI: https://doi.org/10.1002/adma.19960081026.

[26] Gyula I. Tóth and László Gránásy. "Crystal Nucleation in the Hard-Sphere System Revisited: A Critical Test of Theoretical Approaches". In: *The Journal of Physical Chemistry B* 113.15 (2009). PMID: 19320450, pp. 5141–5148. DOI: 10.1021/jp8097439.

[27] A. Escobar et al. "Direct observation of crystal nucleation and growth in a quasi-two-dimensional nonvibrating granular system". In: *Phys. Rev. E* 104 (4 Oct. 2021), p. 044904. DOI: 10.1103/PhysRevE.104.044904.

[28] A. Ashkin. "Acceleration and Trapping of Particles by Radiation Pressure". In: *Phys. Rev. Lett.* 24.4 (1970), pp. 156–159. ISSN: 00319007. DOI: 10.1103/PhysRevLett.24.156.

[29] A. Ashkin et al. "Observation of a single-beam gradient force optical trap for dielectric particles". In: *Opt. Lett.* 11.5 (May 1986), pp. 288–290. DOI: 10.1364/OL.11.000288.

[30] A. M. Kaufman, B. J. Lester, and C. A. Regal. "Cooling a Single Atom in an Optical Tweezer to Its Quantum Ground State". In: *Phys. Rev. X* 2 (4 Nov. 2012), p. 041014. DOI: 10.1103/PhysRevX.2.041014.

[31] Keir C. Neuman and Steven M. Block. "Optical trapping". In: *Rev. Sci. Instrum.* 75.9 (2004), pp. 2787–2809. ISSN: 00346748. DOI: 10.1063/1.1785844. arXiv: arXiv:1011.1669v3. URL: http://aip.scitation.org/doi/10.1063/1.1785844.

[32] A. Ashkin. "Forces of a single-beam gradient laser trap on a dielectric sphere in the ray optics regime". In: *Biophysical Journal* 61.2 (1992), pp. 569–582. ISSN: 0006-3495. DOI: https://doi.org/10.1016/S0006-3495(92)81860-X.

[33] M.J. Padgett, J. Molloy, and D. McGloin. *Optical Tweezers: Methods and Applications*. Series in Optics and Optoelectronics. CRC Press, 2010. ISBN: 9781420074147.

[34] P. C. Chaumet and M. Nieto-Vesperinas. "Time-averaged total force on a dipolar sphere in an electromagnetic field". In: *Opt. Lett.* 25.15 (Aug. 2000), pp. 1065–1067. DOI: 10.1364/OL.25.001065.

[35] Walter Steurer and Sofia Deloudi. "Fascinating quasicrystals". In: *Acta Crystallogr. Sect. A Found. Crystallogr.* 64.1 (2008), pp. 1–11. ISSN: 16005724. DOI: 10.1107/S0108767307038627.

[36] D. Shechtman et al. "Metallic phase with long-range orientational order and no translational symmetry". In: *Phys. Rev. Lett.* (1984). ISSN: 00319007. DOI: 10.1103/PhysRevLett.53.1951.

[37] K.F. Kelton and P.C. Gibbons. "Hydrogen Storage in Quasicrystals". In: *MRS Bulletin* 22.11 (1997), pp. 69–72. DOI: 10.1557/S0883769400034473.

[38] Enrique Macia. *Quasicrystals: Fundamentals and Applications*. Dec. 2020.

[39] Xiangbing Zeng et al. "Supramolecular dendritic liquid quasicrystals". In: *Nature* 428.6979 (Mar. 2004), pp. 157–160. DOI: 10.1038/nature02368.

[40] Walter R. C. Somerville et al. “Pattern formation in two-dimensional hard-core/soft-shell systems with variable soft shell profiles”. In: (2020), pp. 1–12.

[41] M. Baake et al. “The Triangle Pattern — A new Quasiperiodic Tiling with Fivefold Symmetry”. In: *Modern Physics Letters B* 04.04 (1990), pp. 249–258. DOI: 10.1142/S0217984990000313.

[42] Michael Engel and Hans Rainer Trebin. “Structural complexity in monodisperse systems of isotropic particles”. In: *Zeitschrift fur Krist.* 2008. ISBN: 0044-2968. DOI: 10.1524/zkri.2008.1040. arXiv: 0807.0875.

[43] L. Q.Costa Campos and S. W.S. Apolinario. “Structural orderings of anisotropically confined colloids interacting via a quasi-square-well potential”. In: *Phys. Rev. E - Stat. Nonlinear, Soft Matter Phys.* (2015). ISSN: 15502376. DOI: 10.1103/PhysRevE.91.012305. arXiv: arXiv:1011.1669v3.

[44] Anna Skibinsky et al. *Quasicrystals in a monodisperse system.* Tech. rep. 1999.

[45] Hans-Rainer Trebin et al. *Simulating structure and physical properties of complex metallic alloys.* Tech. rep. 2007.

[46] Michael Engel and Hans Rainer Trebin. “Self-assembly of monatomic complex crystals and quasicrystals with a double-well interaction potential”. In: *Phys. Rev. Lett.* (2007). ISSN: 00319007. DOI: 10.1103/PhysRevLett.98.225505. arXiv: 0705.0213.

[47] Alexander Gabriëlse, Hartmut Löwen, and Frank Smallenburg. “Low-temperature crystal structures of the hard core square shoulder model”. In: *Materials (Basel).* (2017). ISSN: 19961944. DOI: 10.3390/ma10111280.

[48] Anja Gemeinhardt, Miriam Martinsons, and Michael Schmiedeberg. “Growth of two-dimensional dodecagonal colloidal quasicrystals: Particles with isotropic pair interactions with two length scales vs. patchy colloids with preferred binding angles”. In: *Eur. Phys. J. E* (2018). ISSN: 1292-8941. DOI: 10.1140/epje/i2018-11737-1.

[49] T. Dotera, T. Oshiro, and P. Ziherl. “Mosaic two-lengthscale quasicrystals, Supplementary”. In: *Nature* (2014). ISSN: 00280836. DOI: 10.1038/nature12938.

[50] Samuel Savitz, Mehrtash Babadi, and Ron Lifshitz. “Multiple-scale structures: from Faraday waves to soft-matter quasicrystals”. In: *IUCrJ* 5.3 (May 2018), pp. 247–268. DOI: 10.1107/S2052252518001161. URL: https://doi.org/10.1107/S2052252518001161.

[51] Ron Lifshitz. *The Definition of Quasicrystals.* Tech. rep.

[52] C. V. Achim, M. Schmiedeberg, and H. Löwen. “Growth modes of quasicrystals”. In: *Phys. Rev. Lett.* (2014). ISSN: 10797114. DOI: 10.1103/PhysRevLett.112.255501. arXiv: 1405.5434.

[53] Hem Raj Sharma. “Structure, Morphology, and Dynamics of Quasicrystal Surfaces”. PhD thesis. 2002. URL: http://dx.doi.org/10.17169/refubium-13587.

[54] C Richard et al. “Random tilings: concepts and examples”. In: *Journal of Physics A: Mathematical and General* 31.30 (July 1998), pp. 6385–6408. DOI: 10.1088/0305-4470/31/30/007.

[55] Michael J. Solomon. “Tools and Functions of Reconfigurable Colloidal Assembly”. In: *Langmuir* 34.38 (2018), pp. 11205–11219. ISSN: 15205827. DOI: 10.1021/acs.langmuir.7b03748.

[56] Christopher L. Henley. “Random Tiling Models”. In: *Quasicrystals*, pp. 429–524. DOI: 10.1142/9789814503532_0015.

[57] Katherine J. Strandburg. “Quasicrystals and Aperiodic Tilings”. In: *Computers in Physics* 5.5 (1991), pp. 520–528. DOI: 10.1063/1.4823015.

[58] Ron Lifshitz and Dean M. Petrich. “Theoretical Model for Faraday Waves with Multiple-Frequency Forcing”. In: *Phys. Rev. Lett.* 79 (7 Aug. 1997), pp. 1261–1264. DOI: 10.1103/PhysRevLett.79.1261.

[59] J. Swift and P. C. Hohenberg. “Hydrodynamic fluctuations at the convective instability”. In: *Phys. Rev. A* 15 (1 Jan. 1977), pp. 319–328. DOI: 10.1103/PhysRevA.15.319.

[60] Kobi Barkan and Beverly Sackler. “Stability of Soft Quasicrystals Composed of Isotropic Particles”. In: 2.September (2009), pp. 1–5. arXiv: arXiv:1005.5257v2.

[61] P. C. Hohenberg and B. I. Halperin. “Theory of dynamic critical phenomena”. In: *Rev. Mod. Phys.* 49 (3 July 1977), pp. 435–479. DOI: 10.1103/RevModPhys.49.435.

[62] Kai Jiang et al. “Stability of two-dimensional soft quasicrystals in systems with two length scales”. In: *Phys. Rev. E* 92 (4 Oct. 2015), p. 042159. DOI: 10.1103/PhysRevE.92.042159. URL: https://link.aps.org/doi/10.1103/PhysRevE.92.042159.

[63] Kobi Barkan, Haim Diamant, and Ron Lifshitz. “Stability of quasicrystals composed of soft isotropic particles”. In: *Phys. Rev. B* 83 (17 May 2011), p. 172201. DOI: 10.1103/PhysRevB.83.172201.

[64] Michael Engel et al. “Dynamics of particle flips in two-dimensional quasicrystals”. In: *Phys. Rev. B - Condens. Matter Mater. Phys.* (2010). ISSN: 10980121. DOI: 10.1103/PhysRevB.82.134206. arXiv: 1006.1836.

[65] Miriam Martinsons and Michael Schmiedeberg. “Stability of particles in two-dimensional quasicrystals against phasonic perturbations”. In: (2019). arXiv: 1905.10152. URL: http://arxiv.org/abs/1905.10152.

[66] M. Schmiedeberg et al. “Dislocation-free growth of quasicrystals from two seeds due to additional phasonic degrees of freedom”. In: *Phys. Rev. E* (2017). ISSN: 24700053. DOI: 10.1103/PhysRevE.96.012602.

[67] Keisuke Nagao et al. “Experimental Observation of Quasicrystal Growth”. In: *Phys. Rev. Lett.* 115 (7 Aug. 2015), p. 075501. DOI: 10.1103/PhysRevLett.115.075501.

[68] Marc de Boissieu. “Phonons, phasons and atomic dynamics in quasicrystals”. In: *Chem. Soc. Rev.* 41 (20 2012), pp. 6778–6786. DOI: 10.1039/C2CS35212E.

[69] F. Reif. *Fundamentals of Statistical and Thermal Physics*. McGraw-Hill, 1985. Chap. 1, 12.5.

[70] S. Chandrasekhar. "Brownian Motion, Dynamical Friction and Stellar Dynamics". In: *Dialectica* 3.1-2 (1949), pp. 114–126. DOI: 10.1111/j.1746-8361.1949.tb00859.x.

[71] Lennart Sjögren. *Lecture notes Stochastic processes*.

[72] Léon Van Hove. "Correlations in Space and Time and Born Approximation Scattering in Systems of Interacting Particles". In: *Phys. Rev.* 95 (1 July 1954), pp. 249–262. DOI: 10.1103/PhysRev.95.249. URL: https://link.aps.org/doi/10.1103/PhysRev.95.249.

[73] Paul Hopkins et al. "The van Hove distribution function for brownian hard spheres: dynamical test particle theory and computer simulations for bulk dynamics." In: *The Journal of chemical physics* 133 22 (2010).

[74] Jean-Pierre Hansen I.R. McDonald. *Theory of Simple Liquids*. Academic Press, 2013.

[75] Zahra Ghannad. "Fickian yet non-Gaussian diffusion in two-dimensional Yukawa liquids". In: *Phys. Rev. E* 100 (3 Sept. 2019), p. 033211. DOI: 10.1103/PhysRevE.100.033211.

[76] Mario et.al. Heidernätsch. "Characterizing N-dimensional anisotropic Brownian motion by the distribution of diffusivities". In: (). DOI: 10.1063/1.4828860.

[77] P. H. Westfall and K. S. S. Henning. *Understanding Advanced Statistical Methods*. CRC Press, 2013.

[78] Michael J. Saxton and Ken Jacobson. "SINGLE-PARTICLE TRACKING:Applications to Membrane Dynamics". In: *Annual Review of Biophysics and Biomolecular Structure* 26.1 (1997). PMID: 9241424, pp. 373–399. DOI: 10.1146/annurev.biophys.26.1.373.

[79] N. Destainville and L. Salome. "Quantification and Correction of Systematic Errors Due to Detector Time-Averaging in Single-Molecule Tracking Experiments". In: *Biophysical Journal* 90.2 (Jan. 2006), pp. L17–L19. DOI: 10.1529/biophysj.105.075176. arXiv: q-bio/0601010 [q-bio.QM].

[80] G. E. Uhlenbeck and L. S. Ornstein. "On the Theory of the Brownian Motion". In: *Phys. Rev.* 36 (5 Sept. 1930), pp. 823–841. DOI: 10.1103/PhysRev.36.823.

[81] Texas Instruments. *Using Lasers with DLP® DMD technology*. English. Version TI DN 2509927. Texas Instruments. 2008. 9 pp. URL: https://www.ti.com/pdfs/dlpdmd/Using_Lasers_with_DLP(r)_Technology.pdf.

[82] Kevin Cowtan. "Phase Problem in X-ray Crystallography, and Its Solution". In: *eLS*. John Wiley Sons, Ltd, 2003. ISBN: 9780470015902. DOI: https://doi.org/10.1038/npg.els.0002722.

[83] Martín Martínez-Ripoll. *Scattering and diffraction. The structure factor*. URL: https://www.xtal.iqfr.csic.es/Cristalografia/parte_05_7-en.html (visited on 02/22/2022).

[84] Joonas Herranen et al. “Non-spherical particles in optical tweezers: A numerical solution”. In: *PLoS ONE* 14 (2019).

[85] Nidhi Raval et al. “Chapter 10 - Importance of Physicochemical Characterization of Nanoparticles in Pharmaceutical Product Development”. In: *Basic Fundamentals of Drug Delivery*. Ed. by Rakesh K. Tekade. Advances in Pharmaceutical Product Development and Research. Academic Press, 2019, pp. 369–400. ISBN: 978-0-12-817909-3. DOI: https://doi.org/10.1016/B978-0-12-817909-3.00010-8.

[86] Coverslip Correction. *Understanding Spatial Filters*. 2020. URL: https://www.microscopyu.com/microscopy-basics/coverslip-correction (visited on 11/11/2020).

[87] Texas Instruments. *DLP6500 0.65 1080p MVSP S600 DMD*. English. Version DLPS053B. Texas Instruments. 2014. 54 pp. URL: https://www.ti.com/pdfs/dlpdmd/Using_Lasers_with_DLP(r)_Technology.pdf.

[88] David M. Benton. “Multiple beam steering using dynamic zone plates on a micromirror array”. In: *Optical Engineering* 57.7 (2018), pp. 1–7. DOI: 10.1117/1.OE.57.7.073109.

[89] Jinpeng Liu et al. “Optimal micro-mirror tilt angle and sync mark design for digital micro-mirror device based collinear holographic data storage system”. In: *Appl. Opt.* 56.16 (June 2017), pp. 4779–4784. DOI: 10.1364/AO.56.004779.

[90] Alice Sandmeyer et al. “DMD-based super-resolution structured illumination microscopy visualizes live cell dynamics at high speed and low cost”. In: *bioRxiv* (2019), p. 797670. DOI: 10.1101/797670.

[91] *N-BK7 Plano-Convex Lenses - Graphs*. URL: https://www.thorlabs.com/newgrouppage9.cfm?objectgroup_id=112 (visited on 04/01/2022).

[92] *Understanding Spatial Filters*. 2018. URL: https://www.edmundoptics.de/knowledge-center/application-notes/lasers/understanding-spatial-filters/ (visited on 11/05/2020).

[93] Mike Woerdemann et al. “Advanced optical trapping by complex beam shaping”. In: *Laser Photonics Rev.* 7.6 (2013), pp. 839–854. ISSN: 18638880. DOI: 10.1002/lpor.201200058.

[94] Ravi Radhakrishnan and Bernhardt L. Trout. *Order parameters in molecular simulations*. Ed. by Sidney Yip. Kluwer Academic Publishers, 2005. ISBN: 9783642073960.

[95] R. W. Gerchberg. “A practical algorithm for the determination of phase from image and diffraction plane pictures”. In: *Optik* 35 (1972), pp. 237–246.

[96] James Fienup. “Phase retrieval algorithms: a comparison”. In: *Applied optics* 21 (Aug. 1982), pp. 2758–69. DOI: 10.1364/AO.21.002758.

[97] *Phase retrieval*. 2007. URL: https://en.wikipedia.org/wiki/Phase_retrieval#/media/File:GS-diagram.png (visited on 02/22/2022).

[98] Christina Hesseling et al. “Controlling ghost traps in holographic optical tweezers.” In: *Opt. Lett.* 36.18 (2011), pp. 3657–9. ISSN: 1539-4794. DOI: 10.1364/OL.36.003657.

[99] M. Martinsons and M. Schmiedeberg. “Growth of two-dimensional decagonal colloidal quasicrystals”. In: *J. Phys. Condens. Matter* (2018). ISSN: 1361648X. DOI: 10.1088/1361-648X/aac503.

[100] Michael Schmiedeberg. “Colloidal particles on quasicrystalline substrates”. PhD thesis. Technischen Universit at Berlin, 2008.

[101] Jules Mikhael. *Colloidal Monolayers on Quasiperiodic Laser Fields*. Tech. rep.

[102] Jian-Hui Chen, Cheng Cai, and Xiu-Jun Fu. “Decagonal and Dodecagonal Quasicrystals Obtained by Molecular Dynamics Simulations*”. In: *Chinese Physics Letters* 36.3, 036101 (Mar. 2019), p. 036101. DOI: 10.1088/0256-307X/36/3/036101.

[103] Gary Meisner. *Number Five (5) and Phi*. 2012. URL: https://www.goldennumber.net/five-phi/ (visited on 02/22/2022).

[104] G.R. Fowles. *Introduction to Modern Optics*. Dover Books on Physics Series. Dover Publications, 1989. ISBN: 9780486659572. URL: https://books.google.de/books?id=SL1n9TuJ5YMC.

[105] W. Steurer. “Five-dimensional Patterson analysis of the decagonal phase of the system Al-Mn”. In: *Acta Crystallographica Section B* 45.6 (Dec. 1989), pp. 534–542. DOI: 10.1107/S0108768189007998.

[106] A. Yamamoto and K. N. Ishihara. “Penrose patterns and related structures. II. Decagonal quasicrystals”. In: *Acta Crystallographica Section A* 44.5 (Sept. 1988), pp. 707–714. DOI: 10.1107/S010876738800296X.

[107] Walter Steurer and Sofia Deloudi. “Crystallography of Quasicrystals: Concepts, Methods and Structures”. In: 2009.

[108] Z.M. Stadnik. *Physical Properties of Quasicrystals*. Springer Series in Solid-State Sciences. Springer Berlin Heidelberg, 1998. ISBN: 9783540651888. URL: https://books.google.de/books?id=fBB0a56uS5MC.

[109] S. Ranganathan et al. “A symmetrical indexing scheme for decagonal quasicrystals analogous to Miller-Bravais indexing of hexagonal crystals.” In: *Acta crystallographica. Section A, Foundations of crystallography* 63 Pt 1 (2007), pp. 1–10.

[110] J. D. Fitz Gerald et al. “The Al-Mn decagonal phase 1. A re-evaluation of some diffraction effects 2. Relationship to crystalline phases”. In: *Philosophical Magazine B* 58.1 (1988), pp. 15–33. DOI: 10.1080/13642818808211241.

[111] Eric R. Weeks John C. Crocker. *Particle tracking using IDL*. URL: http://www.physics.emory.edu/faculty/weeks//idl/index.html (visited on 05/05/2020).

[112] Eric Dufresne Daniel Blair. *The Matlab Particle Tracking Code Repository*. URL: http://site.physics.georgetown.edu/matlab/ (visited on 05/05/2020).

[113] R. Candelier et al. “Spatiotemporal Hierarchy of Relaxation Events, Dynamical Heterogeneities, and Structural Reorganization in a Supercooled Liquid”. In: *Phys. Rev. Lett.* 105 (13 Sept. 2010), p. 135702. DOI: 10.1103/PhysRevLett.105.135702.

[114] Anton Smessaert and Jörg Rottler. “Distribution of local relaxation events in an aging three-dimensional glass: Spatiotemporal correlation and dynamical heterogeneity”. In: *Phys. Rev. E* 88 (2 Aug. 2013), p. 022314. DOI: 10.1103/PhysRevE.88.022314.

[115] Marianne Renner et al. “A Simple and Powerful Analysis of Lateral Subdiffusion Using Single Particle Tracking”. In: *Biophysical Journal* 113.11 (2017), pp. 2452–2463. ISSN: 0006-3495. DOI: https://doi.org/10.1016/j.bpj.2017.09.017.

[116] Robert Laurini. “5 - Geographic Relations”. In: *Geographic Knowledge Infrastructure*. Ed. by Robert Laurini. Elsevier, 2017, pp. 83–109. ISBN: 978-1-78548-243-4. DOI: https://doi.org/10.1016/B978-1-78548-243-4.50005-0.

[117] Raphael Blumenfeld. “Disorder Criterion and Explicit Solution for the Disc Random Packing Problem”. In: *Phys. Rev. Lett.* 127 (11 Sept. 2021), p. 118002. DOI: 10.1103/PhysRevLett.127.118002.

[118] Yun Su et al. “Colloidal diffusion over a quasicrystalline-patterned surface.” In: *The Journal of chemical physics* 146 21 (2017), p. 214903.

[119] Jörg Bewerunge. “Colloids in random potentials: Optical realization and characterization of rough laser light fields”. PhD thesis. Heinrich-Heine-Universität Düsseldorf, May 2016.

[120] Linus Pauling. “Apparent icosahedral symmetry is due to directed multiple twinning of cubic crystals”. In: *Nature* 317 (1985), pp. 512–514.

[121] Albert Prodan et al. “The Equivalence Between Unit-Cell Twinning and Tiling in Icosahedral Quasicrystals”. In: *Sci. Reports 2017 71* 7.1 (2017), p. 12474. ISSN: 2045-2322. DOI: 10.1038/s41598-017-12669-w.

[122] M. Martinsons et al. “Event-chain Monte Carlo simulations of the liquid to solid transition of two-dimensional decagonal colloidal quasicrystals”. In: (2019). arXiv: 1906.05091. URL: http://arxiv.org/abs/1906.05091.

[123] Harini Pattabhiraman and Marjolein Dijkstra. “The effect of temperature, interaction range, and pair potential on the formation of dodecagonal quasicrystals in core-corona systems”. In: *J. Phys. Condens. Matter* (2017). ISSN: 1361648X. DOI: 10.1088/1361-648X/aa5530.

[124] Marjolein Linden, Jonathan Doye, and Ard Louis. “Formation of dodecagonal quasicrystals in two-dimensional systems of patchy particles”. In: *The Journal of chemical physics* 136 (Feb. 2012), p. 054904. DOI: 10.1063/1.3679653.

A Appendix

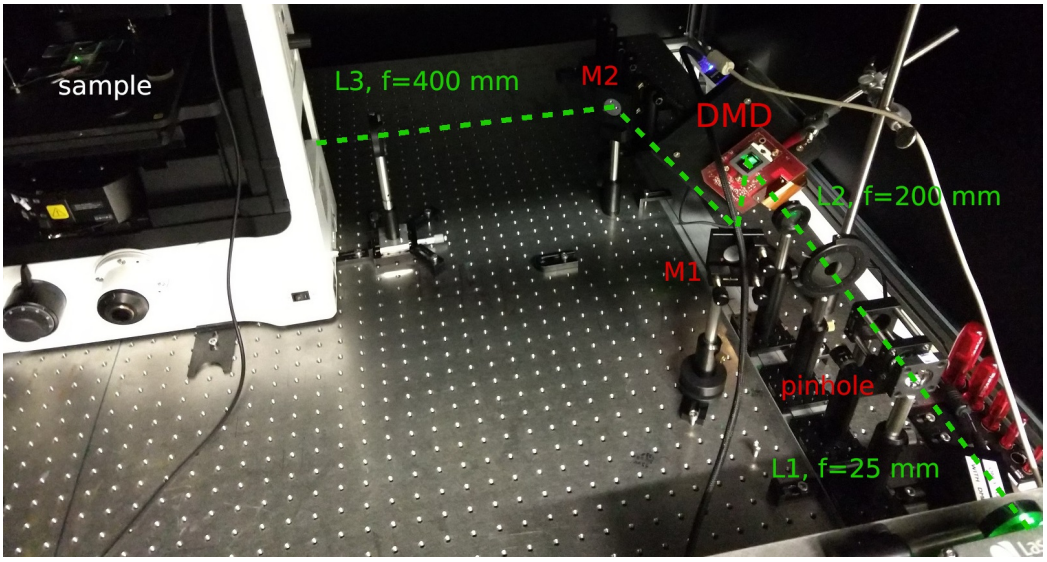

Figure A.1: A picture of the DMD setup as used in this work. Laser path is indicated (green dashed line). For a schematic illustration see fig. 3.5.

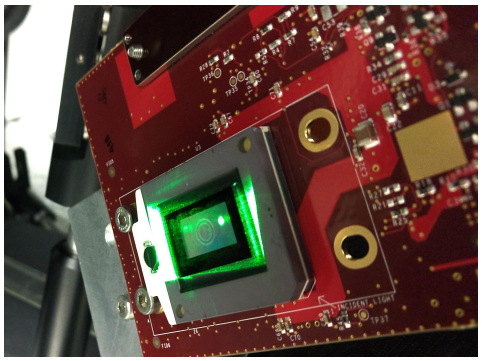

Figure A.2: A picture of the micro-mirror array of the DMD (TI, DLP6500 FYE). For a schematic illustration see fig. 3.3.

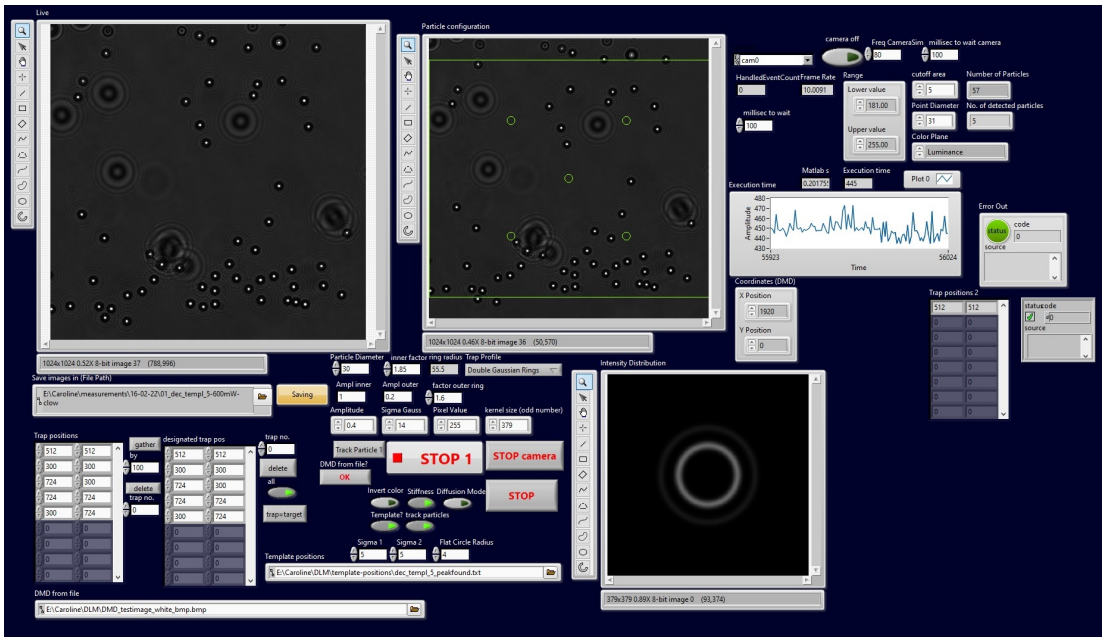

Figure A.2: Screenshot of the LabVIEW VI for controlling the DMD-setup.

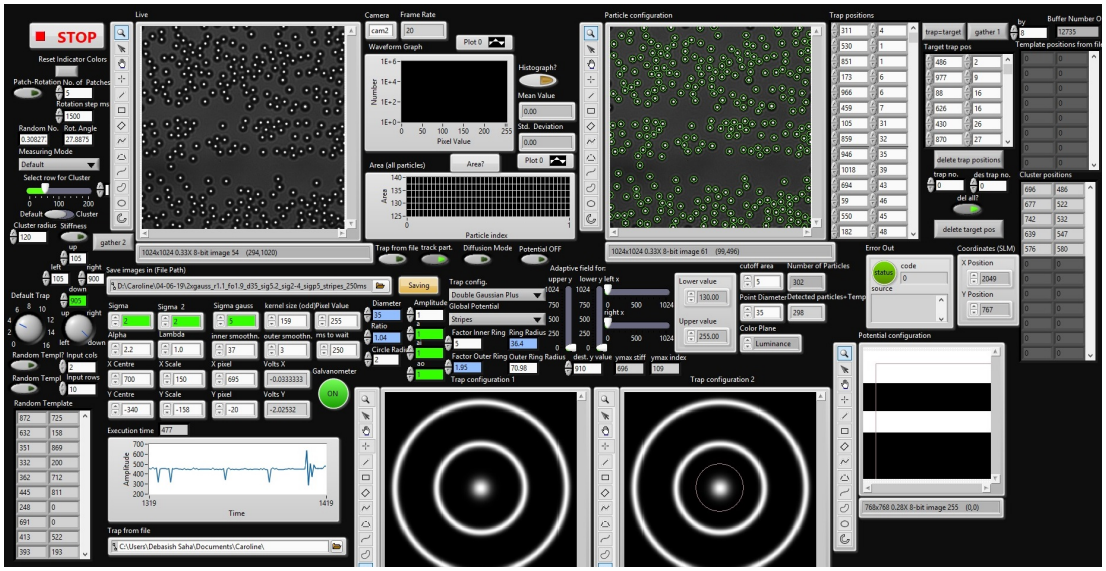

Figure A.2: Screenshot of the LabVIEW VI for controlling the SLM-setup.